

AD-A081 471

MCDONNELL DOUGLAS ASTRONAUTICS CO ST LOUIS MO F/G 20/4
NUMERICAL FLOW FIELD PROGRAM FOR AERODYNAMIC HEATING ANALYSIS. --ETC(U)
DEC 79 H J FIVE F33615-77-C-3003

UNCLASSIFIED

AFFDL-TR-79-3128-VOL-1

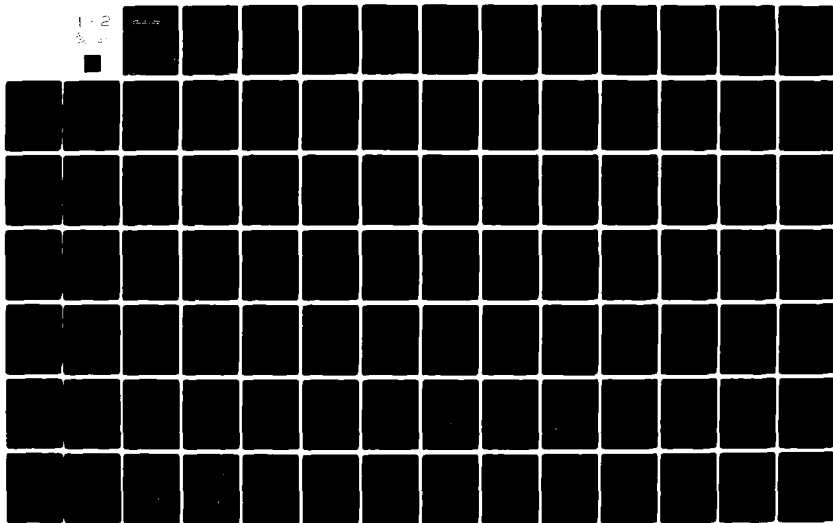
NL

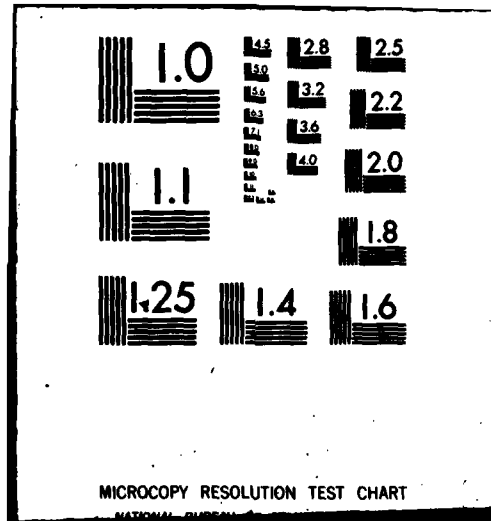
1 - 2

3 - 4



Page 10





AFFDL-TR-79-3128
VOLUME I

AD A 081 471

(Handwritten signature)

LEVEL

NUMERICAL FLOW FIELD PROGRAM FOR AERODYNAMIC HEATING ANALYSIS

Volume I — Equations and Results

H. J. Fivel

MCDONNELL DOUGLAS AERONAUTICS COMPANY-ST. LOUIS DIVISION
Saint Louis, Missouri 63166 (314) 232-0232

DECEMBER 1979

TECHNICAL REPORT AFFDL-TR-79-3128, VOLUME I
Final Report for June 1977 — September 1979

Approved for public release; distribution unlimited.

DTIC
SELECTED
MAR 6 1980
(Handwritten signature)

FILE COPY

AIR FORCE FLIGHT DYNAMICS LABORATORY
AIR FORCE WRIGHT AERONAUTICAL LABORATORIES
AIR FORCE SYSTEMS COMMAND
WRIGHT-PATTERSON AIR FORCE BASE. OHIO 45433

80 3 05 029


NOTICE

When Government drawings, specifications, or other data are used for any purpose other than in connection with a definitely related Government procurement operation, the United States Government thereby incurs no responsibility nor any obligation whatsoever; and the fact that the government may have formulated, furnished, or in any way supplied the said drawings, specifications, or other data, is not to be regarded by implication or otherwise as in any manner licensing the holder or any other person or corporation, or conveying any rights or permission to manufacture, use, or sell any patented invention that may in any way be related thereto.

This report has been reviewed by the Public Affairs Office (PA) and is releasable to the National Technical Information Service (NTIS). At NTIS, it will be available to the general public, including foreign nations.

This technical report has been reviewed and is approved for publication.


Arthur B. Lewis, Jr.
Project Engineer


Melvin L. Buck
Chief, High Speed Aero Perf. Branch

FOR THE COMMANDER


Peter J. Butkewicz
Colonel, USAF
Chief, Aeromechanics Division

If your address has changed, if you wish to be removed from our mailing list, or if the addressee is no longer employed by your organization please notify AFFDL/FXG, W-PAFB, OH 45433 to help us maintain a current mailing list.

Copies of this report should not be returned unless return is required by security considerations, contractual obligations, or notice on a specific document.

SECURITY CLASSIFICATION OF THIS PAGE (When Data Entered)

REPORT DOCUMENTATION PAGE		READ INSTRUCTIONS BEFORE COMPLETING FORM
1. REPORT NUMBER 18 AFFDL TR-79-3128-VOLUME 1	2. GOVT ACCESSION NO.	3. RECIPIENT'S CATALOG NUMBER
4. TITLE (and Subtitle) 6 NUMERICAL FLOW FIELD PROGRAM FOR AERODYNAMIC HEATING ANALYSIS, VOLUME I, EQUATIONS AND RESULTS	5. TYPE OF REPORT & PERIOD COVERED 9 FINAL TECHNICAL REPORT JUNE 1977 TO SEPTEMBER 1979	
7. AUTHOR(s) 10 H. J. FIVEL	8. CONTRACT OR GRANT NUMBER(s) 15 F33615-77-C-3003	
9. PERFORMING ORGANIZATION NAME AND ADDRESS MCDONNELL DOUGLAS ASTRONAUTICS COMPANY-ST. LOUIS P. O. BOX 516 ST. LOUIS, MISSOURI 63166	10. PROGRAM ELEMENT, PROJECT, TASK AREA & WORK UNIT NUMBERS 16 17 2404-07-10	
11. CONTROLLING OFFICE NAME AND ADDRESS AIR FORCE FLIGHT DYNAMICS LABORATORY (FXG) WRIGHT-PATTERSON AIR FORCE BASE OHIO 45433	12. REPORT DATE 11 DECEMBER 1979	
14. MONITORING AGENCY NAME & ADDRESS (if different from Controlling Office) 12 1251	13. NUMBER OF PAGES 124	
	15. SECURITY CLASS. (of this report) UNCLASSIFIED	
	15a. DECLASSIFICATION/DOWNGRADING SCHEDULE	
16. DISTRIBUTION STATEMENT (of this Report) APPROVED FOR PUBLIC RELEASE: DISTRIBUTION UNLIMITED		
17. DISTRIBUTION STATEMENT (of the abstract entered in Block 20, if different from Report)		
18. SUPPLEMENTARY NOTES		
19. KEY WORDS (Continue on reverse side if necessary and identify by block number) Aerodynamic heating 3-D BODIES COMPUTER PROGRAM INTERFERENCE HEATING FLAT BOTTOM DELTA WING FINS FLAPS A		
20. ABSTRACT (Continue on reverse side if necessary and identify by block number) This report documents a study to modify an existing computer program which provides an economical and easy to use analytic tool for aerodynamic heating to a wide variety of 3-dimensional vehicle configurations. This report also serves as a user's manual for the computer program plus two auxiliary programs written to analyze vehicle geometry, and presents program capabilities, input/output characteristics, and example problems. Core requirements have been minimized by the use of overlays. User oriented features of the program include minimized input requirements and various options for application flexibility.		

DD FORM 1 JAN 73 1473 EDITION OF 1 NOV 65 IS OBSOLETE

SECURITY CLASSIFICATION OF THIS PAGE (When Data Entered)

404231

43

A07 6442

FOREWORD

This report, "Numerical Flow Field Program for Aerodynamic Heating Analysis," describes the computer program that provides economical and accurate predictions of heat transfer to three-dimensional configurations. The report consists of the following two volumes:

- Volume I, Equations and Results
- Volume II, User's Manual

The work was performed by the McDonnell Douglas Astronautics Company - St. Louis Division (MDAC-St. Louis), under contract number F33615-77-C-3003 to the Air Force Flight Dynamics Laboratory, Air Force Systems Command, Wright-Patterson Air Force Base, Ohio. The subject contract was initiated in June 1977 and completed in September 1979. Mr. Arthur B. Lewis was the Air Force Project Engineer. Mr. H. W. Kipp was the Program Manager for MDAC-St. Louis and Mr. H. J. Fivel was the principal investigator.

The author gratefully acknowledges the major contributions of Dr. Fred R. DeJarnette of North Carolina State University to the development of the computer program and for his assistance in preparing several sections of this report. The author wishes to also thank Mr. N. J. Sliski, AFFDL, and Mr. W. H. Plath, MDAC, for their contributions to both the analyses and report write-up.

Requests for copies of the computer program and/or this report should be directed to the Air Force Flight Dynamics Laboratory (FXG).

This report supersedes AFFDL-TR-79-3025 Interim Report for June 1977 - December 1978, "Numerical Flow Field Program for Aerodynamic Heating Analysis," by H. J. Fivel, April 1979.

TABLE OF CONTENTS

Section		Page
I	INTRODUCTION	1
II	HEATING PROGRAM DESCRIPTION	3
	2.1 BASIC PROGRAM FOR AEROHEATING ON 3-D BODIES	3
	2.2 NEW METHOD FOR CALCULATING STREAMLINE METRIC	6
	2.3 IMPROVED ENTROPY SWALLOWING TECHNIQUE	8
III	OPTIONS ADDED IN THIS STUDY	9
	3.1 ADDED PRESSURE OPTIONS	9
	3.1.1 Modified Dahlem-Buck	11
	3.1.2 Prandtl-Meyer	12
	3.1.3 Van Dyke	14
	3.1.4 Tangent Wedge	14
	3.1.5 Tangent Cone	15
	3.1.6 Input Pressures	16
	3.1.7 Flat bottom Delta Wing	17
	3.2 ADDED TURBULENT HEATING OPTIONS	29
	3.2.1 Eckert Reference Enthalpy	29
	3.2.2 Van Driest	31
	3.3 INTERFERENCE HEATING	32
	3.3.1 Maximum Heating Rate on a Flap	32
	3.3.2 Fin/Plate Interaction	41
IV	SURFACE FITTING 3-D BODIES	52
	4.1 GENERAL DESCRIPTION OF GEOMETRY METHOD	52
	4.2 IMPROVEMENT TO LONGITUDINAL FITS	55
	4.3 GEOMETRY USING LOFTING TECHNIQUES	57
	4.4 TRANSLATOR CODE	58
V	OGIVE/CYLINDER CHECK CASE	62
	5.1 ARBITRARY GEOMETRY	62
	5.2 INPUT CONDITIONS	64
	5.2.1 Input Pressure Data	65
	5.2.2 Options and Other Input Data	67
	5.3 STREAMLINE GENERATION	67
	5.4 HEATING RATE DISTRIBUTION	70
	5.5 FIN/PLATE INTERACTION	74

TABLE OF CONTENTS

Section	Page
VI FLAT BOTTOM DELTA WING CHECK CASE	78
6.1 ARBITRARY GEOMETRY	79
6.2 INPUT CONDITIONS	79
6.3 STREAMLINE GENERATION	80
6.4 HEATING RATE DISTRIBUTION	82
VII SLAB DELTA CHECK CASE	88
7.1 INPUT CONDITIONS	88
7.2 STREAMLINE GENERATION	88
7.3 HEATING RATE DISTRIBUTION	91
7.4 FLAP HEATING	95
APPENDIX A TWO-STREAMLINE SCALE FACTOR EQUATION	104
REFERENCES	106

LIST OF ILLUSTRATIONS

Figure		Page
1	Two Streamline Method	7
2	Modified Newtonian Pressure Distribution	10
3	Measured Pressure Distribution On Windward Surface of Delta Wing, 0° Angle of Attack	18
4	Measured Pressure Distribution on Windward Surface of Delta Wing, 10° Angle of Attack	19
5	Delta Wing Pressure Determination	19
6	Windward Centerline Pressure Distribution on Delta Wing	21
7	Comparison of Centerline and Shoulder Pressures, 0° Angle of Attack	23
8	Comparison of Centerline and Shoulder Pressures, 5° Angle of Attack	23
9	Comparison of Centerline and Shoulder Pressures, 10° Angle of Attack	24
10	Shoulder Pressure Correlation	24
11	Position of Constant Shoulder Pressure Ratio	25
12	Spanwise Pressure Distribution, 4° Angle of Attack, X = 8 inch.	26
13	Spanwise Pressure Distribution, 4° Angle of Attack, X = 15 inch.	26
14	Spanwise Pressure Distribution, 4° Angle of Attack, X = 25 inch.	27
15	Spanwise Pressure Distribution, 4° Angle of Attack, X = 50 inch.	27
16	Spanwise Pressure Distribution, 12° Angle of Attack, X = 8 inch.	28
17	Spanwise Pressure Distribution, 12° Angle of Attack, X = 15 inch.	28
18	Spanwise Pressure Distribution, 12° Angle of Attack, X = 50 inch.	29
19	Flow Separation in Viscous Corner Flow	33
20	Wall Pressure Distribution in the Vicinity of Separation	33
21	Incipient Flow Separation	35
22	Plateau Pressure - Laminar Flow	36
23	Plateau Pressure - Turbulent Flow	37
24	Free Interaction Flow Deflection Angle	37
25	Measured Surface Pressure Distribution	38
26	Correlation of Peak Heating at Reattachment	41
27	The 3-D Interaction	42
28	Typical Oil Flow	42
29	Separation Location Coordinate System	43
30	Typical Surface Heating and Surface Pressure Profiles	44
31	Slope of Separation Asymptote	46
32	Separation Asymptote Parameter "a"	47
33	Exponent in Peak Pressure Correlation	48
34	Plateau Pressure Correlation	49
35	Coefficient in Peak Heating Correlation	50
36	Heating Profile with 3-D Interference	51
37	Curve Fit in Cross-Sectional Plane	53
38	Four Data Points Used to Define the Conic Section for this Segment	54
39	Longitudinal Curves Through the Four Points Used to Define the Conic Section for the Segment	55
40	Slope Determination for Longitudinal Curves	56
41	Body Cross Section Using Lofting Techniques	57

LIST OF ILLUSTRATIONS (Continued)

Figure		Page
42	Replacement of Circular Arc with Elliptical Segment	58
43	Complete Model for X-24C from HARP Format	59
44	X-24C Model Cut Off for Phase I	60
45	Model Schematic for Translator Code	60
46	X-24C Model from Translator Code	61
47	Ogive/Cylinder Model	62
48	Effect of Geometry Fit on Stagnation Point Curvature	63
49	Effect of Geometry Fit on Stagnation Heating	64
50	Spherical Nose Cap Pressures	65
51	Pressures on Ogive/Cylinder ($X=0.0699$ inch)	66
52	Pressures on Ogive/Cylinder ($X=39.6634$ inch)	66
53	Streamlines on Ogive/Cylinder, 12° Angle of Attack, Input Pressures - (Front View)	67
54	Streamlines on Ogive/Cylinder, 12° Angle of Attack, Input Pressures - (Side View)	68
55	Streamlines on Ogive/Cylinder, 8° Angle of Attack, Newtonian Pressure - (Front View)	68
56	Streamlines on Ogive/Cylinder, 8° Angle of Attack, Newtonian Pressure - (Side View)	69
57	Streamlines on Ogive/Cylinder, 12° Angle of Attack, Newtonian Pressure - (Front View)	69
58	Streamlines on Ogive/Cylinder, 12° Angle of Attack, Newtonian Pressure (Side View)	70
59	Ogive/Cylinder Centerline Heating Rate	70
60	Spanwise Heating Rate on Ogive/Cylinder, 12° Angle of Attack, Input Pressure	71
61	Spanwise Heating Rate on Ogive/Cylinder, $X = 10$ inch	71
62	Spanwise Heating Rate on Ogive/Cylinder, $X = 20$ inch	72
63	Spanwise Heating Rate on Ogive/Cylinder, $X = 30$ inch	72
64	Spanwise Heating Rate on Ogive/Cylinder, $X = 40$ inch	73
65	Spanwise Heating Rate on Ogive/Cylinder, $X = 47.5$ inch	73
66	Fin/Plate Interaction Heating, $X/X_{Fin} = 0.2$	75
67	Fin/Plate Interaction Heating, $X/X_{Fin} = 0.4$	75
68	Fin/Plate Interaction Heating, $X/X_{Fin} = 0.6$	76
69	Fin/Plate Interaction Heating, $X/X_{Fin} = 0.8$	76
70	Fin/Plate Interaction Heating, $X/X_{Fin} = 1.0$	77
71	X-24C Model for Delta Wing Check Case	78
72	X-24C Model from Geometry Coefficients	79
73	Streamlines on X-24C, 4° Angle of Attack - (Bottom View)	80
74	Streamlines on X-24C, 4° Angle of Attack - (Front View)	81
75	Streamlines on X-24C, 12° Angle of Attack - (Bottom view)	81
76	Streamlines on X-24C, 12° Angle of Attack - (Front View)	82
77	X-24C Axial Heating Rate Distribution, 4° Angle of Attack, $\beta = 0^\circ$	83
78	X-24C Axial Heating Rate Distribution, 4° Angle of Attack, $\beta = 2^\circ$	83
79	X-24C Axial Heating Rate Distribution, Variable Entropy, $\beta = 0^\circ$	84
80	X-24C Axial Heating Rate Distribution, Variable Entropy, $\beta = 2^\circ$	84

LIST OF ILLUSTRATIONS (Continued)

Figure		Page
81	X-24C Spanwise Heating Rate, 4° Angle of Attack	85
82	X-24C Spanwise Heating Rate, 12° Angle of Attack.	85
83	X-24C Spanwise Heating Rate, X = 200 inch	86
84	X-24C Spanwise Heating Rate, X = 300 inch	86
85	X-24C Spanwise Heating Rate, X = 419 inch	87
86	Streamlines on Slab Delta, 5.5° Angle of Attack, M = 6.8	89
87	Streamlines on Slab Delta, 10° Angle of Attack, M = 6.8	90
88	Streamlines on Slab Delta, 5.2° Angle of Attack, M = 9.6	90
89	Slab Delta Windward Centerline Heating, 5.5° Angle of Attack, M = 6.8	91
90	Slab Delta Windward Centerline Heating, M = 6.8, Laminar Flow . .	92
91	Slab Delta Windward Centerline Heating, Laminar Flow	92
92	Slab Delta Spanwise Heating, 5.5° Angle of Attack, M = 6.8, X = 1.0 inch	93
93	Slab Delta Spanwise Heating, 5.5° Angle of Attack, M = 6.8, X = 2.0 inch	93
94	Slab Delta Spanwise Heating, 5.5° Angle of Attack, M = 6.8, X = 3.0 inch	94
95	Slab Delta Spanwise Heating, 5.5° Angle of Attack, M = 6.8, X = 4.0 inch	94
96	Slab Delta Spanwise Heating, 5.5° Angle of Attack, M = 6.8, X = 4.53 inch	95
97	Peak Heating on a Flap, 10° Angle of Attack, M = 6.8	96
98	Peak Heating on a Flap, 5.2° Angle of Attack, M = 9.6	97
99	Spanwise Peak Heating on a Flap, Flap Angle = 10°	97
100	Spanwise Peak Heating on a Flap, Flap Angle = 20°	98
101	Spanwise Peak Heating on a Flap, Flap Angle = 30°	98
102	Spanwise Peak Heating on a Flap, 10° Angle of Attack, M = 6.8 . .	99
103	Spanwise Peak Heating on a Flap, 5.2° Angle of Attack, M = 9.6 .	99
104	Peak Stanton Number on a Flap, 10° Angle of Attack, M = 6.8 . . .	100
105	Peak Stanton Number on a Flap, 5.2° Angle of Attack, M = 9.6 . .	101
106	Spanwise Peak Stanton Number on a Flap, Flap Angle = 10°	101
107	Spanwise Peak Stanton Number on a Flap, Flap Angle = 20°	102
108	Spanwise Peak Stanton Number on a Flap, Flap Angle = 30°	102
109	Spanwise Peak Stanton Number on a Flap, 10° Angle of Attack, M = 6.8	103
110	Spanwise Peak Stanton Number on a Flap, 5.2° Angle of Attack, M = 9.6	103

LIST OF SYMBOLS

a	curve fit constant for modified Dahlem-Buck cone pressure, defined by Equation (13)
a	separation location correlation parameter. See Figures 29, 31 and 32.
a_o	distance from leading edge of flat plate to fin leading edge. See Figure 27.
A	constant in flat bottom delta wing spanwise pressure distribution equation
b	separation location correlation parameter. See Figures 29, 31 and 32.
b	function in the oblique shockwave relation, Equation (20)
B	constant in flat bottom delta wing spanwise pressure distribution equation
c	function in the oblique shockwave relation, Equation (20)
C	constant in flat bottom delta wing spanwise pressure distribution equation
C	constant in the peak to shock heat transfer distribution equation, defined in Equation (62)
C_f	skin friction coefficient
\overline{C}_f	incompressible skin friction coefficient
C_p	pressure coefficient
C_p	specific heat ratio at constant pressure
C_{st}	constant in the shear layer relation, Equation (50), for Stanton number
d	function in the oblique shockwave relation, Equation (20)
D	constant in flat bottom delta wing spanwise pressure distribution equation
D_{NOSE}	vehicle nose diameter
\hat{e}_s, \hat{e}_β	unit vectors in streamline coordinate system
\hat{e}_x, \hat{e}_ϕ	unit vectors in cylindrical coordinate system

LIST OF SYMBOLS (Continued)

f	body radius
F_C	transformation function for skin friction, defined by Equation (38)
F_θ	transformation function for momentum thickness Reynolds number, defined by Equation (36)
h	streamline metric
h	independent variable for velocity expansion expression in tangent-cone pressure solution, defined by Equation (22)
h	enthalpy
h	heat transfer coefficient
h	difference between the conical ray angle and the cone half angle
h_s	streamline metric in s-direction
H_C	compressible form factor ($H_C = \delta^*/\theta_m$)
J	mechanical equivalent
K	constant in the two-dimensional separation correlation. See Equation (44).
L_{SEP}	length of separated region in a two-dimensional interaction
L_{HINGE}	length from separation point to hinge line in a two-dimensional interaction
L_{FLAP}	length along flap from hinge line to reattachment point
Δz	distance between two adjacent streamlines for calculating streamline metric. See Figure 1.
M	Mach number
n	exponent in curve fit for modified Dahlem-Buck cone pressure, defined by Equation (14)
n	exponent in heat transfer distribution relation given by Equation (61)
n_{PK}	exponent in peak pressure - shock angle correlation given by Equation (56)

LIST OF SYMBOLS (Continued)

n_{st}	exponent in straight-line correlation of data in Figure 26. See Equation (50).
N	exponent in expression modifying Newtonian pressure distribution, defined in Equation (6)
P	pressure
P_{ASYMPT}	asymptotic value of windward centerline pressure on delta wing flat bottom
P_E	peak pressure on the leading edge of a flat bottom delta wing. See Figure 5.
P_F	pressure at the spanwise location where the pressure approaches the centerline value. See Figure 5.
P_M	pressure at the match point between the modified Newtonian pressure distribution on the leading edge and the flat bottom delta wing pressure. See Figure 5.
P_q	local pressure at match point for Prandtl-Meyer solution
Pr	Prandtl Number
$P_{SHOULDER}$	pressure at the shoulder
$(P_1)_i$	undisturbed pressure at hinge line of compression flap
$(P_2)_i$	pressure at incipient separation
q	heating rate
q_∞	free stream dynamic pressure
Q	local to free stream static pressure ratio, defined by Equation (15)
Q	local heating rate
Q_M	minimum shoulder to centerline pressure ratio
Q_{MM}	minimum shoulder to centerline pressure ratio at zero degrees angle of attack
Q_S	heating rate at stagnation point
Q_W	local heating rate

LIST OF SYMBOLS (Continued)

Q_{WS}	heating rate at stagnation point
r	recovery factor
Re	Reynolds number
Re_S	undisturbed Reynolds number based on distance along a streamline from the stagnation point to the hinge line
Re_{SHEAR}	Reynolds number based on shear layer thickness. See Equation (47).
Re_δ	boundary layer thickness Reynolds number based on undisturbed conditions at hinge line of compression flap
Re_θ	momentum thickness Reynolds number
\bar{Re}_θ	transformed (incompressible) momentum thickness Reynolds number
R_N	nose radius
R_{OG}	ogive radius, see Figure 47
S_0	distance along delta wing surface normal to leading edge from midline of wing
S	factor to match McElderry flat bottom centerline pressure distribution with nose cap pressure, see Equation (29)
S	distance along streamline, measured from stagnation point
St	Stanton number
t	delta wing model thickness
T	constant in McElderry centerline pressure distribution, defined by Equation (30)
T	temperature
U	velocity
W_f	weighting factor in Equation (2), 0 for laminar flow and 1 for turbulent flow
X	Cartesian coordinate in axial direction
X	distance measured from fin leading edge. See Figure 27.

LIST OF SYMBOLS (Continued)

x_c	axial location, in nose diameters (measured from the vertex), where the ratio of shoulder pressure to centerline pressure becomes constant
x_c	distance along a streamline from the separation point to the hinge line
x_R	axial distance from the hinge line to the reattachment point
x_S	distance along a streamline from the stagnation point to the separation point
x'	distance measured along fin. See Figure 27.
\bar{x}	distance measured along shockwave. See Figure 27.
y	Cartesian coordinate, normal to x
Δy	distance outboard of shock
\bar{y}	distance measured normal to shockwave. See Figure 27.
y_0, y_1, y_h, y_s z_0, z_1, z_h, z_s	the coordinates of the four points used to define the conic equation in a particular cross sectional plane. See Figures 38 and 39.
y', z'	Axes of the local coordinate system used to describe a conic section in a cross-sectional plane. See Section 3.2.1 for details.
z	Cartesian coordinate, normal to x
α	angle of attack
β	coordinate normal to streamline on body surface
$\Delta\beta$	angular difference between primary and secondary streamlines. See Figure 1.
Γ	body angle, defined in geometry output Section 3.2.3, Volume II
$\bar{\Gamma}$	shock wave angle
γ	ratio of specific heats
δ	impact angle of freestream to local body surface
δ	boundary layer thickness
δ_{MATCH}	value of the cone half angle where the cone pressure matches the modified Dahlem-Buck pressure

LIST OF SYMBOLS (Continued)

δ_ϕ	body angle, defined in geometry output Section 3.2.3, Volume II
δ^*	displacement thickness
θ	conical ray angle
θ	inclination angle of surface inviscid streamline
θ_C	incidence angle of body
θ_D	deflection angle of the dividing streamline. See Figure 19.
θ_i	wedge angle for incipient separation
θ_{FIN}	effective fin deflection angle measured with respect to the local freestream direction
θ_m	momentum thickness
θ_{SH}	shock angle
μ	viscosity
ν	Prandtl-Meyer angle of expansion from sonic flow to the match point, defined by Equation (18)
ξ	coordinate along a streamline
ξ	pressure ratio across an oblique shock. See Equation (39).
ρ	density
ϕ	circumferential angle, see Figure 37
Φ	orientation angle between two streamlines. See Figure 1.
ϕ_E	angular location of the peak pressure on the leading edge of a flat bottom delta wing. See Figure 5.
ϕ_F	angular location of the place where the pressure approaches the centerline value. See Figure 5.
ϕ_M	angular location of the matchpoint between the modified Newtonian pressure on the leading edge and the flat bottom delta wing pressure. See Figure 5.
ϕ_S	angular location of the shoulder of the flat bottom delta wing pressure distribution. See Figure 5.

LIST OF SYMBOLS (Continued)

ψ	complement of the impact angle, δ , used in the Newtonian pressure routine
ψ	Y-coordinate measured from the shock normal to the fin. See Figure 28.
ψ_{BL}	mass flux absorbed by the boundary layer, defined by Equation (2)
ψ_{PK}	location of peak heating with respect to the fin
ψ_{SH}	mass flux crossing the bow shock wave, defined by Equation (3)

Subscripts

aw	adiabatic wall
CL	windward centerline
CONE	value on a cone surface
DB	Dahlem-Buck
e	boundary layer edge
FLAP	value on or with respect to a flap
FIN	value on or with respect to a fin
i	conditions at incipient separation
MDB	modified Dahlem-Buck
PK	peak value
PLAT	value on or with respect to plateau region
q	Prandtl-Meyer match point
L	laminar flow
REF	reference value
S	stagnation
SEP	value in or with respect to plateau region
SH	value at or with respect to shockwave
SHEAR	value based on shear layer thickness

LIST OF SYMBOLS (Continued)

STAG	stagnation point
T	turbulent flow
u	undisturbed value
w	wall
0	stagnation
∞	free stream

Superscript

*	reference condition, defined by Equation (33)
---	---

SECTION I

INTRODUCTION

Design of high speed vehicles requires a fast, reliable method for the prediction of heat loads to all parts of a vehicle over an entire flight trajectory. The extensive application of complex automated procedures is often prohibitive in terms of both time and computer costs. The fundamental purpose of the Numerical Flow Field Program for Aerodynamic Heating Analysis is to provide an economical, easy-to-use engineering analysis tool for computation of aerodynamic heating to a wide variety of both simple and complex high speed vehicle configurations. Complex configurations include vehicles having features which produce strong shocks, such as flaps and fins. Of specific interest are configurations having flat or nearly flat surfaces and regions in which streamlines converge.

The current-generation flow field computer program developed by DeJarnette (Reference 1) does provide accurate predictions of heat transfer to simplified geometries. This document reports on modifications to the DeJarnette code which increase the options available to the user in the areas of surface pressure determination, turbulent heat transfer, geometric description, and interference heating. Specific subtasks in the first phase of the study included addition of improved pressure computations for flat or nearly flat-bottom configurations, evaluation of transition criteria and transitional heating computation methods, review and implementation of additional aerodynamic heating methods for turbulent flow, and modification of the code to allow additional geometry input options. The second phase of the study was concerned with evaluating prediction methods for interference heating, both on flaps and in the vicinity of fins. Two other computer programs were developed for use with the heating code to generate the geometry of general three-dimensional bodies from coordinates of points in several cross-sectional planes. One auxiliary program provides the necessary curve fit techniques. The other program is a translator code that converts basic geometry description data in the HABP (Hypersonic Arbitrary Body Program) form (References 2 and 3) to a form acceptable in the geometry code.

This volume of the report contains an overview of the computer program capabilities and includes a brief description of the added components. Section 3 discusses those added components for the aeroheating code. A discussion of the auxiliary geometry codes for surface fitting 3-D bodies may be found in Section 4. Results of several sample cases are presented in the remaining sections. Potential users are directed to the Volume II User's Manual for a detailed discussion of the input description. Both Volume II and this volume supersede the user's manual for the preliminary version of the codes, reported in Reference 4.

SECTION II

HEATING PROGRAM DESCRIPTION

This section presents a brief discussion of the basic heating program analysis described in Reference 5 and a discussion of a new technique to determine the scale factor and an improved entropy swallowing technique. Subroutines and options added to the program to increase the pressure and heat transfer capability are discussed in Section 3.

2.1 BASIC PROGRAM FOR AEROHEATING ON 3-D BODIES

A relatively simple computer program has been developed to calculate laminar, transitional, and turbulent heating rates on arbitrary, blunt-nosed, three-dimensional bodies at angles of attack in high-speed flow. The technique is an engineering analysis which does not require a solution of the complete flow-field equations. In this technique, inviscid surface streamlines are calculated from Euler's equation using a prescribed pressure distribution. Heating rates are calculated along a streamline by applying the axisymmetric analog to the three-dimensional boundary-layer equations. This approximation allows the heat-transfer rate to be calculated along an inviscid surface streamline by any boundary-layer method applicable to a body of revolution at zero incidence. The distance along the three-dimensional streamline is interpreted as the distance along the equivalent axisymmetric body, and the scale factor (which is a measure of the divergence of adjacent three-dimensional streamlines) is interpreted as the radius of the equivalent axisymmetric body. Each inviscid surface streamline corresponds to a different equivalent body of revolution and may be calculated independently of the others.

In order to keep the calculations simple, laminar heating rates are calculated by applying the axisymmetric analog to the local similarity method of Beckwith and Cohen (Reference 6). For turbulent heating rates, a modified form of Reshotko and Tucker's integral method is used to calculate the momentum thickness (Reference 7). In the original version of the program the momentum thickness Reynolds number is used to calculate the local skin friction coefficient with a technique developed by Spalding and Chi (Reference 8). The skin-friction coefficient is converted to the turbulent heating rate through von Karman's form of

Reynolds analogy factor (Reference 9). A transition region may be prescribed by defining the beginning and end of transition. Heating rates are calculated within the transition region as a weighted average of the local laminar and turbulent values (Reference 10). Either ideal gas or equilibrium air properties may be used and the properties at the edge of the boundary layer may be calculated using either normal-shock entropy or variable entropy.

The equations for the streamline geometry and scale factor are singular at the stagnation point. Therefore, an analytic solution is used for a small region surrounding the stagnation point, and then heating rates are calculated along an inviscid surface streamline as it is generated downstream. The number of streamlines to be calculated is chosen to give the desired distribution of heating rates.

The following list summarizes the options and features available with the current version of the aerodynamic heating program.

Pressure

Modified Newtonian

Dahlem-Buck

Prandtl-Meyer

Van Dyke

Tangent wedge

Tangent cone

Input values

Flat bottom delta wing

Turbulent heat transfer

Spalding-Chi

Van Driest

Eckert reference enthalpy

Transition specification

Geometric location

Momentum thickness Reynolds number

Integrated unit Reynolds number

Local momentum thickness Reynolds number divided
by local Mach number

Analytical body of revolution to describe geometry

Hemisphere nose - ogive

Hemisphere nose - cone

Hemisphere - cylinder

Hemisphere nose - ogive - cylinder

Analytical body to describe geometry

Slab delta

Arbitrary body from cross section coordinates

Cross section coordinates

Cross section described by loft lines

Interference heating

Two-dimensional flap

Three-dimensional fin/plate interaction

Inviscid flow field for boundary layer edge

Normal shock entropy

Variable entropy

Gas state

Perfect gas

Equilibrium air

Viscosity

Sutherland's law

Keyes viscosity law

Wall temperature

Input enthalpy ratio, calculate temperature

Input temperature, calculate enthalpy ratio

Output print option

Print-out at specified axial locations

Other program features included a flag for laminar or turbulent flow and a print-out option. The user is directed to the Volume II, User's Manual, Section 3 on input for instructions on exercising the options.

2.2 NEW METHOD FOR CALCULATING STREAMLINE METRIC

The technique used in Reference 5 for calculating the scale factor required first and second derivatives of the surface pressure with respect to the longitudinal and circumferential coordinates. The pressure and its derivatives were calculated from either the modified Newtonian pressure distribution or surface fits to input pressure data. This method worked well for simple body shapes, e.g., blunted cones, whose geometry could be described by analytical equations. It was subsequently found, however, that the accuracy of obtaining second derivatives of the pressure by these techniques was poor for complex geometrical configurations and for irregular input pressure data. Therefore, a new technique, called the two-streamline method, was developed to calculate the scale factor without using second derivatives of the surface pressure.

In the two-streamline method, for each primary streamline to be calculated a secondary streamline, very close to the primary streamline, is also calculated using the same method described in Reference 5. These two streamlines are traced along the body in a step-by-step fashion by numerically integrating an ordinary differential equation for each streamline. However, only the pressure and first derivatives of the pressure are needed in these calculations. For each step of the integration the scale factor, h , is calculated from the distance between the primary and secondary streamlines, as shown in Figure 1. The distance between the two streamlines is Δl and, therefore, the scale factor is

$$h = \frac{\Delta l \cos \phi}{\Delta \beta} \quad (1)$$

where the surface coordinate normal to the streamline is β . This coordinate is constant along a streamline and its value is assigned at the stagnation point. However, Equation (1) is not in a form suitable for use in the program. Derivation of the equation used in the program is given in Appendix A.

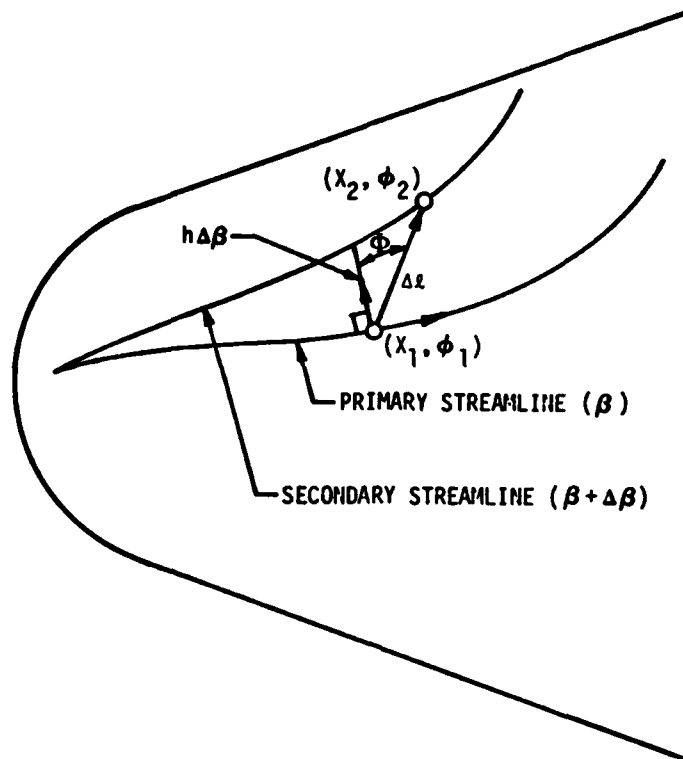


FIGURE 1 - TWO STREAMLINE METHOD

The scale factor, h , is used to calculate the heating rate on the primary streamline only. The only parameter needed from the secondary streamline is its geometric position on the body at each integration step. The two-streamline method was found to give much more satisfactory results than the previous method for calculating the scale factor. The elimination of the need for second derivatives of the surface pressure more than compensates for the additional calculations required for the secondary streamline. As a result, the new method is more efficient as well as more accurate than the old method.

2.3 IMPROVED ENTROPY SWALLOWING TECHNIQUE

Entropy layer swallowing effects are accounted for by using a mass-balance technique which requires that the mass flux being swallowed by the boundary layer, ψ_{BL} , be equal to the mass flux crossing the bow shockwave, ψ_{SH} , along an inviscid streamline. In Reference 11 it is shown that the mass flux being absorbed by the boundary layer is

$$\psi_{BL} = \rho_e U_e h \left[5.27 (1 - w_f) \theta_{m,L} - 9 w_f \theta_{m,T} \right] \quad (2)$$

while the mass flux crossing the bow shockwave is

$$\psi_{SH} = \rho_\infty U_\infty \int_0^S \sin \bar{\Gamma} h ds \quad (3)$$

In the old analysis, the turbulent momentum thickness, $\theta_{m,T}$, was determined from the axisymmetric, momentum integral equation,

$$\frac{d\theta_{m,T}}{ds} = \frac{C_f}{2} + (M_e^2 - 2 - H_c) \frac{\theta_{m,T}}{U_e} \frac{dU_e}{ds} - \frac{\theta_{m,T}}{h} \frac{dh}{ds} \quad (4)$$

where the coefficient of friction, C_f , was calculated using one of the turbulent skin friction options listed in Section 2.1. This equation was evaluated using a fourth order, Runge-Kutta numerical integration technique. An iteration procedure was used to converge ψ_{BL} and ψ_{SH} by continually improving the estimate for the shockwave angle, $\bar{\Gamma}$, and consequently ρ_e and U_e , the local density and velocity respectively.

In the new analysis, the functional relation $(\rho_e U_e h \theta_{m,T})$, instead of $\theta_{m,T}$, is the parameter that is integrated along the streamline direction.

Utilizing Equation (4) it can be shown that

$$\frac{d(\rho_e U_e h \theta_{m,T})}{ds} = \rho_e U_e h \frac{C_f}{2} - (H_c + 1) \rho_e U_e h \theta_{m,T} \left(\frac{1}{U_e} \frac{dU_e}{ds} \right) \quad (5)$$

Note that in this expression there is no need to calculate dh/ds as there is in Equation (4). Thus, $\rho_e U_e h \theta_{m,T}$ is known (from the Runge-Kutta integration) and no iteration for ρ_e or U_e is required in the entropy calculation.

SECTION III

OPTIONS ADDED IN THIS STUDY

Several subroutines were prepared in this study to increase the options available to the user for local pressure, turbulent heat transfer, transition specification, geometry descriptions, and interference heating. The following subsections discuss features of the added pressure, turbulent heat transfer, and interference heating routines. Cross section geometry is discussed in Section 4. The user is directed to the Volume II, User's Manual, Section 2 on input for instructions on triggering the various options.

3.1 ADDED PRESSURE OPTIONS

The new pressure options added that are analytical in form are, in general, valid only at low local impact or incidence angles. The incidence angle is the angle between the free stream and the body tangency plane at the desired location. (Input pressure values, of course, are valid over the entire vehicle). Using the modified Newtonian pressure distribution in the stagnation region results in a mismatch with the low impact angle expressions. This mismatch is eliminated by substituting a different relationship for the $\sin^2(\delta)$ term in the Newtonian distribution. An exponent less than 2 on the $\sin(\delta)$ retains the general shape of the Newtonian distribution, but predicts greater pressures at low impact angles which can be matched to the appropriate distribution while retaining the proper stagnation value. The resulting expression is:

$$C_p = C_{p_{stag}} (\sin \delta)^N \quad (6)$$

where

C_p = pressure coefficient

$C_{p_{stag}}$ = stagnation value of pressure coefficient

δ = impact angle

An iterative procedure is employed to determine the exponent at the point where the pressures and pressure derivatives of the two correlations match. This concept is illustrated in Figure 2. A typical Dahlem-Buck distribution curve does

not cross the Newtonian curve for an exponent of 2, but appears to be tangent to a curve for an exponent between 1.8 and 2. The solution yields an exponent of 1.86, tangent at $\delta = 18.8^\circ$. By inspection, the 1.86 curve would be quite similar to the 2.0 curve.

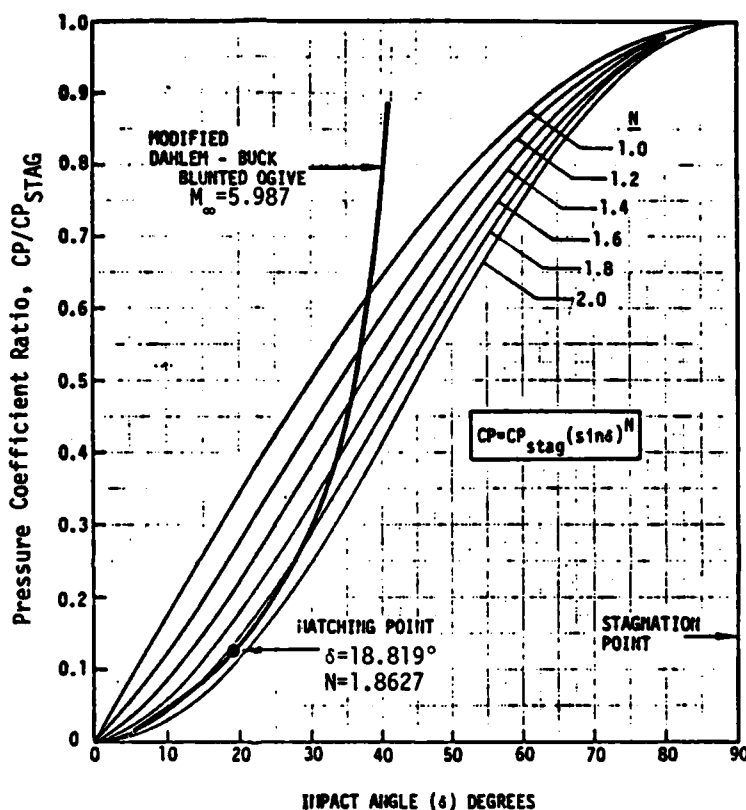


FIGURE 2 - MODIFIED NEWTONIAN PRESSURE DISTRIBUTION

All the analytical-type pressure routines are written as functions of the impact angle, δ , where δ is the complement of the angle, ψ , used in the Newtonian pressure routine in the form $\cos^2 \psi$. Relating the partial derivatives of local pressure then to the primary independent variables of X and ϕ results in the following expressions:

$$\frac{\partial(P/P_\infty)}{\partial X} = \frac{q_\infty}{2 P_\infty \sin \psi \cos \psi} \left(\frac{\partial C_p}{\partial \delta} \right) \frac{\partial(\cos^2 \psi)}{\partial X} \quad (7)$$

and

$$\frac{\partial(P/P_s)}{\partial\phi} = \frac{q_\infty}{2P_s \sin\psi \cos\psi} \left(\frac{\partial C_p}{\partial\delta} \right) \frac{\partial(\cos^2\psi)}{\partial\phi} \quad (8)$$

where:

C_p = pressure coefficient

P_s = stagnation pressure

q_∞ = free stream dynamic pressure

3.1.1 Modified Dahlem-Buck

The modified Dahlem-Buck method uses an empirical relationship which approximates tangent cone pressures at low incidence angles and approaches Newtonian values in the stagnation region at large incidence angles. The original method has been shown to be in good agreement with data on highly swept shapes at large hypersonic Mach numbers and modifications extend the range to lower Mach numbers (Reference 12). Thus,

$$C_{p_{MDB}} = C_{p_{DB}} \left[\frac{C_{p_{cone}}(M < 20)}{C_{p_{cone}}(M = 20)} \right] \quad (9)$$

where $C_{p_{MDB}}$ is the modified Dahlem-Buck pressure coefficient.

The original equations are

$$\text{for } \delta \leq \delta_{MATCH} \quad C_{p_{DB}} = \left[\frac{1.0}{(\sin 4\delta)^{3/4}} + 1.0 \right] \sin^2 \delta \quad (10)$$

$$\text{for } \delta > \delta_{MATCH} \quad C_p = C_{p_{stag}} \sin^N \delta \quad (11)$$

If, at small values of δ , the bracketed term exceeds 5.0 it is set at 5.0.

Reference 12 shows a curve fit of data which permits the cone pressure coefficient fraction to be analytically defined, so that

$$\frac{C_{p\text{ cone}}(M < 20)}{C_{p\text{ cone}}(M = 20)} - 1.0 = a \delta^n \quad (12)$$

where δ is the impact angle in degrees, and

$$a = (6.0 - 0.3 M_\infty) + \sin \left(\frac{\ln M_\infty - 0.588}{1.20} \pi \right) \quad (13)$$

$$-n = 1.15 + 0.5 \sin \left(\frac{\ln M_\infty - 0.916}{3.29} \pi \right) \quad (14)$$

3.1.2 Prandtl-Meyer

This method is based on a technique recommended by Kaufman in Reference 13 which involves matching the modified Newtonian and Prandtl-Meyer expansion methods at a point where the pressure gradients with respect to axial distance calculated by each method are equal. A local Mach number at the match point, M_q , is assumed and iterated on until the Prandtl-Meyer free stream static to local stagnation pressure ratio matches the Newtonian value. At the match point, the local to stagnation pressure ratio is given by:

$$\frac{P_q}{P_s} = Q = \left[\frac{2}{2 + (\gamma - 1) M_q^2} \right]^{\frac{\gamma}{\gamma - 1}} \quad (15)$$

and the free stream static to stagnation pressure ratio is given by

$$\frac{P_{\infty}}{P_s} = Q \left[1 - \frac{\gamma^2 M_q^4 Q}{4 (M_q^2 - 1) (1 - Q)} \right] \quad (16)$$

The angle of incidence at the match point can be determined from

$$\sin^2 \delta_q = \frac{\left(Q - \frac{P_{\infty}}{P_s} \right)}{\left(1 - \frac{P_{\infty}}{P_s} \right)} \quad (17)$$

and the Prandtl-Meyer angle for expansion from sonic flow to the match point is

$$\nu = \sqrt{\frac{\gamma+1}{\gamma-1}} \tan^{-1} \left[\sqrt{\frac{\gamma-1}{\gamma+1} (M_q^2 - 1)} \right] - \tan^{-1} \left[\sqrt{M_q^2 - 1} \right] \quad (18)$$

The local pressure at some arbitrary incidence angle is determined by first iteratively solving for a local Mach number that satisfies Equation (18) for expansion from sonic flow to the incidence angle and then substituting that Mach number in Equation (15).

There is no pressure mismatch between Newtonian and Prandtl-Meyer so that the Newtonian expression remains unaltered.

3.1.3 Van Dyke

This method is based on the unified supersonic-hypersonic small disturbance theory of Van Dyke in Reference 14. The method is valid at small incidence angles for thin profile shapes and is given by

$$C_p = \delta^2 \left[\frac{\gamma+1}{2} + \sqrt{\left(\frac{\gamma+1}{2}\right)^2 + \frac{4}{\delta^2(M^2-1)}} \right] \quad (19)$$

3.1.4 Tangent Wedge

The tangent-wedge pressures are calculated using the oblique shock relationships of NACA TR-1135 (Reference 15). The basic equation is a cubic relating the local shock wave angle to the angle of incidence.

$$\left(\sin^2 \theta_{SH}\right)^3 + b \left(\sin^2 \theta_{SH}\right)^2 + c \left(\sin^2 \theta_{SH}\right) + d = 0 \quad (20)$$

where

θ_{SH} = shock angle
 δ = wedge angle

$$b = -\frac{M^2 + 2}{M^2} - \gamma \sin^2 \delta$$

$$c = \frac{2M^2 + 1}{M^4} + \left[\frac{(\gamma+1)^2}{4} + \frac{\gamma-1}{M^2} \right] \sin^2 \delta$$

$$d = -\frac{\cos^2 \delta}{M^4}$$

The roots of the above cubic equation may be obtained by using the trigonometric solution procedure outlined in Reference 16. The local pressure is related to the shock angle by

$$C_p = \frac{4(M_\infty^2 \sin^2 \theta_{SH} - 1)}{(\gamma + 1) M_\infty^2} \quad (21)$$

3.1.5 Tangent Cone

The tangent cone method used here is the approximate solution devised by Hammitt and Murthy in Reference 17. They expand the expression for velocities between the body and the shock by a Taylor series in terms of h , where

$$h = \theta - \theta_c \quad (22)$$

θ is the conical ray angle and θ_c refers to the incidence angle of the body. The value of h at the shock (h_{SH}) is given by

$$h_{SH} = \frac{-\sin 2\theta_c}{[2 - (\gamma + 5) \sin^2 \theta_c]} \pm \sqrt{\left| \frac{\sin 2\theta_c}{[2 - (\gamma + 5) \sin^2 \theta_c]} \right|^2 + \left| \frac{(\gamma - 1) \sin^2 \theta_c + (2/M_\infty^2)}{[2 - (\gamma + 5) \sin^2 \theta_c]} \right|} \quad (23)$$

The correct solution is the smaller positive value. The local pressure is given by

$$\frac{P}{P_\infty} = \left[\frac{2\gamma}{\gamma + 1} M_\infty^2 \sin^2 \theta_{SH} - \frac{\gamma - 1}{\gamma + 1} \right] \times \left[1 + \frac{\gamma M_\infty^2 \cos^2 \theta_{SH} h_{SH}^2}{1 + \frac{\gamma - 1}{2} M_\infty^2 \sin^2 \theta_{SH}} \right] \quad (24)$$

3.1.6 Input Pressures

One of the options in the aerodynamic heating program is to use input pressure data to calculate the inviscid surface streamlines and heating rates. These input pressures may be experimental data or calculated from some other computer program. A computer subprogram has been prepared to "surface fit" this data. The subprogram calculates the pressure ratio P/P_S and its derivatives, $\partial(P/P_S)/\partial\phi$ and $\partial(P/P_S)/\partial X$, at any position (X, ϕ) on the body.

It is required that the pressure data be input to the computer program as the ratio P/P_S at a number of longitudinal positions (X) in several meridional planes (ϕ). The pressure data should be smoothed before input. The longitudinal positions where data are input may differ from one meridional plane to another. Also, the meridional planes need not be evenly spaced, but the first plane must be the windward plane ($\phi = 0$) and the last plane must be the leeward plane ($\phi = 180^\circ$). In addition, one input pressure point in the windward plane must be the stagnation point ($P/P_S = 1$).

The computer subprogram first fits longitudinal curves (P/P_S vs X) through the pressure data in each meridional plane separately. A cubic is curve fit through two successive data points in the longitudinal direction. The coefficients for each cubic are determined by requiring that cubic segment to pass through the two data points and have the same slopes as those at the two data points. The slope $\partial(P/P_S)/\partial X$ at each data point is determined beforehand by fitting a parabola through three points, the point in question and the data point on each side. Note, however, that the parabola is used to determine the slope only. Once the slopes are determined, a cubic is curve fit through two successive data points. Special consideration is given to the stagnation point (in the windward plane) in that the longitudinal slope $\partial(P/P_S)/\partial X$ is forced to be zero at this point.

After longitudinal curves are fit through the pressure data in each meridional plane, coefficients for these curve fits are stored. Then, when this subprogram is called in the heating program, the value of the pressure ratio (P/P_S) and its longitudinal derivatives $\partial(P/P_S)/\partial X$ can be calculated in each meridional plane for a specific longitudinal position (X). In order to calculate the pressure

ratio and its derivatives at a specific circumferential position (ϕ), a circumferential curve is fit through the calculated values of (P/P_S) in each meridional plane. This curve fit is accomplished by fitting parabolic arcs between successive values of P/P_S in the meridional planes. The parabolic arcs match pressure and pressure derivative $\partial(P/P_S)/\partial\phi$ at each meridional plane. This curve fit gives the value of P/P_S and $\partial(P/P_S)/\partial\phi$ at the specified body position (X,ϕ) . In order to obtain $\partial(P/P_S)/\partial X$, a second circumferential curve is fit through the calculated values of $\partial(P/P_S)/\partial X$ in each meridional plane. This curve fit is also accomplished by fitting parabolic arcs between successive values of $\partial(P/P_S)/\partial X$ in the meridional planes. This procedure is used for each prescribed body position (X,ϕ) .

3.1.7 Flat Bottom Delta Wing

Data presented by Bertram and Everhart in Reference 18 for pressure distributions on the flat bottom portion of a delta wing indicate that a Newtonian analysis does not properly predict the pressure behavior in the vicinity of the leading edge-flat bottom tangency. Spanwise distributions at low angles of attack appear to form a minimum at the shoulder, rising to a centerline value greater than the Newtonian value. (See Figure 3). At higher angles of attack the shoulder minimum becomes less pronounced and disappears at angles of attack approaching 10° . This can be seen in Figure 4. In all cases, however, the centerline value seems to be greater than the Newtonian value. This suggests the use of some analytic function or functions connecting Newtonian pressures on the leading edge with a centerline value. Development of the analytic function indicated that it was sufficient to correlate the spanwise pressure distribution in terms of only the spanwise meridional location. However, it was necessary to divide the analysis into three zones.

- Zone 1. A match point on the leading edge inboard to the shoulder.
- Zone 2. The shoulder inboard to a point on the bottom where the pressure is essentially the centerline value.
- Zone 3. The essentially constant pressure inboard to the centerline.

These zones are indicated on Figure 5 by means of the ϕ angles. ϕ_E is the location of the peak pressure, P_E , on the leading edge, or the location of the

stagnation line. ϕ_M is the match point between the modified Newtonian distribution on the leading edge and the flat bottom delta wing pressure analysis assumed to be midway between ϕ_E and the shoulder. ϕ_S locates the shoulder. ϕ_F is the point where the pressure approaches the centerline value. The distance between the shoulder and ϕ_F is an input parameter which is usually set equal to the distance from the shoulder to the match point. Note also the "crown" indicated on Figure 5. It was found necessary to provide a negative spanwise pressure gradient immediately outboard of the centerline for those cases where the shoulder pressure was less than the centerline value.

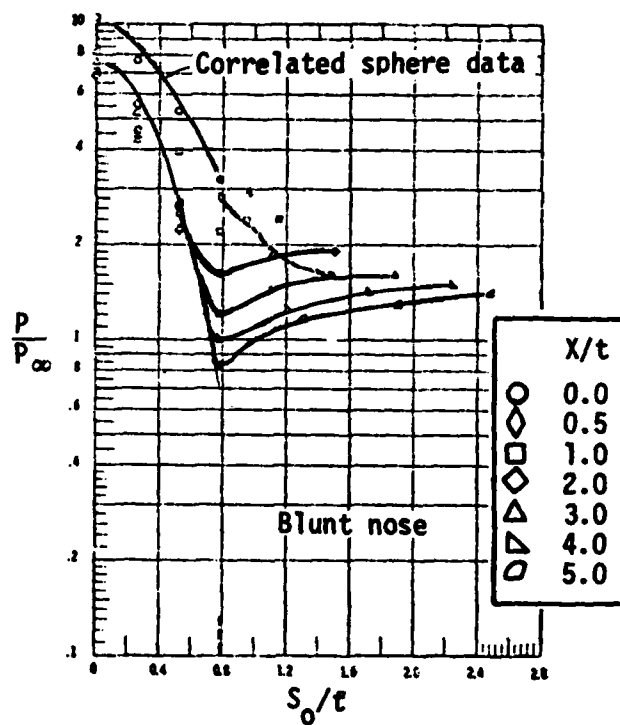


FIGURE 3 - MEASURED PRESSURE DISTRIBUTION ON WINDWARD SURFACE OF DELTA WING, 0° ANGLE OF ATTACK

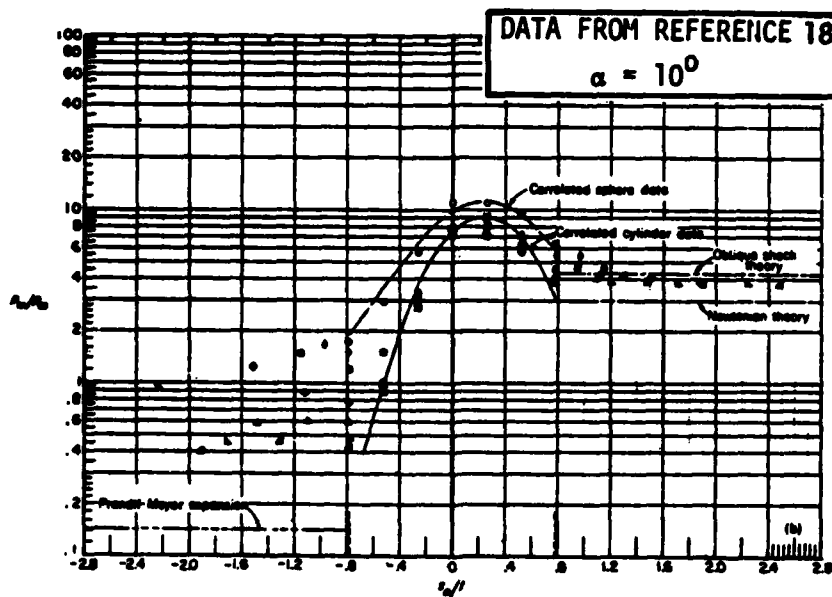


FIGURE 4 - MEASURED PRESSURE DISTRIBUTION ON WINDWARD SURFACE OF DELTA WING, 10° ANGLE OF ATTACK

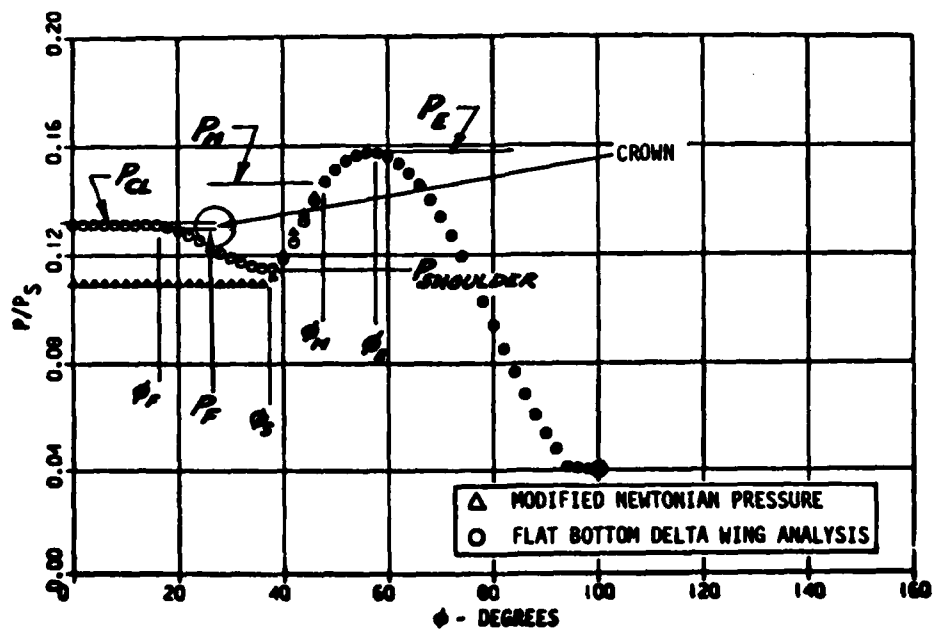


FIGURE 5 - DELTA WING PRESSURE DETERMINATION

The analytical expressions describing the spanwise distribution are a cubic for each of zones (1) and (2), and a quadratic for the nearly constant pressure zone at the centerline. The cubic takes the form

$$\frac{P}{P_s} = A \phi^3 + B \phi^2 + C \phi + D \quad (25)$$

The derivative is obtained by merely differentiating Equation (25).

$$\frac{\partial(P/P_s)}{\partial \phi} = 3A \phi^2 + 2B \phi + C \quad (26)$$

In like fashion, the quadratic is

$$\frac{P}{P_s} = B \phi^2 + C \phi + D \quad (27)$$

and

$$\frac{\partial(P/P_s)}{\partial \phi} = 2B \phi + C \quad (28)$$

At any given body station the pressure and pressure derivative at the match point are known from the Newtonian distribution. The pressure at the centerline, at ϕ_F , and at the shoulder are also known, and the derivatives at the centerline and at the shoulder are both set equal to zero. These boundary conditions are sufficient to determine the coefficients of the appropriate expression for each zone. At body stations in the near nose region the centerline pressure may be equal to or greater than the maximum pressure on the leading edge. For such a condition, the multi-zone analysis yields unsatisfactory arithmetic results. It is therefore necessary to fit a single cubic equation between the centerline and the maximum pressure on the leading edge.

An expression for the centerline pressure is suggested by the work of McElderry in Reference 19.

$$\frac{P_{CL}}{P_S} = \frac{T}{\left(\frac{X}{D_{NOSE}} + \frac{S}{D_{NOSE}} \right)} + \frac{P_{ASYMPT}}{P_S} \quad (29)$$

and

$$T = 0.067 M_\infty^2 \left(\frac{P_\infty}{P_S} \right) \quad (30)$$

where

P_{ASYMPT} = asymptotic value of pressure at $X = \infty$
 S = factor to make expression match with Newtonian

Data from both McElderry and Bertram and Everhart indicate that a tangent cone pressure be used for the asymptotic value in the range of conditions valid for this study. Equation 29 must be used to match with a Newtonian distribution in the stagnation region by varying the factor S . A typical centerline distribution is shown in Figure 6.

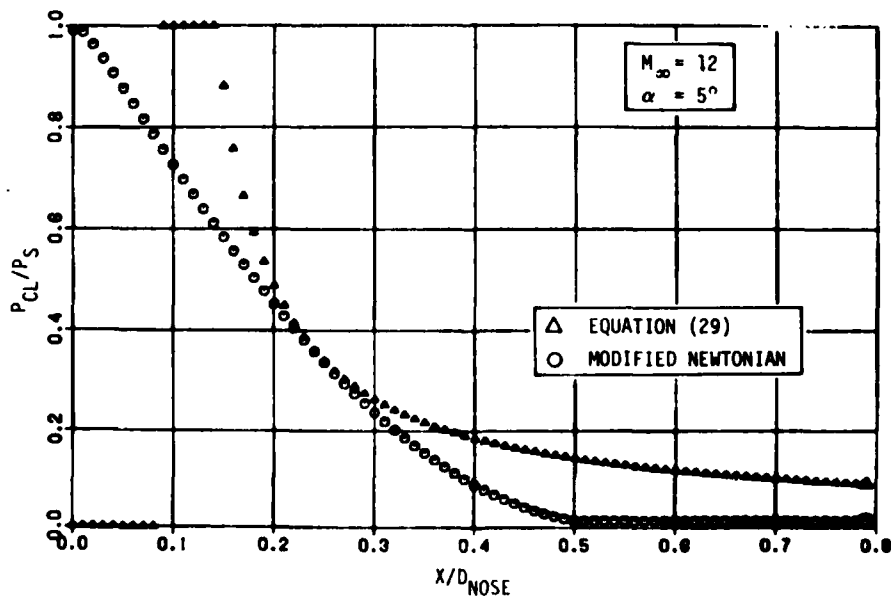


FIGURE 6 - WINDWARD CENTERLINE PRESSURE DISTRIBUTION ON DELTA WING

Completing the flat bottom delta wing pressure analysis is a correlation of the shoulder to centerline pressure ratio. A comparison of the centerline and shoulder pressures at typical conditions is presented in Figures 7, 8, and 9 for angles of attack of 0° , 5° , and 10° , respectively. These data were extracted from Reference 18. There is very little difference between the two pressures at 10° angle of attack, as can be seen from Figure 9. At some axial distance less than 8 nose diameters from the vertex of the delta all the pressures become constant. Additional data from Reference 18 are included in Figure 10, which presents the ratio of the shoulder to centerline pressure for a range of conditions. It is seen from Figure 10 that each curve may be approximated by two straight lines. One line varies between a pressure ratio of 1.0 at $X/D_{\text{NOSE}} = 0$ and some lesser pressure ratio, Q_M , at $X/D_{\text{NOSE}} = X_C$. The second straight line is constant valued at Q_M for X/D_{NOSE} greater than X_C . Within the range of conditions examined, the minimum shoulder to centerline pressure ratio, Q_M , is a function of Mach number and Reynolds number, and is assumed to be a linear function of angle of attack, such that Q_M is equal to 1.0 when the angle of attack is greater than 10° and Q_M is equal to Q_{MM} when the angle of attack is zero. Therefore, Q_{MM} is a function of Mach number and Reynolds number. The derived equations are:

$$Q_{MM} = 0.054 M_\infty - 0.46 \times 10^{-6} Re_\infty + 0.294 \quad (31)$$

$$Q_M = 0.1 \alpha (1.0 - Q_{MM}) + Q_{MM} \quad (32)$$

The axial location, X_C , beyond which the pressure ratio remains constant is correlated as a function of Q_M and is shown in Figure 11.

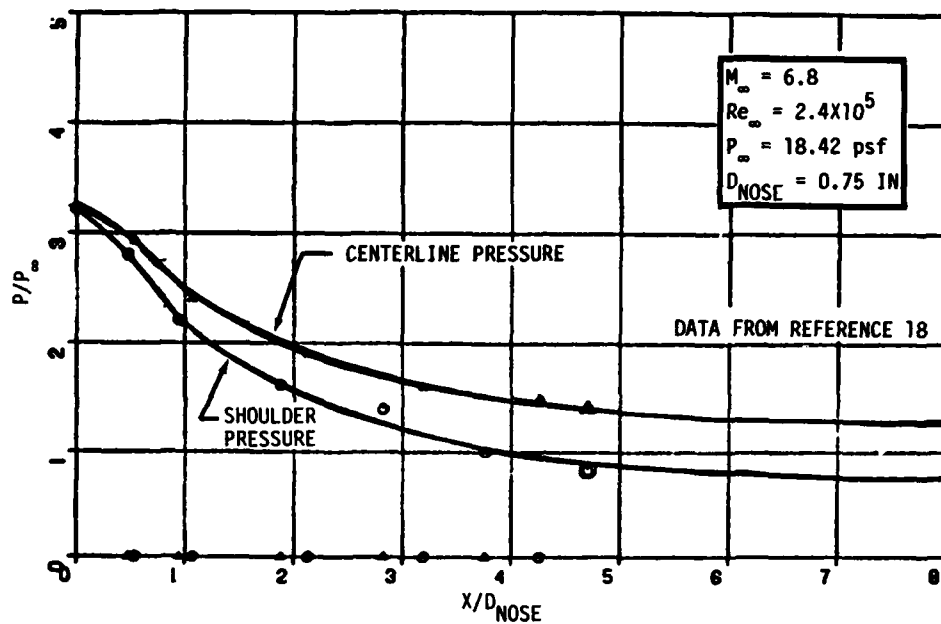


FIGURE 7 - COMPARISON OF CENTERLINE AND SHOULDER PRESSURES,
0° ANGLE OF ATTACK

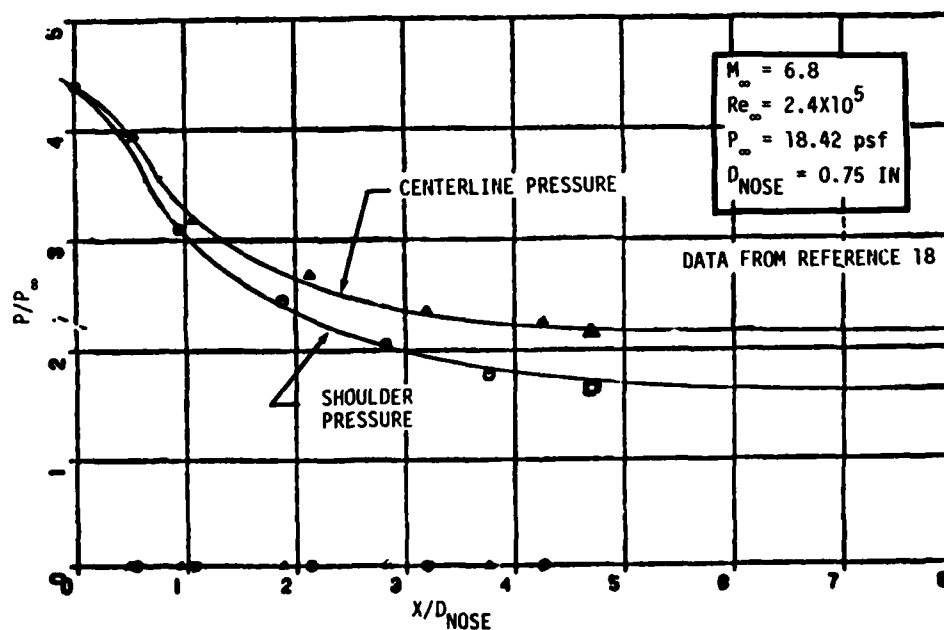


FIGURE 8 - COMPARISON OF CENTERLINE AND SHOULDER PRESSURES,
5° ANGLE OF ATTACK

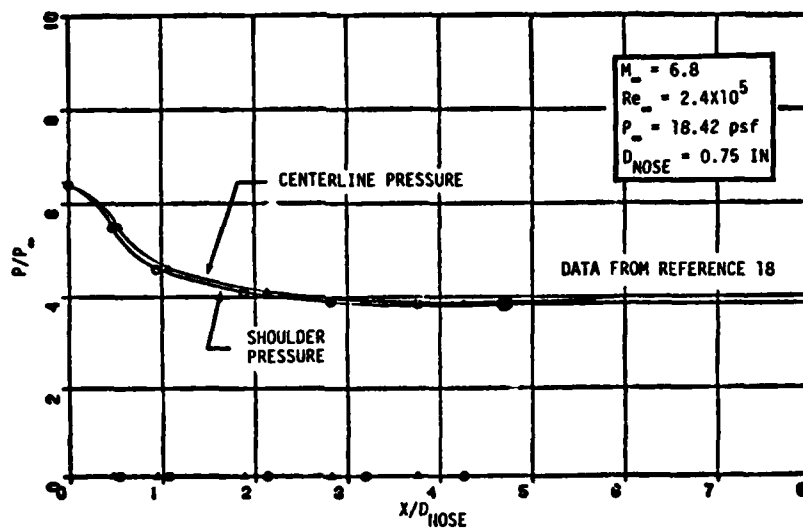


FIGURE 9 - COMPARISON OF CENTERLINE AND SHOULDER PRESSURES, 10° ANGLE OF ATTACK

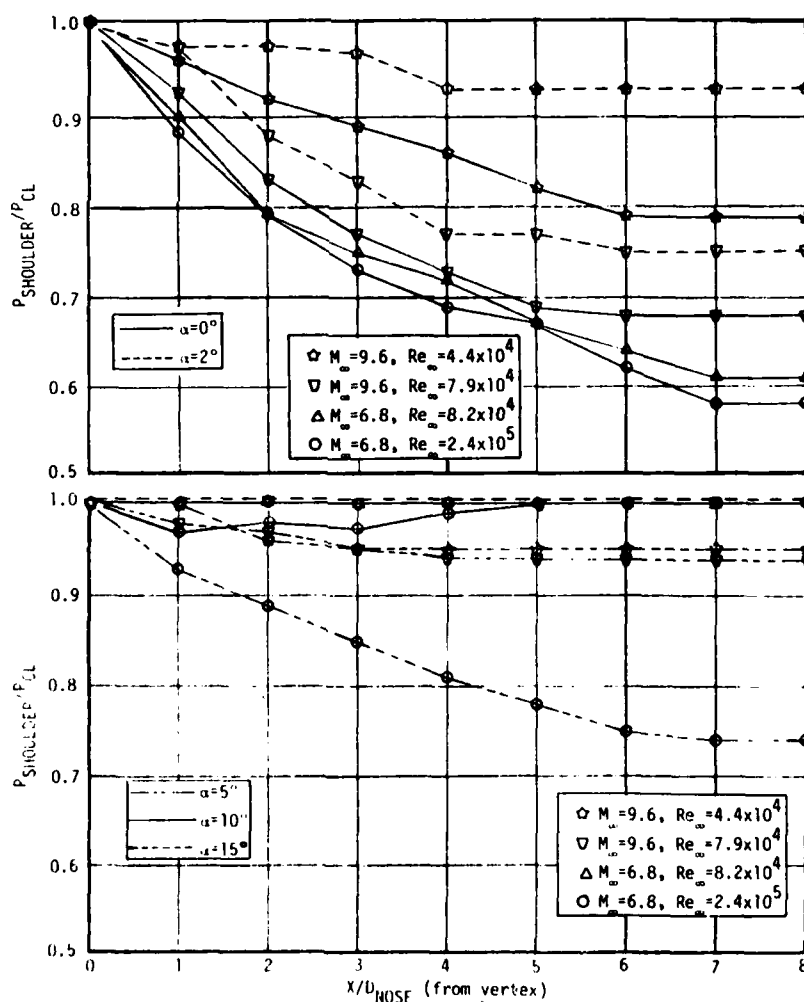


FIGURE 10 - SHOULDER PRESSURE CORRELATION

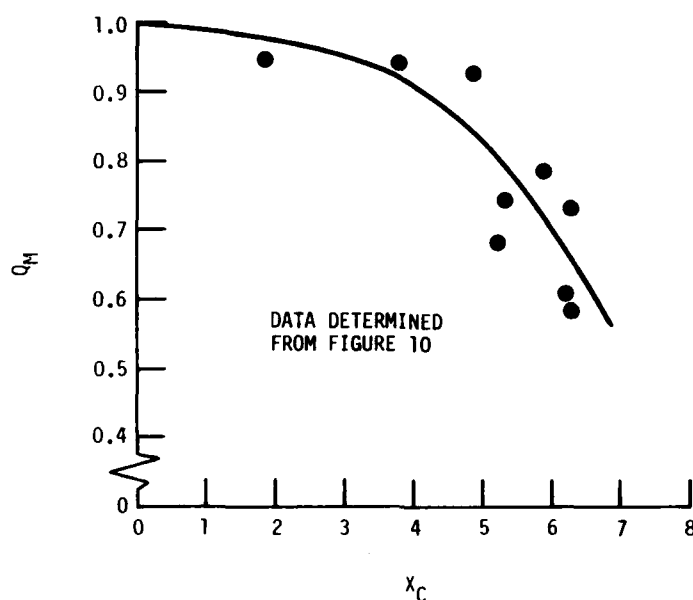


FIGURE 11 - POSITION OF CONSTANT SHOULDER PRESSURE RATIO

Typical spanwise pressure distributions on the bottom of the X-24C for the case presented in Section 6 are shown in Figures 12 through 18. The Newtonian pressure distribution is included on the figures for comparison. Data are for two angles of attack, 4° and 12° ; however the flat bottom is inclined an additional 3.27° to the free stream. The leading edge vertex is at $X = 2.73$. Figures 12 and 16 are for an upstream axial location where the centerline pressure is greater than the peak pressure on the leading edge. Figures 13 and 17 are for a location where the centerline pressure and the peak pressure on the leading edge are nearly equal. Figure 14 represents a station where ϕ_F is close to the centerline. Figures 15 and 18 are at downstream locations where the ratio of shoulder to centerline pressure is constant. For the 12° angle of attack, however, the shoulder pressure equals the centerline pressure.

The Bertram and Everhart data are for one sweep angle only-- 70° --and any attempt to apply the above correlations to other sweep angles requires verification. The Mach number range for the data in the correlation is 6.8 to 9.6, and the Reynolds number range is 4.4×10^4 to 2.5×10^5 .

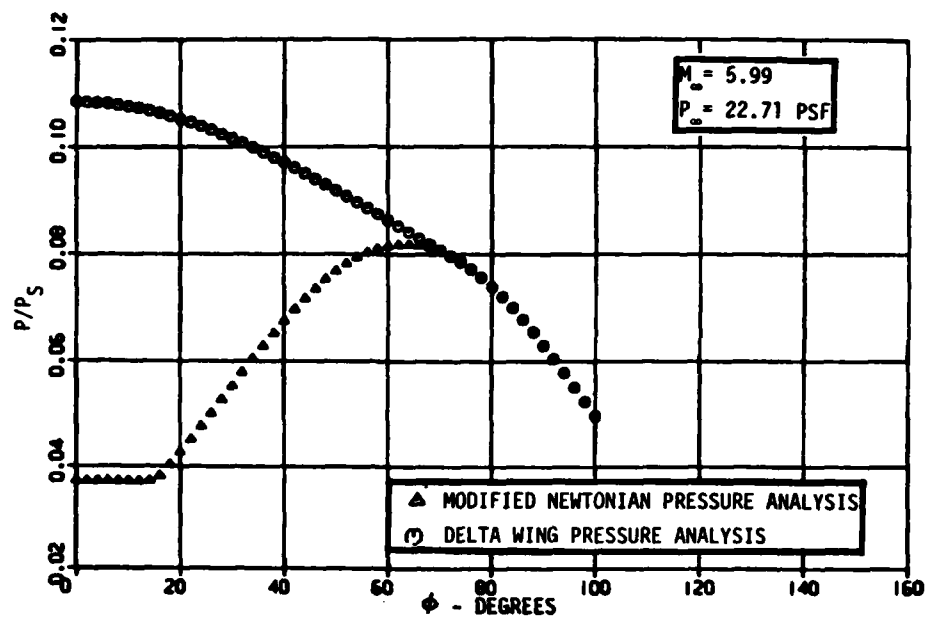


FIGURE 12 - SPANWISE PRESSURE DISTRIBUTION,
4° ANGLE OF ATTACK, X = 8 INCH

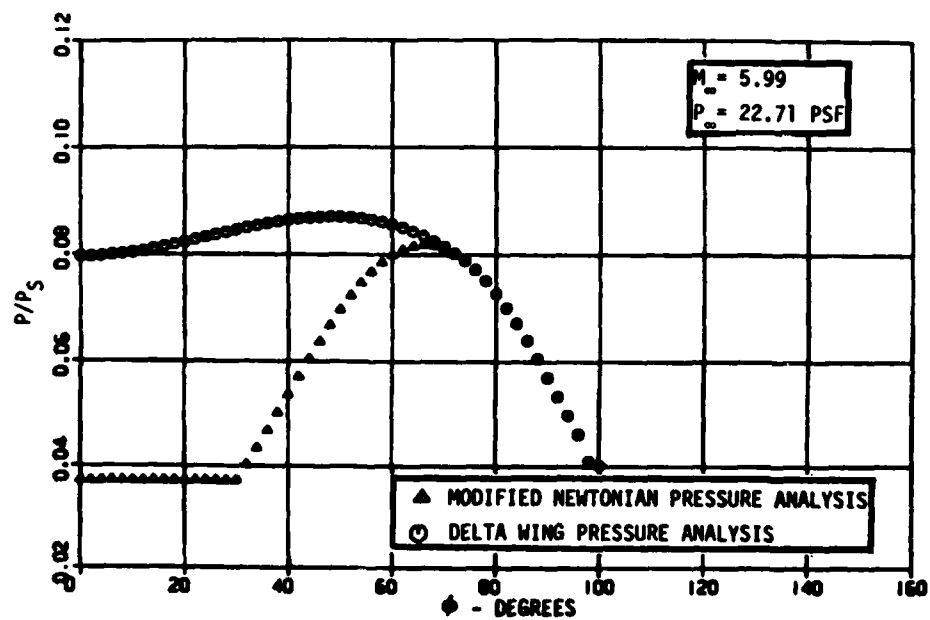


FIGURE 13 - SPANWISE PRESSURE DISTRIBUTION,
4° ANGLE OF ATTACK, X = 15 INCH

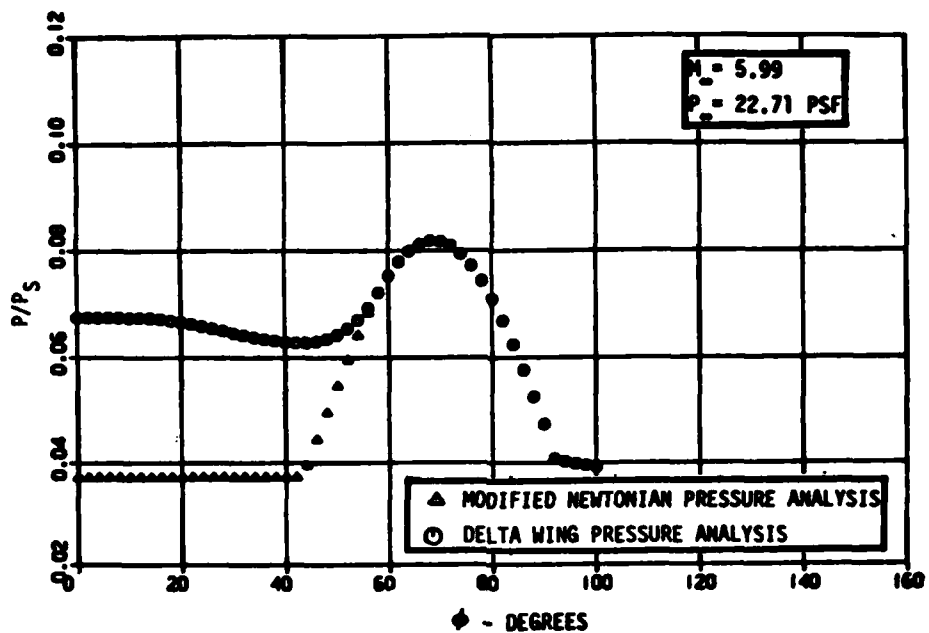


FIGURE 14 - SPANWISE PRESSURE DISTRIBUTION,
4° ANGLE OF ATTACK, X = 25 INCH

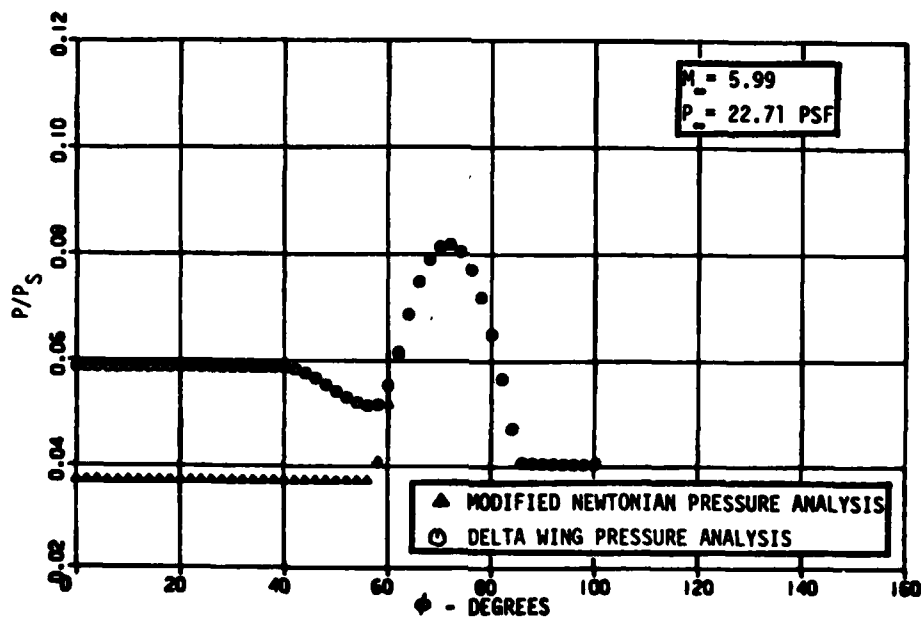


FIGURE 15 - SPANWISE PRESSURE DISTRIBUTION,
4° ANGLE OF ATTACK, X = 50 INCH

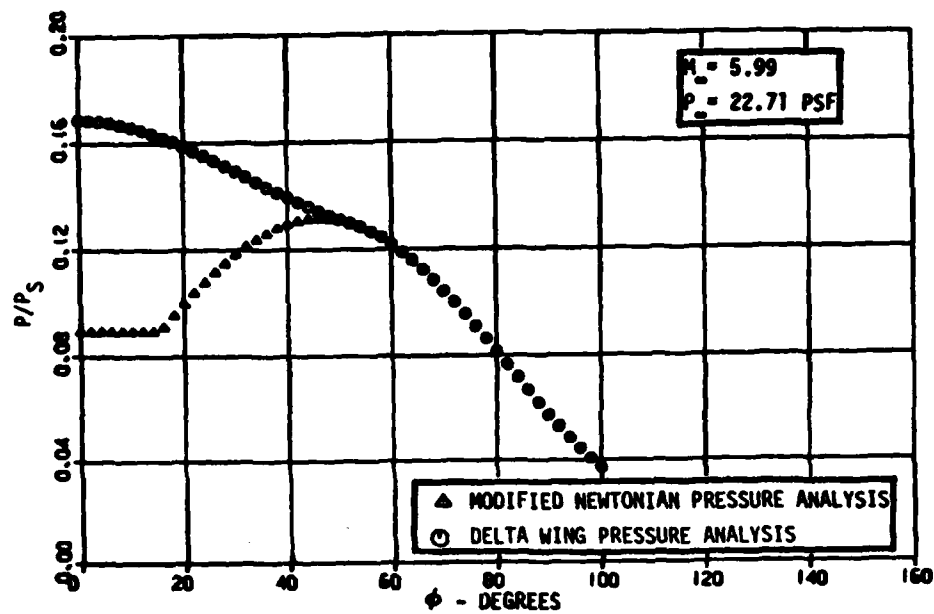


FIGURE 16 - SPANWISE PRESSURE DISTRIBUTION,
12° ANGLE OF ATTACK, $X = 8$ INCH

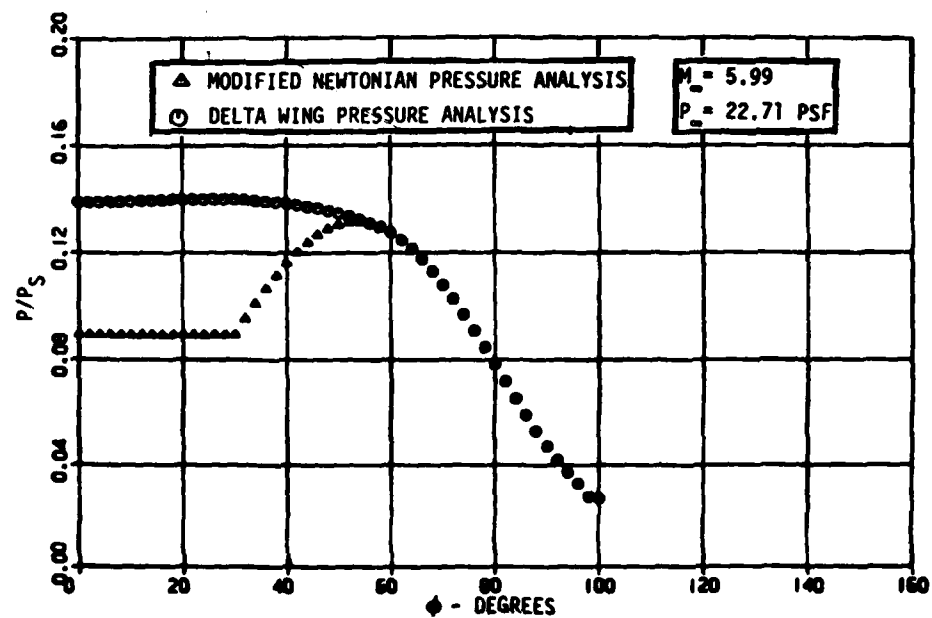


FIGURE 17 - SPANWISE PRESSURE DISTRIBUTION,
12° ANGLE OF ATTACK, $X = 15$ INCH

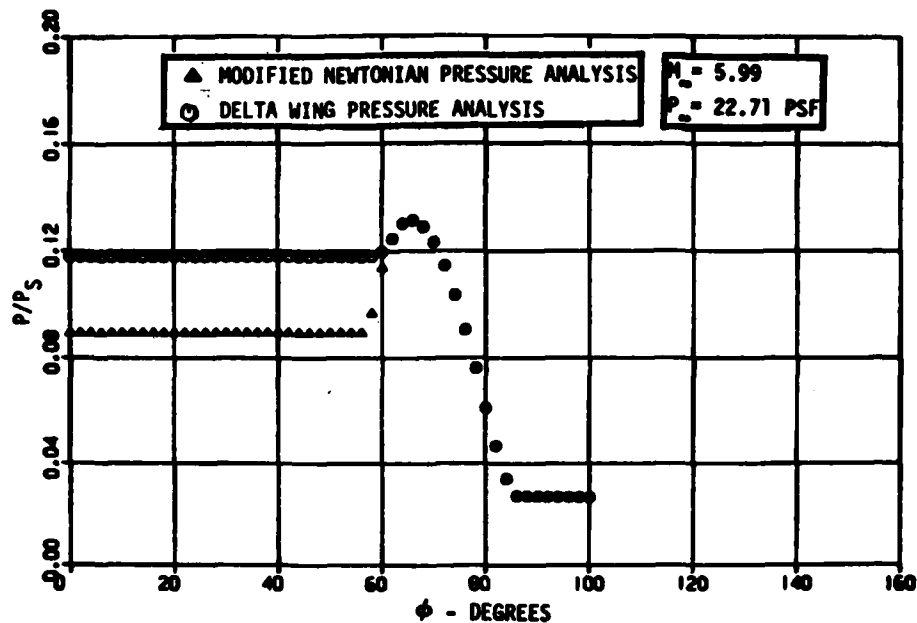


FIGURE 18 - SPANWISE PRESSURE DISTRIBUTION,
12° ANGLE OF ATTACK, X = 50 INCH

3.2 ADDED TURBULENT HEATING OPTIONS

Two routines were added to provide additional options for the local turbulent flow heating rate. One routine is the Reference Enthalpy method of Eckert. The other routine is the Van Driest method. Both methods are discussed in the following sections. Heating rates on flaps and in the vicinity of fin induced shocks are discussed in Section 3.3.

3.2.1 Eckert Reference Enthalpy

The Reference Enthalpy method for computing heat transfer is in widespread use. In effect, the heat transfer coefficient and other properties are evaluated at the temperature corresponding to a reference enthalpy, given by the following expression:

$$h^* = h_e + 0.5(h_w - h_e) + 0.22(h_{aw} - h_e) \quad (33)$$

where

e refers to boundary layer edge conditions

w refers to wall conditions

* is the reference condition

h_{aw} is the adiabatic wall enthalpy and is related to the recovery factor by

$$h_{aw} = h_e + r \frac{U_e^2}{2} \quad (34)$$

where

U_e = boundary layer edge velocity

r = recovery factor ($= Pr^{1/3}$ for turbulent flow)

A constant value of 0.725 is assumed for the Prandtl Number, Pr . The heating rate for turbulent flow is given by

$$q = \frac{0.0296 (Re^*)^{0.8} \mu^* (h_{aw} - h_w)}{S J (Pr^*)^{2/3}} \quad (35)$$

where

S = distance along streamline from the stagnation point

J = mechanical equivalent

Pr = Prandtl number

Re = Reynolds number

Equation (35) which is valid for a flat plate gives reasonable results for turbulent heating to an arbitrary blunt body. A summary discussion of the Reference Enthalpy method is given in Reference (20) and a detailed discussion of the method may be found in the survey report by Eckert (Reference 21).

3.2.2 Van Driest

One of the options for calculating turbulent heating rates is the Van Driest II method (References 22 and 23). In this method the momentum thickness Reynolds number is obtained from the integration of the integral form of the momentum equation along an inviscid surface streamline. Then a transformed momentum thickness Reynolds number is calculated from

$$\bar{Re}_\theta = F_\theta Re_\theta \quad (36)$$

where $F_\theta = \mu_e / \mu_w$ and \bar{Re}_θ is the

transformed (incompressible) momentum thickness Reynolds number. This transformed value is used to calculate the transformed (incompressible) skin friction coefficient, \bar{C}_f , from the Karman-Schoenherr formula (Reference 23). The transformed skin friction coefficient is then converted to the compressible skin friction coefficient by the relation

$$C_f = \bar{C}_f / F_c \quad (37)$$

where

$$F_c = \left[\int_0^1 \left(\frac{\rho}{\rho_e} \right)^{1/2} d \left(\frac{U}{U_e} \right) \right]^{-2} \quad (38)$$

The expression for F_c can be evaluated in closed form for a perfect gas, but the integral must be evaluated numerically for equilibrium air. The well-known Crocco temperature distribution through the boundary layer and a temperature recovery factor of 0.9 are used to evaluate the integral for F_c .

The local skin friction coefficient is then converted to the turbulent heat-transfer rate through the von Karman form of Reynolds analogy factor.

3.3 INTERFERENCE HEATING

This program also addresses heating resulting from strong shocks produced by flaps and fins. Flap heating is characterized by flow separation and subsequent reattachment. The fin problem is characterized by localized heating in the vicinity of and influenced by the fin induced shock wave. These two interference heating methods are triggered only at the end of a streamline calculation; i.e., the last calculated streamline axial location corresponds to either the flap hinge line or the fin leading edge. Boundary layer edge conditions at that point serve as free stream conditions to the interference heating calculations. Such edge parameters include pressure, temperature, velocity, and Mach number. Other necessary parameters include boundary layer thickness, Reynolds number, and streamline direction with respect to the vehicle axis. The following sections describe the analyses for heating on a flap and the heating caused by fin interference.

3.3.1 Maximum Heating Rate on a Flap

The adverse pressure gradient caused by a flap or other compression ramp results in boundary layer flow separation for all except the smallest gradients. If separation occurs, the streamlines in the external flow will be deflected, as illustrated in Figure 19. The effect of separation is to alter the flow geometry such that the supersonic flow will undergo two stages of weak shock wave compression; separation shock and reattachment shock. The external inviscid flow and the viscous separated flow are interdependent through a pressure interaction. There remains a viscous fluid layer outside the dividing streamline which behaves much the same as a continuance of the original boundary layer and is referred to as a shear layer. The nature of the pressure rise and local flow are shown in Figure 20. It is seen that the pressure waves propagate upstream of the disturbance, allowing the pressure gradient to spread over a long distance. In this analysis, maximum heating on the deflected surface is assumed to occur at the point of reattachment. Thus, this analysis addresses itself mainly to the determination of the reattachment point.

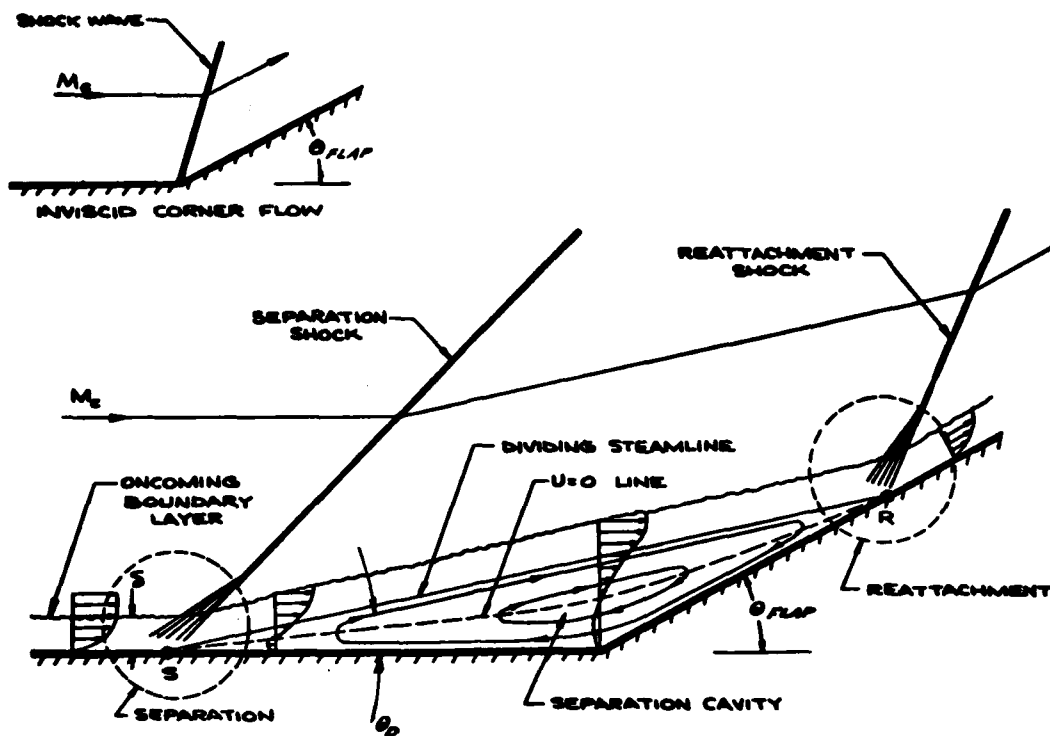


FIGURE 19 - FLOW SEPARATION IN VISCOUS CORNER FLOW

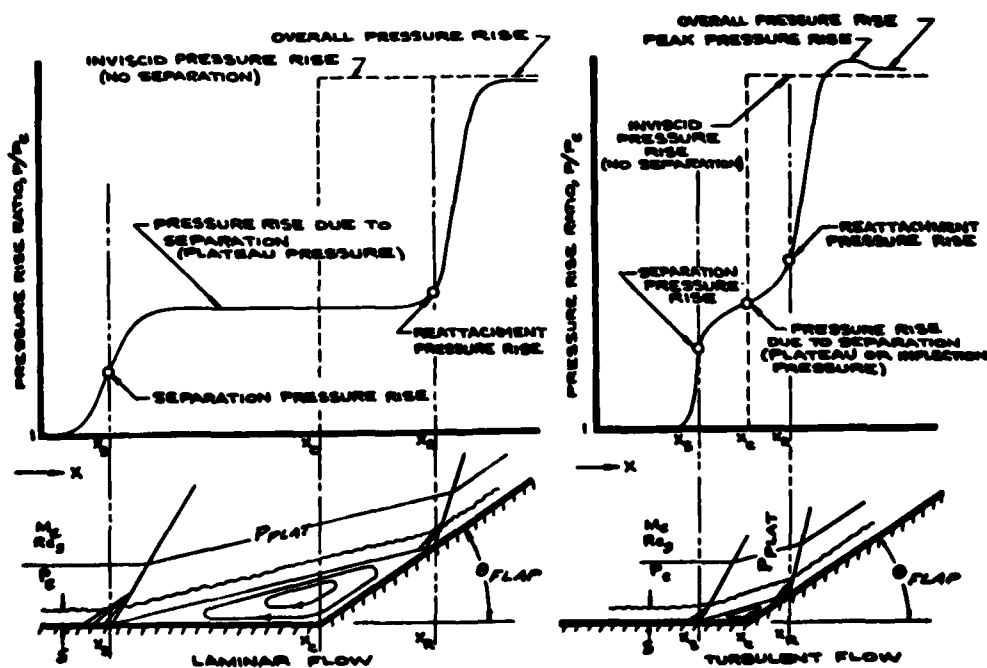


FIGURE 20 - WALL PRESSURE DISTRIBUTION IN THE VICINITY OF SEPARATION

The analysis for the maximum heating rate to a flap or other compression ramp is divided into three parts:

- (1) Determining if flow separation occurs at a particular ramp angle.
- (2) Determining the geometry of the separated region; i.e. the location of separation and the point of reattachment with respect to the ramp hinge line.
- (3) Determining the heating rate itself.

Incipient separation was analyzed by Kessler, Reilly, and Mockapetris (Reference 24). The correlation for incipient separation pressure is a function of the undisturbed boundary layer thickness Reynolds number, Re_δ , and the Mach number, M_e , and is presented in Figure 21. The wedge angle that produces incipient separation pressure is the minimum deflection angle necessary to produce separation. The oblique shock compressible flow relations of Reference 15 may be used.

$$\left(\frac{P_2}{P_1}\right)_i = \xi = 1 + \frac{\gamma}{2} C_{P_i} M_e^2 \quad (39)$$

$$\tan^2 \theta_i = \left(\frac{\xi - 1}{\gamma M_e^2 - \xi + 1}\right)^2 \frac{2\gamma M_e^2 - (\gamma - 1) + (\gamma + 1)\xi}{(\gamma + 1)\xi + (\gamma - 1)} \quad (40)$$

where

C_{P_i} = incipient separation pressure coefficient
 θ_i = wedge angle for incipient separation

The criterion for turbulent flow in the separation analysis is also seen from Figure 21. Turbulent flow occurs at values of the correlating parameter, Re_δ/M_e^3 , greater than 400.

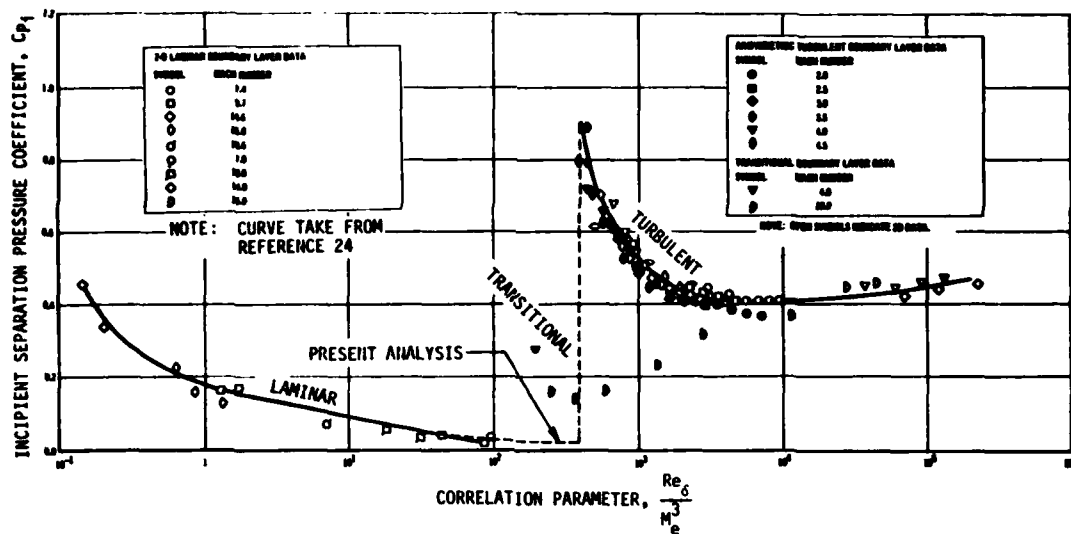


FIGURE 21 - INCIPIENT FLOW SEPARATION

The pressure behind the separation shock--indicated on Figure 20 as the plateau pressure--leads to the determination of the deflection angle of the dividing streamline. Wuerer and Clayton (Reference 25) present correlations of the plateau pressure coefficients in both laminar and turbulent flow regimes, which are reproduced here as Figures 22 and 23. The curve through the data points in each figure has been approximated by an empirical relationship.

$$\left(C_{P_{PLAT}}\right)_L = 1.60 \left[Re_s (M_e^2 - 1) \right]^{-1/4} \quad (41)$$

$$\left(C_{P_{PLAT}}\right)_T = 1.70 (Re_s)^{-1/10} (M_e^2 - 1)^{-1/4} \quad (42)$$

where

$C_{P_{PLAT}}$ = plateau pressure coefficient

Re_s = Reynolds number based on distance along a streamline to the hinge line

Equations (39) and (40) can be used with the appropriate plateau pressure parameters to determine the deflection angle of the dividing streamline, θ_D . This deflection angle is shown in Figure 24 as a function of the Mach number and Reynolds number prior to separation. The plateau pressure and other conditions behind the separation shock can be used as upstream conditions to the reattachment shock, for a wedge angle equal to the difference between the flap deflection angle and the deflection angle of the dividing streamline. In this manner, the pressure behind the reattachment shock becomes the pressure of interest on the flap and can be determined by the usual oblique shock relationships. Calculated plateau pressure and flap pressure are compared with measured data in Figure 25. The measured data, for $M_e = 2.76$, is taken from Reference 24.

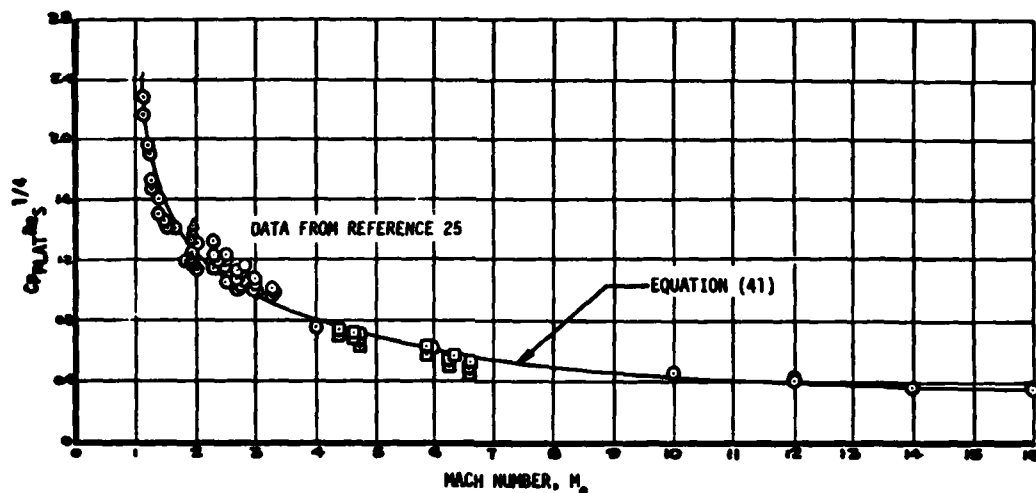


FIGURE 22 - PLATEAU PRESSURE - LAMINAR FLOW

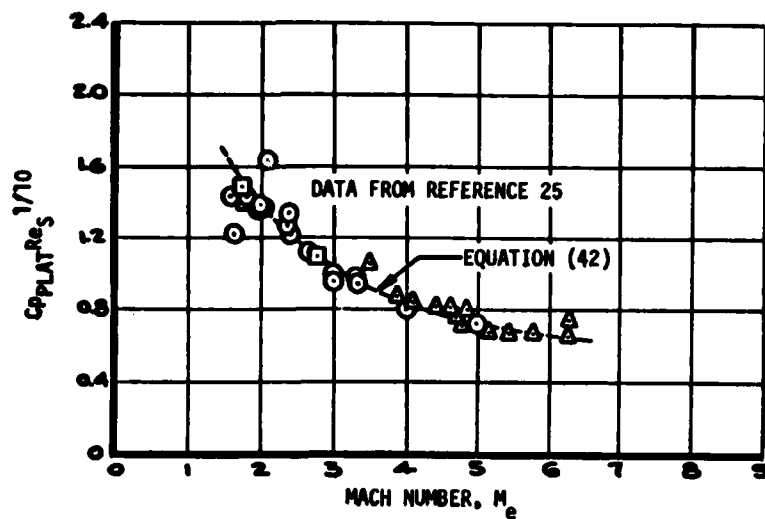


FIGURE 23 - PLATEAU PRESSURE - TURBULENT FLOW

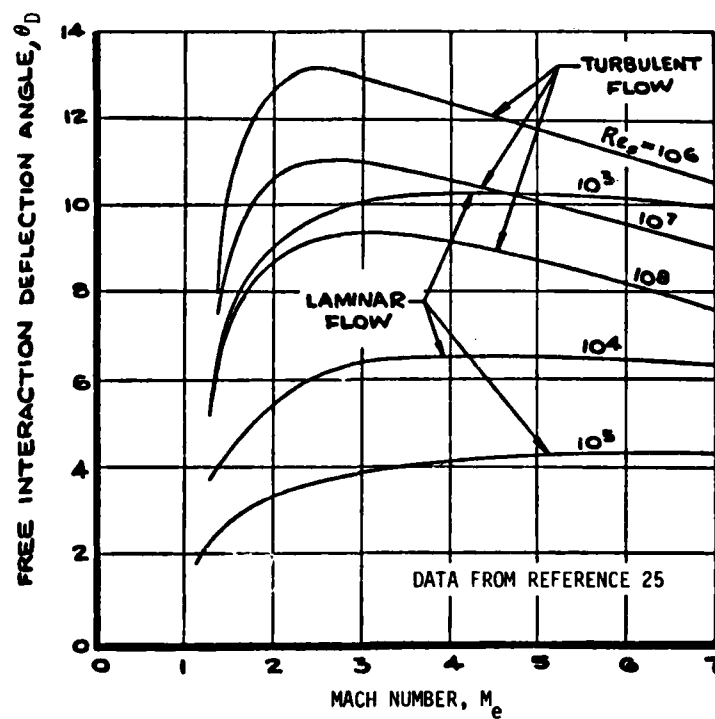


FIGURE 24 - FREE INTERACTION FLOW DEFLECTION ANGLE

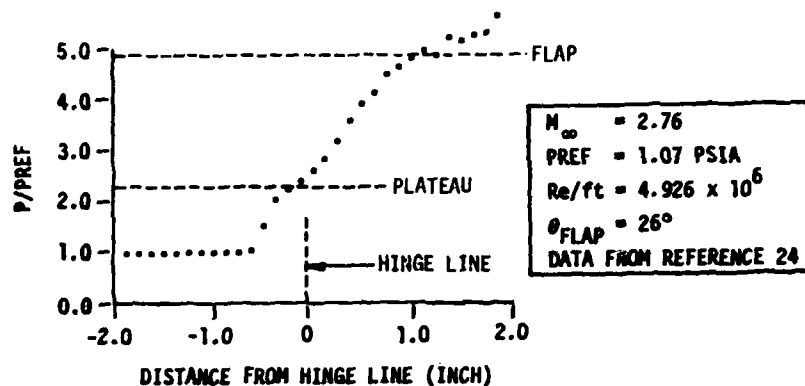


FIGURE 25 - MEASURED SURFACE PRESSURE DISTRIBUTION

The length of the separated region (or dividing streamline length) is shown in Reference 25 to be a function of certain reference parameters which are independent of the geometry; namely an effective deflection angle, θ_{REF} , reference separation length, and a reference boundary layer thickness, δ_{REF} .

$$\frac{L_{SEP}}{\delta} = \left(\frac{L_{SEP}}{\delta} \right)_{REF} \times \frac{\theta_{REF}}{\theta_D} \quad (43)$$

$$\left(\frac{L_{SEP}}{\delta} \right)_{REF} = K \left[\frac{P_{FLAP} - P_{PLAT}}{P_e} \right] \quad (44)$$

where

- L_{SEP} = length of the separated region
- P_{FLAP} = flap pressure
- P_{PLAT} = plateau pressure
- P_e = undisturbed boundary layer edge pressure ahead of hinge line
- δ = undisturbed boundary layer thickness

The following table lists the reference quantities required to make the calculation. The quantities M_{REF} , $(Re_s)_{REF}$ and K are based on experimental data

in the Mach number range from 1 to 7.

	LAMINAR FLOW	TURBULENT FLOW
$(M)_{REF}$	2.0	2.8
$(Re_s)_{REF}$	2.0×10^5	2.0×10^6
K	105	4.15
θ_{REF}	2.687° ($\gamma=1.4$)	12.84° ($\gamma=1.4$)

The separation geometry is determined from the separation length and flow deflection angle, using trigonometric considerations.

$$L_{HINGE} = L_{SEP} \times \frac{\sin(\theta_{FLAP} - \theta_D)}{\sin(180 - \theta_{FLAP})} \quad (45)$$

$$L_{FLAP} = L_{SEP} \times \frac{\sin \theta_D}{\sin(180 - \theta_{FLAP})} \quad (46)$$

where

L_{HINGE} = length from separation point to hinge line

L_{FLAP} = length along flap from hinge line to reattachment point

Bushnell and Weinstein, in Reference 26, correlate the peak heating at reattachment with a shear layer thickness Reynolds number, shown here in Figure 26. The Reynolds number is defined as:

$$Re_{SHEAR} = \frac{\rho_w U_{FLAP} \delta_{SHEAR}}{\mu_w \sin(\theta_{FLAP} - \theta_D)} \quad (47)$$

where

- U_{flap} = velocity in reattachment region
- ρ_w = density in reattachment region at wall temperature
- μ_w = viscosity at wall temperature
- δ_{shear} = shear layer thickness

Reference 26 also gives expressions for the shear layer thickness. In their approach it was assumed that the shear layer thickness was equal to the undisturbed boundary layer thickness plus the growth of a free shear layer from zero initial thickness. Hence,

$$\left(\delta_{SHEAR} \right)_L = \delta + 5.0 \left(\frac{L_{SEP} \mu_{SEP}}{\rho_{SEP} U_{SEP}} \right)^{1/2} \quad (48)$$

$$\left(\delta_{SHEAR} \right)_T = \delta + 1.6 L_{SEP} / 13 \quad (49)$$

where the subscript SEP refers to quantities evaluated in the separated region, at the plateau pressure behind the separation shock. The straight lines on the correlations of Figure 26 have been numerically fitted with the expression

$$St_{PK} = C_{st} \left(Re_{SHEAR} \right)^{n_{st}} \quad (50)$$

where

St_{PK} = Peak Station Number at reattachment

The constants in Equation (50) are listed in the following table.

	LAMINAR FLOW	TURBULENT FLOW
C_{st}	0.199	0.0204
n_{st}	-0.5	-0.2

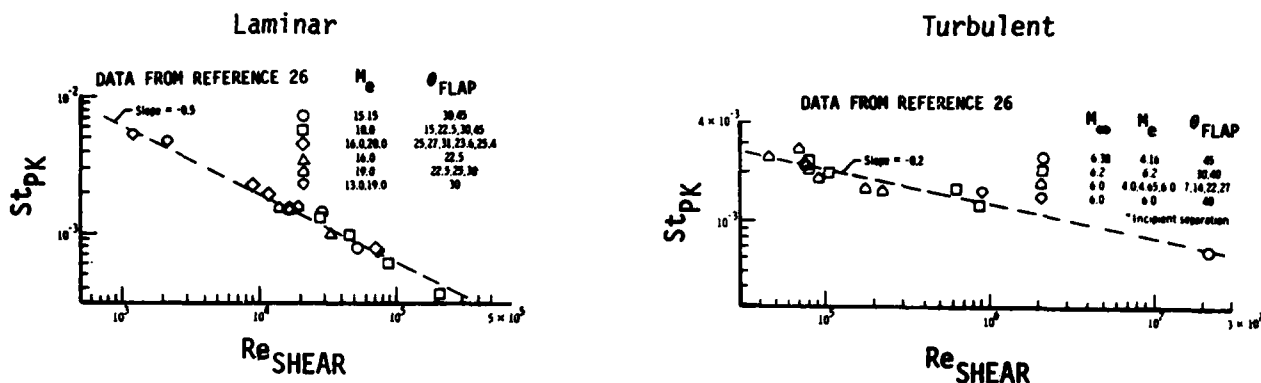


FIGURE 26 - CORRELATION OF PEAK HEATING AT REATTACHMENT

3.3.2 Fin/Plate Interaction

This section considers the interaction resulting from high speed flow around a sharp fin normal to a flat surface. The oncoming flow produces an oblique shock wave which interacts with the boundary layer on the adjacent flat surface. This interaction is depicted in Figure 27. The interaction zone can be divided into two regions--an inner region and an outer region--separated by the fin induced shock wave. The inner region is characterized by a sharp peak in the pressure and the heating rate, both of which may be several times greater than the undisturbed values. The outer region is in a turbulent separated state and the pressures may be predicted with 2-D correlations. The separation line can be identified in oil flow photographs and it was found that the pattern resembles hyperbolic curves. Figure 28 was taken from Hayes, Reference 27, and shows a typical oil flow pattern. A coordinate system for the separation line was also worked out in Reference 27, shown in Figure 29, and is approximated by asymptotes to the hyperbolic curves.

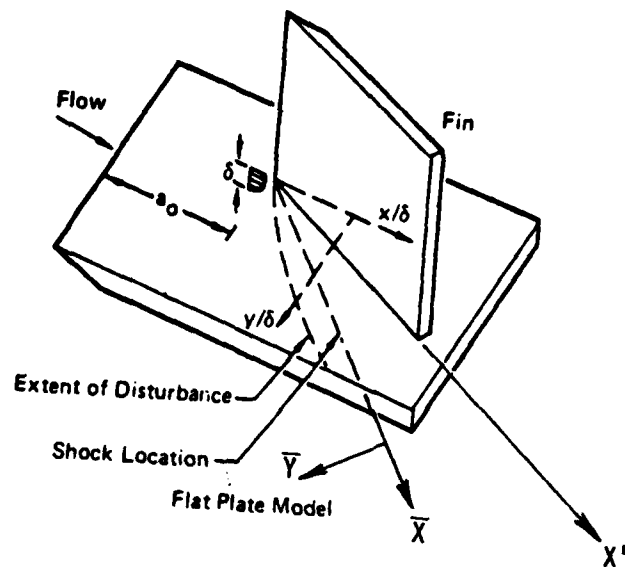


FIGURE 27 - THE 3-D INTERACTION

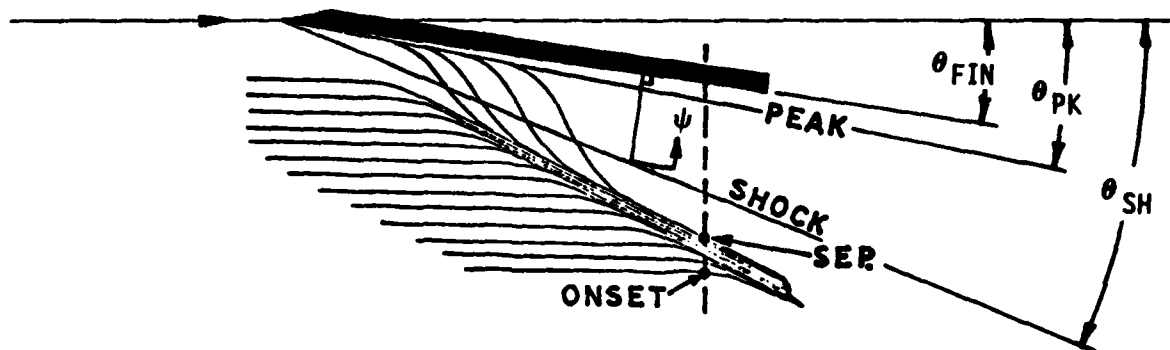


FIGURE 28 - TYPICAL OIL FLOW

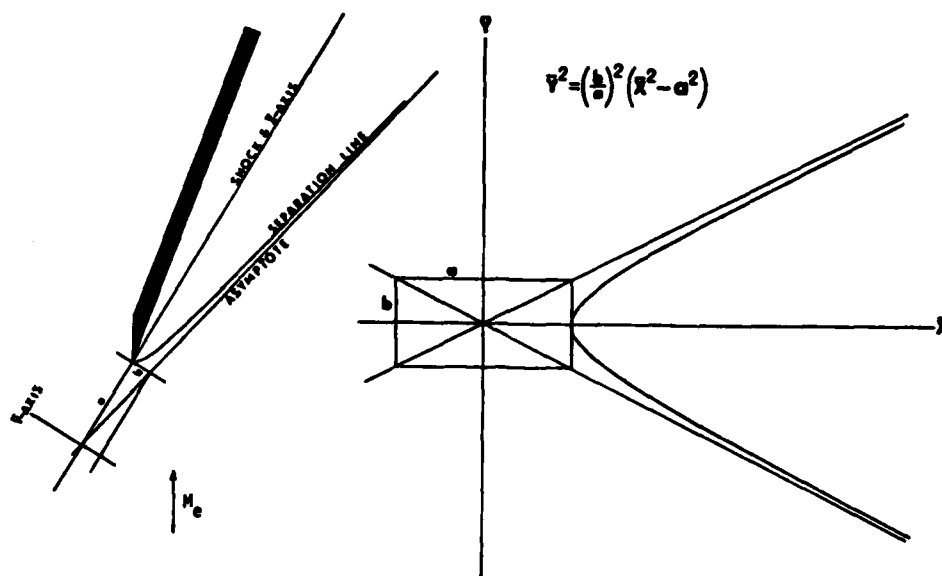


FIGURE 29 - SEPARATION LOCATION COORDINATE SYSTEM

Scuderi, too, Reference 28, has developed engineering methods for predicting three-dimensional interaction heating. A portion of that analysis is summarized here. Typical surface pressure and heat transfer profiles in the interaction flow region are sketched in Figure 30. These profiles, perpendicular to the free-stream flow direction, are presented normalized by their respective undisturbed surface values (lengths are normalized by δ). Away from the fin (at large y/δ) the flow is undisturbed and the pressure and heat transfer coefficient equal to the undisturbed value (denoted by P_e and h_u , respectively). As the free stream flow enters the interaction region, it is first compressed by initial compression waves and a pressure rise occurs between the upstream extent of disturbance and the shock wave. The increase results in either a plateau or an initial peak pressure. Eventually, a second much higher pressure peak occurs between the shock wave and the fin. This higher peak is the result of reattachment of the boundary layer. The surface heating profile generally increases more slowly (solid line) from the undisturbed heat transfer value and it also reaches a peak between the shock wave and the fin. Under certain conditions, however, an initial peak heating value (dashed line) develops between the upstream disturbance and the shock wave, as is true for the pressure profile.

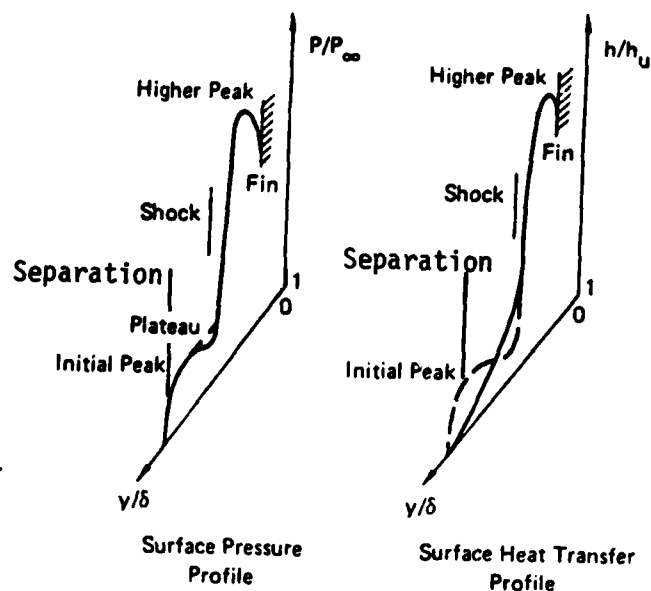


FIGURE 30 - TYPICAL SURFACE HEATING AND SURFACE PRESSURE PROFILES

The procedures for predicting pressure and heating profiles result from the fact that the pressure and heating profiles are similar. For example, both profiles have higher peaks between the shock and the fin, and under some conditions, both profiles have initial peaks between the upstream extent of disturbance and the shock. This analysis is divided into several parts, as outlined below:

- (1) determining certain distribution features
 - (a) peak pressure and location
 - (b) peak heating and location
 - (c) location of separation point and heating
 - (d) location of the shock
 - (e) location of onset of turbulent interaction zone
 - (f) plateau pressure and separation pressure
- (2) heating distribution from the peak to the shock
- (3) heating distribution from the peak to the fin
- (4) heating distribution outboard of the shock

The coordinate system used to present the heating distribution is aligned with the effective free stream to the fin, and the distributions are given normal to this free stream at various axial locations measured along the fin. The effective fin deflection angle $(\theta_{EFF})_{FIN}$, then, is determined from the streamline direction and the orientation of the fin with respect to the vehicle axis. The shock wave angle, θ_{SH} , produced by a wedge angle equal to the effective angle of attack can then be determined by the procedure presented in Section 3.1.4.

The angle defining the location of the peak pressure and peak heating is given by (Reference 29).

$$\theta_{PK} = 0.24 \left[\theta_{SH} - (\theta_{EFF})_{FIN} \right] + (\theta_{EFF})_{FIN} \quad (51)$$

The peak location and the shock location are given by

$$Y_{PK} = X' \left[\cos(\theta_{EFF})_{FIN} \right] (\tan \theta_{PK}) \quad (52)$$

$$Y_{SH} = X' \left[\cos(\theta_{EFF})_{FIN} \right] (\tan \theta_{SH}) \quad (53)$$

where

X' = location, measured along fin, see Figure 27.

θ_{PK} = angle to peak pressure and heating location, see Figure 28.

Referring to Figure 29, an equation approximating the separation asymptote is given by

$$\bar{Y}^2 = \left(\frac{b}{a} \right)^2 (\bar{X}^2 - a^2) \quad (54)$$

where

\bar{X} = distance measured along shock

\bar{Y} = distance measured normal to shock

Hayes shows that the parameters a and b in the above expression correlate well with the strength of the shock wave, which is indicated by $M_e \sin \theta_{SH}$. The correlations are presented here as Figures 31 and 32.

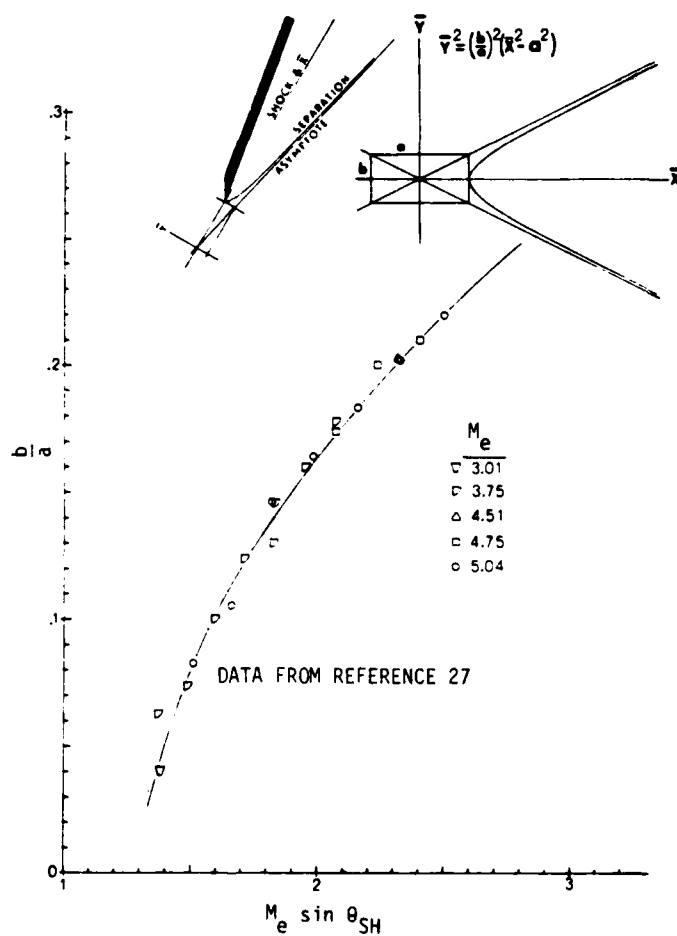


FIGURE 31 - SLOPE OF SEPARATION ASYMPTOTE

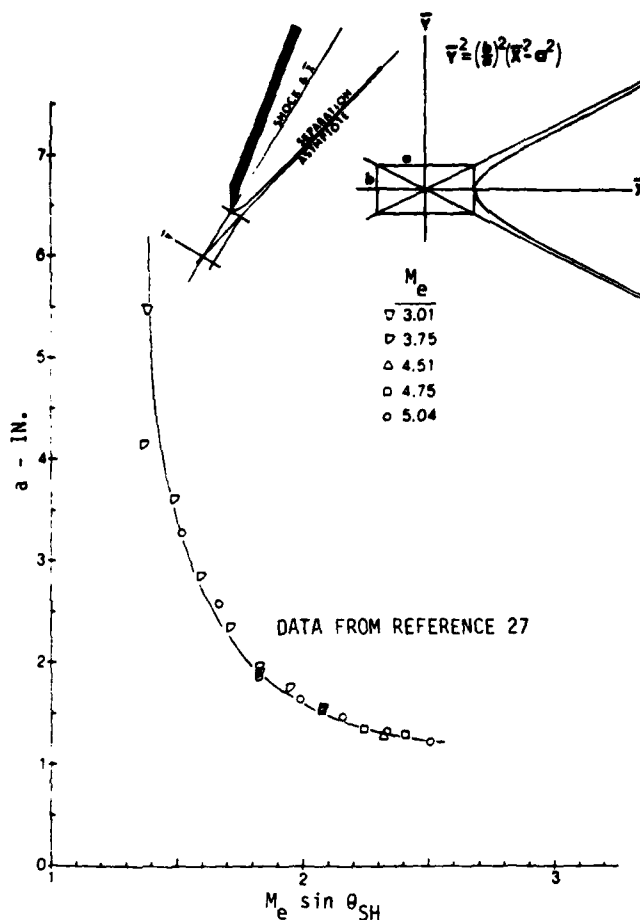


FIGURE 32 - SEPARATION ASYMPTOTE PARAMETER "a"

The outward extent of the disturbance has been correlated by Scuderi as a function of the effective angle of attack and the distance downstream of the fin leading edge. This extent is defined as the distance between the initial rise in pressure in the interaction region and the shock wave. Data for each fin deflection angle collapse to approximately one line, resulting in the following expression:

$$\frac{\Delta y}{\delta} = (0.0115 \theta_{FIN} + 0.1) \frac{x}{\delta} + 0.14 \theta_{FIN} \quad (55)$$

where

x = distance measured from fin leading edge

Δy = distance outboard of shock

The peak pressure was correlated by Hayes, indicating a relationship of the form

$$\frac{P_{PK}}{P_U} = (M_e \sin \theta_{SH})^{\eta_{PK}} \quad (56)$$

The exponent η_{PK} is a function of X/δ and is shown in Figure 33. Hayes also correlated the plateau pressure and the separation pressure. The plateau pressure is shown in Figure 34 as a function of $M_e \sin \theta_{SH}$. For purposes of this analysis, the plateau pressure correlation is reduced to the straight line

$$\frac{P_{PLAT}}{P_U} = 0.56667 (M_e \sin \theta_{SH}) + 0.83333 \quad (57)$$

and is assumed to be the value at the shock. The separation zone pressure is shown by Hayes to be a linear function of the plateau pressure, given by

$$\frac{P_{SEP}}{P_U} = 0.73 \left(\frac{P_{PLAT}}{P_U} \right) \quad (58)$$

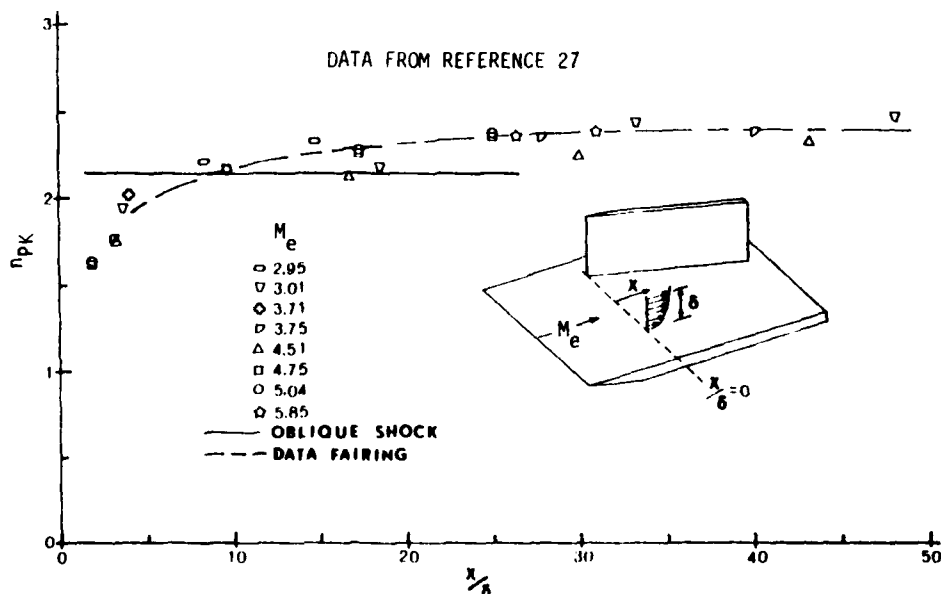


FIGURE 33 - EXPONENT IN PEAK PRESSURE CORRELATION

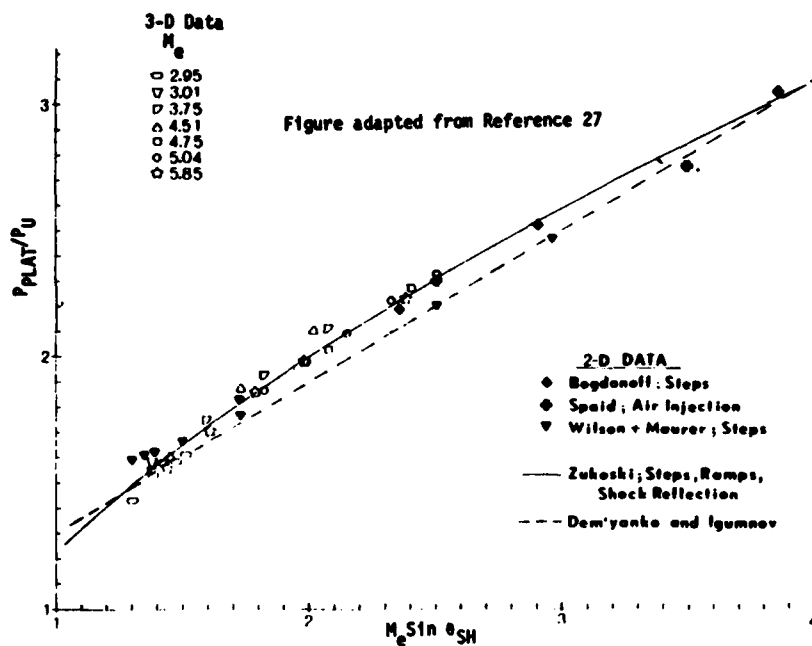


FIGURE 34 - PLATEAU PRESSURE CORRELATION

Peak heating has been correlated by Hayes in much the same manner as the peak pressure. The following expression results.

$$\frac{h_{PK}}{h_u} = [M_e \sin \theta_{SH} - 1] n_{st} + 0.75 \quad (59)$$

where n_{st} is a function of X/δ and is shown in Figure 35. Scuderi correlated the heat transfer at the location of separation with the separation pressure and presents the following expression approximating the data.

$$\frac{h_{SEP}}{h_u} = \left(\frac{P_{SEP}}{P_u} \right)^{0.85} \quad (60)$$

For purposes of this analysis the heating distribution between the shock and separation is assumed to be constant at the separation value.

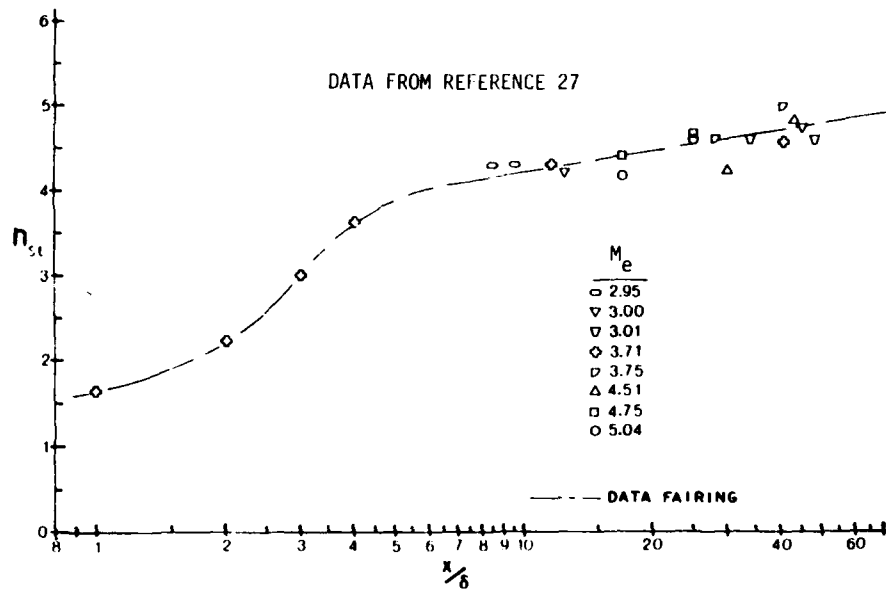


FIGURE 35 - COEFFICIENT IN PEAK HEATING CORRELATION

Hayes presents the results of an analysis by Token (Reference 29) in which Token derived equations to govern the heat transfer distribution between the peak and the shock locations. The expression is

$$\frac{h - h_{SH}}{h_{PK} - h_{SH}} = 1 - \left[1 - \frac{\psi}{\psi_{PK}} \right]^{\frac{4.7+3}{5}} \left(1 + C \frac{\psi}{\psi_{PK}} \right)^{0.8} \quad (61)$$

where ψ is the Y-coordinate measured from the shock normal to the fin, see Figure 28. The constant C in the expression is the pressure gradient parameter given by

$$C = \frac{P_{PK} - P_{SH}}{P_{SH}} \quad (62)$$

Because it has been assumed that the heating distribution between the shock and separation is a constant, the slope of the heating distribution curve must be set equal to zero at $\psi/\psi_{PK} = 0$ even though this contradicts experimental evidence given in Reference 29. Consequently, the value of n in the exponential terms must be adjusted accordingly. Thus, by differentiating Equation (61) and setting the resultant expression to zero at $\psi/\psi_{PK} = 0$, we find

$$n = C - \frac{3}{4} \quad (63)$$

As can be seen, the heating distribution from the peak to the shock is a function of both the pressure and the heating at the peak and at the shock. The heating distribution from the peak to the fin, then, is the mirror image (in absolute Y) of the distribution from the peak to the shock. The heating rate is considered constant from the separation point to the shock, at the separation value. The heating distribution is linear between onset and the separation point, the undisturbed value being used at onset.

Results of the computation for a sample case are shown in Figure 36. The example is taken from Scuderi. His calculation, along with measured data, are compared with the present calculations.

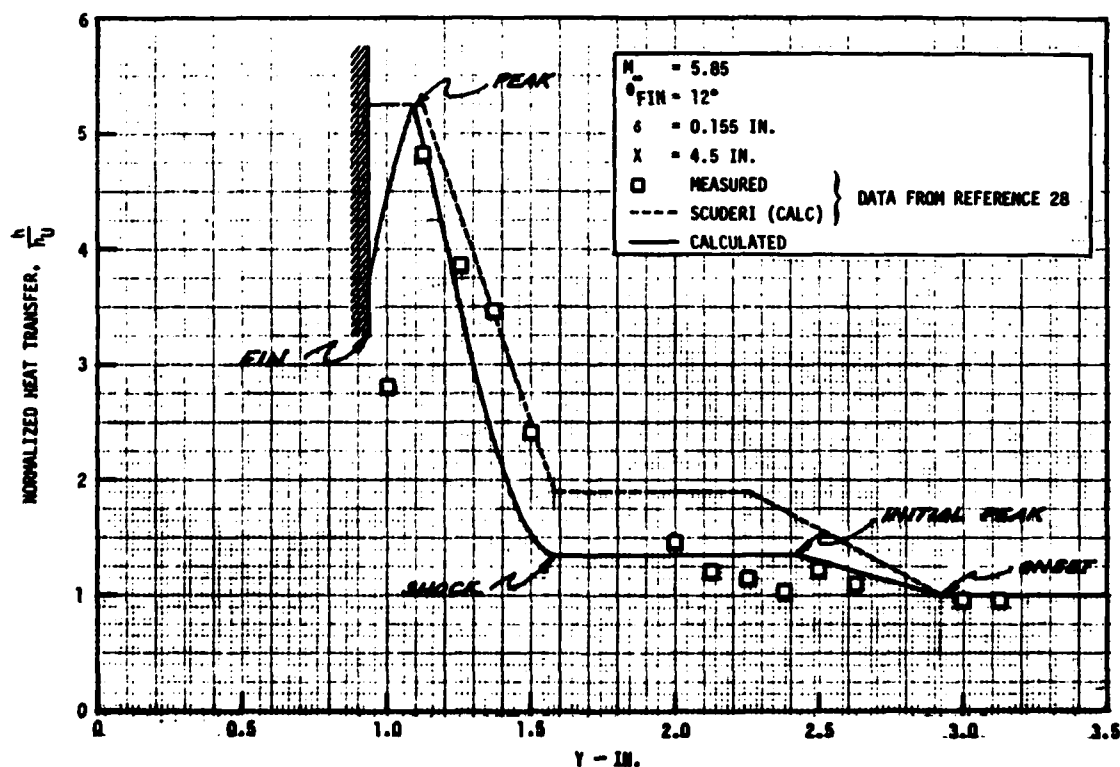


FIGURE 36 - HEATING PROFILE WITH 3-D INTERFERENCE

SECTION IV

SURFACE FITTING 3-D BODIES

Two auxiliary computer codes are provided with the main heating program to aid in the geometric description of the body to be analyzed. The first of these codes is the geometry program itself which generates details of the surface from coordinates of points in several cross-sectional planes or from loft line data. This program does curve-fitting and generates the coefficients input to the heating code in the proper format. It is coded in such a way that many of the routines are common also to the heating program. Included in the program is the user option to verify the fits at selected circumferential locations and body stations in parametric form.

The second of the two auxiliary programs is a translator code which operates on geometric data in a particular format, specifically Hypersonic Arbitrary Body Program (HABP) format, to set up the data in the proper format for the geometry code. HABP format is described in References 2 and 3. Geometry data in HABP format, in general, are used by other groups interested mainly in aerodynamic characteristics. The translator code was written to enable the individual to use the same set of geometric data for both the aerodynamic and the heating calculations with a minimum of additional input.

The following sections describe the methods employed by these two programs. Included are a brief description of the geometry method by both cross-section coordinates and loft lines, a recent improvement in fitting the longitudinal variations, and a discussion of the translator code. Actual input and output from these programs, along with examples, are discussed in Sections 2 and 3 of Volume II.

4.1 GENERAL DESCRIPTION OF GEOMETRY METHOD

A computer program was developed in Reference 30 for generating the geometry of three-dimensional bodies from coordinates of points in several cross-sectional planes. In that method, segments of general conic sections are curve fit in a least-squares sense to the points in each cross-section. These segments of general conic sections are constrained to have continuous circumferential slopes

at their boundaries, unless slopes are input at the boundaries. Figure 37 illustrates this concept. The specific conic section for each segment can be defined by the two points at the ends of a segment (called control points), an intermediate point on the curve and a slope point which is tangent to the curve at the two end points (control points). See Figure 38. These four (4) points are used to define the conic section for each segment around the circumference in a cross-sectional plane.

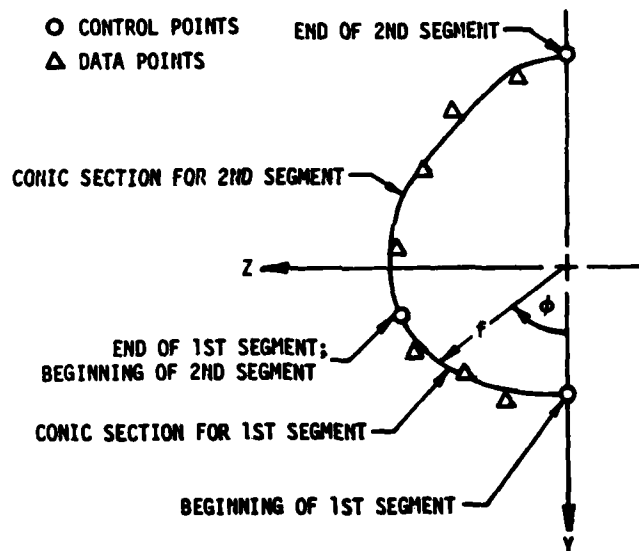


FIGURE 37 - CURVE FIT IN CROSS-SECTIONAL PLANE

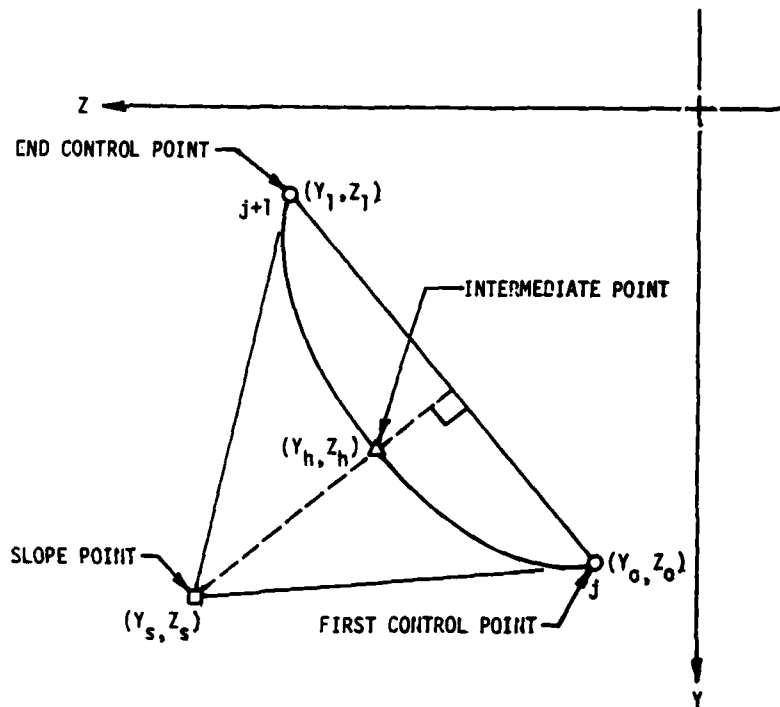


FIGURE 38 - FOUR DATA POINTS USED TO DEFINE THE CONIC SECTION FOR THIS SEGMENT

The longitudinal variation of the input cross sections is determined by fitting a three-dimensional curve in the longitudinal direction through each of the four points used to define a conic section for a cross-sectional segment (see Figure 39). Then for a value of x between the input cross-sectional data, the coordinates of these four longitudinal lines will determine the conic section in the cross-sectional plane at that value of x . Unlike curve fitting the input coordinates in the cross-sectional planes, the three-dimensional longitudinal curves must pass through each of the corresponding points in all the cross-sectional planes. Each three-dimensional longitudinal curve is represented by two planar curves by projecting it onto the x - y and x - z planes. In Reference 30 the parametric method of cubic splines was used to spline fit each planar curve, with the chordal distance between the coordinate points as the independent parameter.

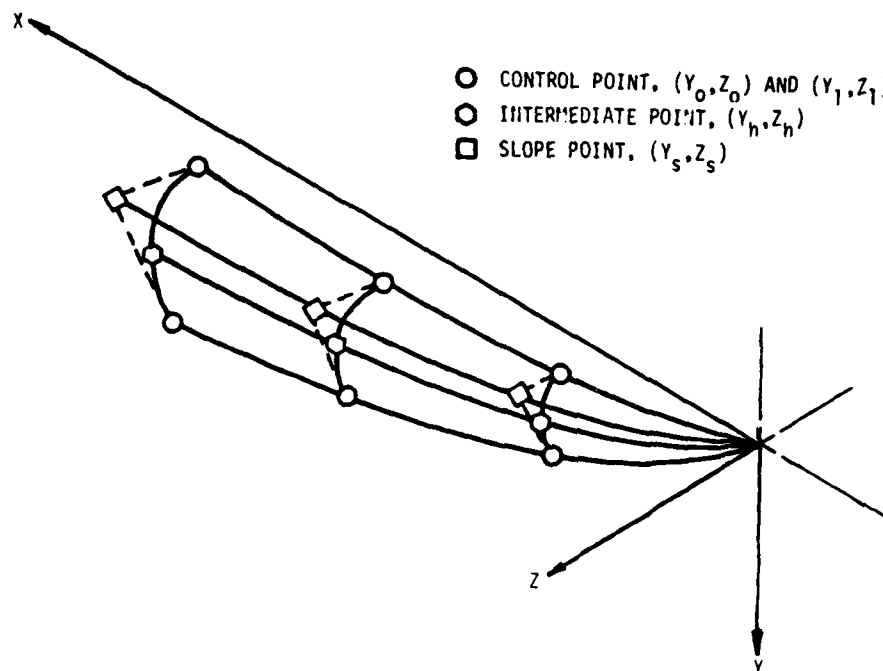


FIGURE 39 - LONGITUDINAL CURVES THROUGH THE FOUR POINTS
USED TO DEFINE THE CONIC SECTION FOR THE SEGMENT

4.2 IMPROVEMENT TO LONGITUDINAL FITS

The method used in Reference 30 for curve fitting general conic sections to input coordinates in cross-sectional planes has been found to give good results. However, the parametric method of cubic splines used to curve fit the three-dimensional longitudinal curves was found to be unsatisfactory for a number of geometries tested. Therefore, a new method was developed for fitting these longitudinal curves. As before, each three-dimensional curve is represented by the two planar curves obtained by projecting it onto the x-y and x-z planes. Each planar curve is defined by a cubic equation in the x-coordinate between two successive cross-sectional planes where input coordinates are prescribed. However, the slope of the longitudinal curve passing through these cross-sectional planes is determined by fitting a parabola through the point in question and the two corresponding points in the input cross-sectional planes on both sides of that one (see Figure 40). In this fashion the cubic equation used to represent the curve

between two consecutive longitudinal points is determined from the coordinates of the two points and the longitudinal slopes at those two points. In this procedure the possibility of having discontinuous slopes is not admitted. The longitudinal curves will also be continuous and have continuous slopes unless a discontinuity in slope is input to the program. This method of representing the longitudinal lines was found to yield better results than the method of cubic splines. Although the cubic splines have continuous second derivatives in the longitudinal direction, unwanted wiggles frequently occurred. The new method avoids most of the wiggles but it does not constrain the second derivative to be continuous. As in Reference 30, if the new method should yield longitudinal curves which are unsatisfactory, they may be modified by specifying slopes at longitudinal stations or specifying selected longitudinal curves as straight lines. In addition, the longitudinal curves in the nose region of blunt-nosed bodies are represented by ellipses rather than cubic equations. Therefore, the infinite slope at the nose of a blunted body causes no difficulty.

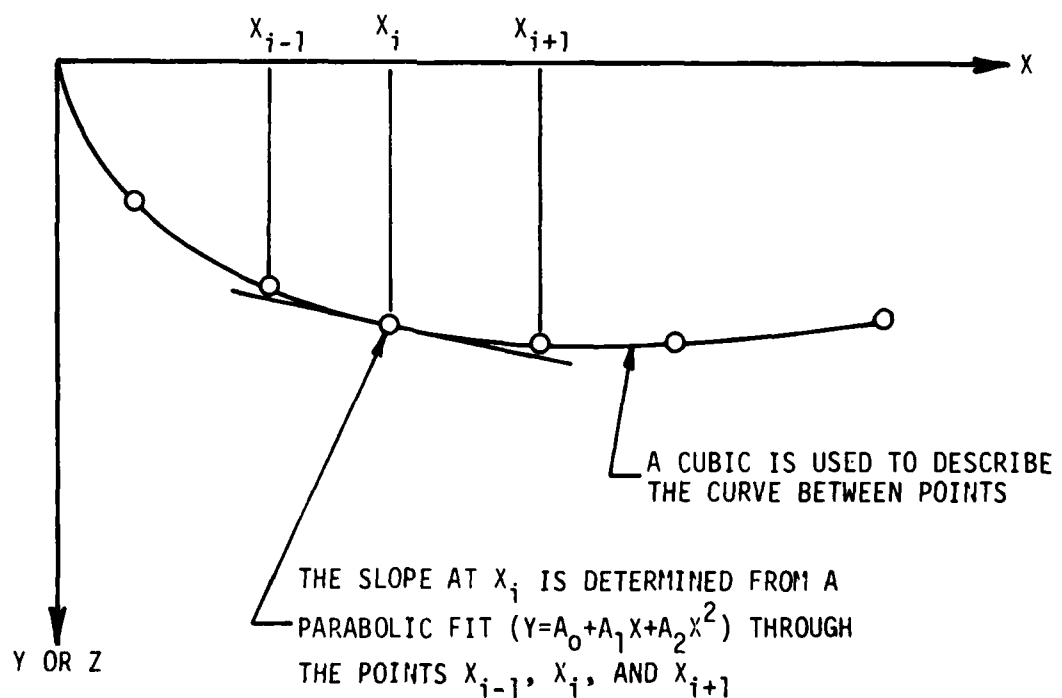


FIGURE 40 - SLOPE DETERMINATION FOR LONGITUDINAL CURVES

4.3 GEOMETRY USING LOFTING TECHNIQUES

As an alternate method for describing the geometry of three-dimensional bodies, additional routines were developed using lofting techniques to describe the cross-sectional shape. In some lofting techniques the cross-sectional curve of the body consists of alternate segments of straight lines and circular arcs as shown in Figure 41. Here the cross-section can be represented by just the end points of each segment (control points). Special consideration must be given to the circular arc segments if they are to be tangent to the adjacent straight-line segments. Since only the two end points and the slope at one end point are sufficient to determine a circular arc, this circular arc may not be tangent to the straight line at the other end point as shown in Figure 42. In order to force the arc to be tangent to the two adjacent straight line segments, an elliptical arc is used here in place of the circular arc so that it will pass through the two end points and be tangent to the straight-line segments at both end points. Note that the elliptical arc may be a circular arc if the appropriate end points (control points) are selected for a cross section. Three-dimensional longitudinal curves are fit through corresponding control points using the same method as described in the previous section. Note, however, that each segment in a cross-sectional plane here is defined by two points whereas the geometry technique

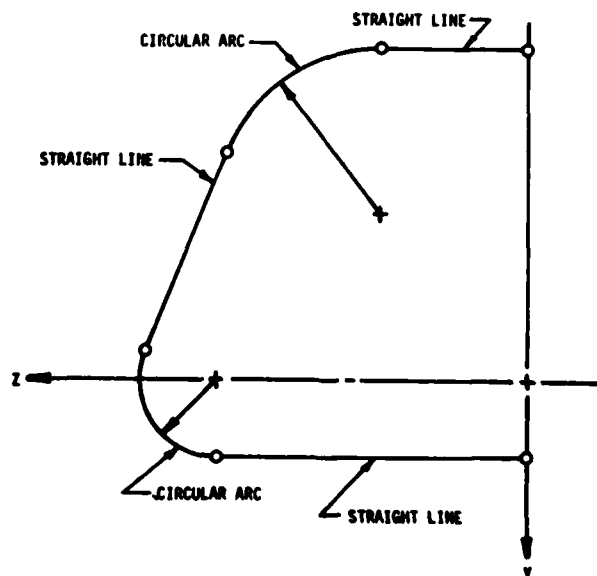


FIGURE 41 - BODY CROSS SECTION USING LOFTING TECHNIQUES

described in the previous section required four points. In addition, the conic shapes here are straight lines or ellipses, and therefore the least squares curve fit to input coordinates, used in the previous section, is not needed here. Otherwise, the computational algorithms are very similar. In order to establish the required slopes for the first and last elliptical arcs in a cross section, the first and last segments in each cross section must be straight lines.

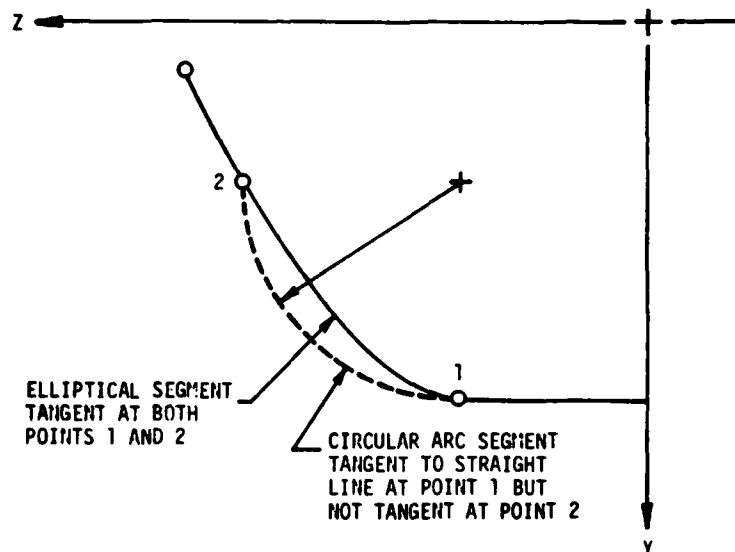


FIGURE 42 - REPLACEMENT OF CIRCULAR ARC WITH ELLIPTICAL SEGMENT

4.4 TRANSLATOR CODE

Geometry data decks set up in HABP format may be converted to the proper format for input to the geometry code by utilizing a translator code. The translator is designed to process an HABP data deck with a minimum of additional input by the user. However, two passes through the translator might be necessary to ascertain the proper control points in the resultant cross-sectional planes. For ease in checking the results, each resultant cross section has the same even number of points; some points may be repeated.

After reading user supplied titles and control variables, the first operation of the translator code reads the HABP data deck in its entirety, storing the data for each major panel. Next, panels and data beyond a specified cut-off station are eliminated. An example of a complete model is shown in Figure 43, for the X-24C flat-bottom delta wing configuration. The same configuration cut off just ahead of the fins, eliminating all protuberances but the canopy, is shown in Figure 44. When subpanels are indicated, they are treated as major panels. Values of the body stations from all the panels are then accumulated and arranged in order, eliminating duplicate values. If some panels do not contain data at all body stations within their length from start to end, such data is added by interpolating along longitudinal lines. This results in a series of panels, not necessarily ordered and possibly overlapping longitudinally, with all body stations represented appropriately. The start and end of these panels are then accumulated and sorted and used to order the panels and to indicate limits of additional panels made by dividing large panels at the additional starting stations whenever possible. The schematic model shown in Figure 45 illustrates this procedure.

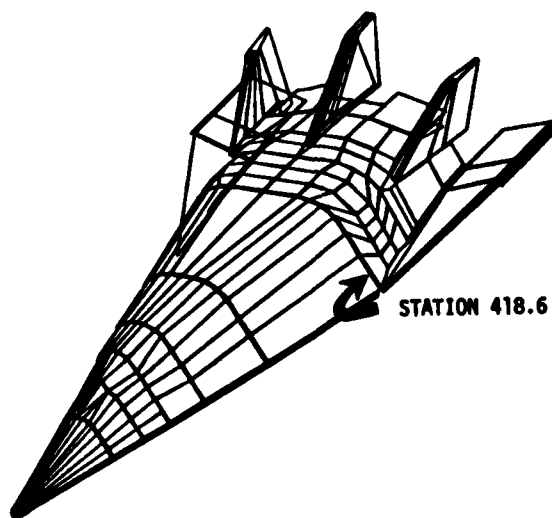


FIGURE 43 - COMPLETE MODEL FOR X-24C FROM HABP FORMAT

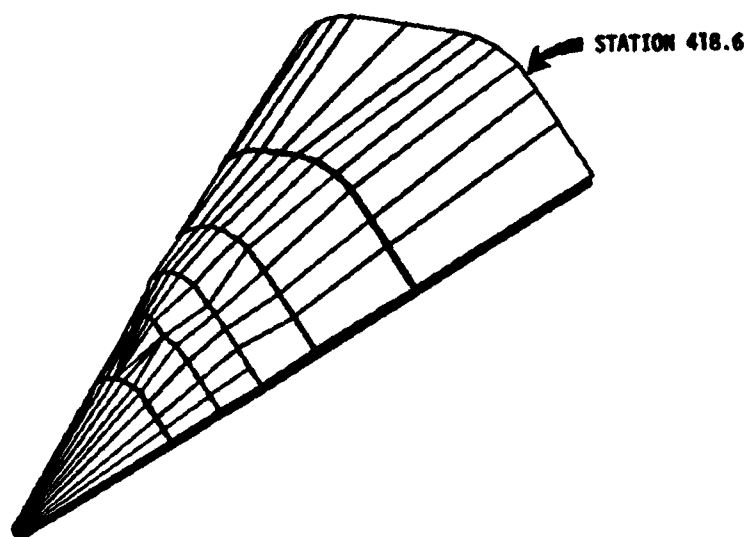


FIGURE 44 - X-24C MODEL CUT OFF FOR PHASE I

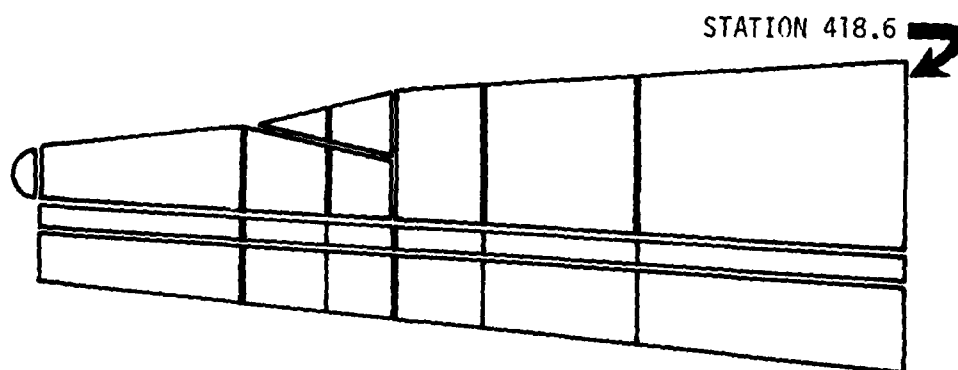


FIGURE 45 - MODEL SCHEMATIC FOR TRANSLATOR CODE

At this point in the procedure panels no longer overlap in the longitudinal direction, but each longitudinal section may contain a different number of panels arranged in the circumferential direction. The panels in any given section are not necessarily ordered at this point, but are so arranged in the next step. Common lines between circumferential panels are then eliminated from one of the pairs, resulting in circumferentially complete single panels in the longitudinal direction, each with possibly a different number of circumferential points. This difference is adjusted by adding rows of points, where necessary, making the points from two adjacent panels correspond at the common intersection. The nose cap panel participates in the above step only to the extent that circumferential rows of points on the nose cap are adjusted to correspond to the points on the next panel, rather than adjusting both panels. Then, by eliminating the duplicate cross section common to adjacent panels, the complete model merges into a single panel. See Figure 46.

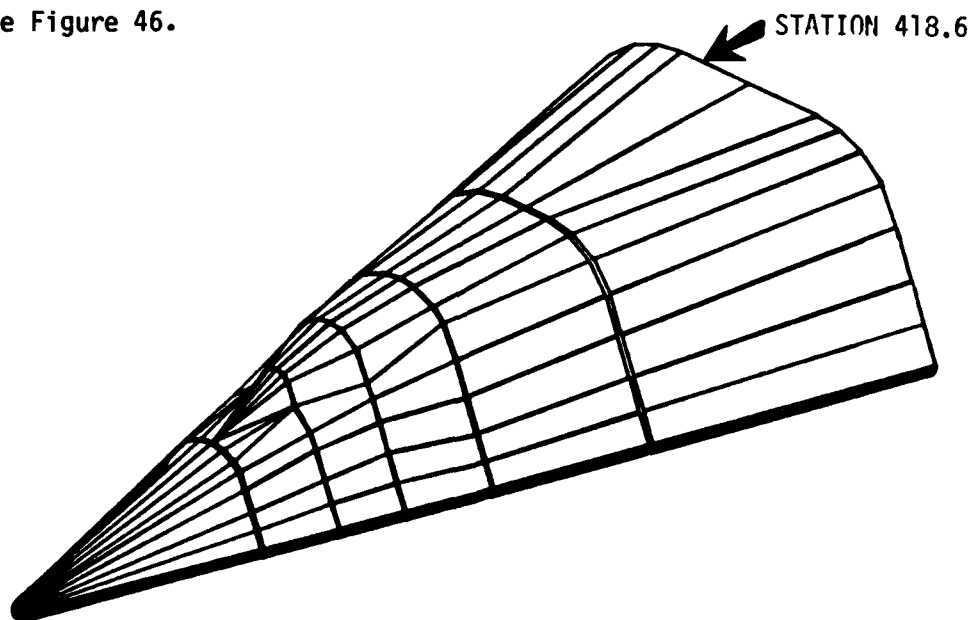


FIGURE 46 - X-24C MODEL FROM TRANSLATOR CODE

Two files are prepared from the resultant procedure. One file contains the data in a form suitable for input directly into the geometry program. The second file contains the complete single panel model back in HABP format to be used in verifying the procedure through either a visual examination of the file or a computer aided plotting routine.

SECTION V

OGIVE/CYLINDER CHECK CASE

A relatively simple body of revolution configuration was chosen as the first demonstration case; an ogive-cylinder with a hemispherical nose cap. A sketch of the model is shown in Figure 47. The ogive radius is 61.7 inches, the cylindrical radius is 4.25 inches, and the nose radius is 0.1 inch. The vehicle length of interest is 47.5 inches. The following section will discuss several aspects of this configuration; specifically, geometry input by cross-section coordinates, input pressure distribution, streamline generation at angle of attack, heating rate distribution at angle of attack, and fin/plate interference heating.

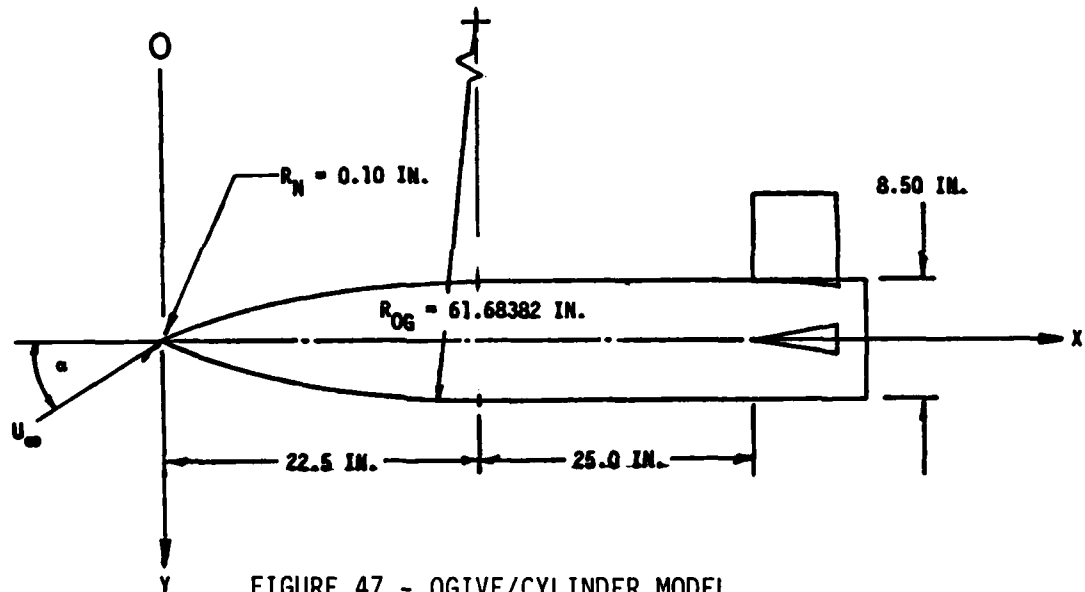


FIGURE 47 - OGIVE/CYLINDER MODEL

5.1 ARBITRARY GEOMETRY

It appears that definition of the geometry in the nose cap region affects the heating results as printed out in the program. Differences in the heating rates using geometric fits were discovered when compared with exact geometry results. The print-out value is the ratio of local heating rate to the stagnation point value and the geometric fits predict a stagnation value somewhat in error to that from the exact geometry solution. However, the heating values downstream of the stagnation point are in good agreement with the exact geometry results. To show the effect of nose cap definition on the stagnation point radius of curvature

and heating rate for the hemisphere-ogive-cylinder check case, the number of stations defining the nose cap between the true nose point and the sphere-ogive tangency point was varied. Results are presented in Figures 48 and 49 for the stagnation point radius of curvature and heating rate, respectively. For this model, at least, 7 or 8 stations are required to assure agreement with the exact geometry solution.

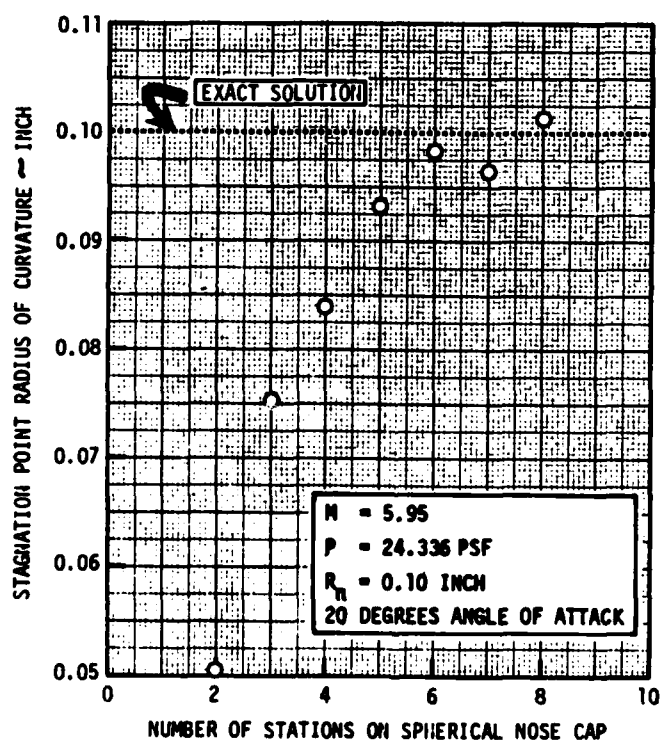


FIGURE 48 - EFFECT OF GEOMETRY FIT ON STAGNATION POINT CURVATURE

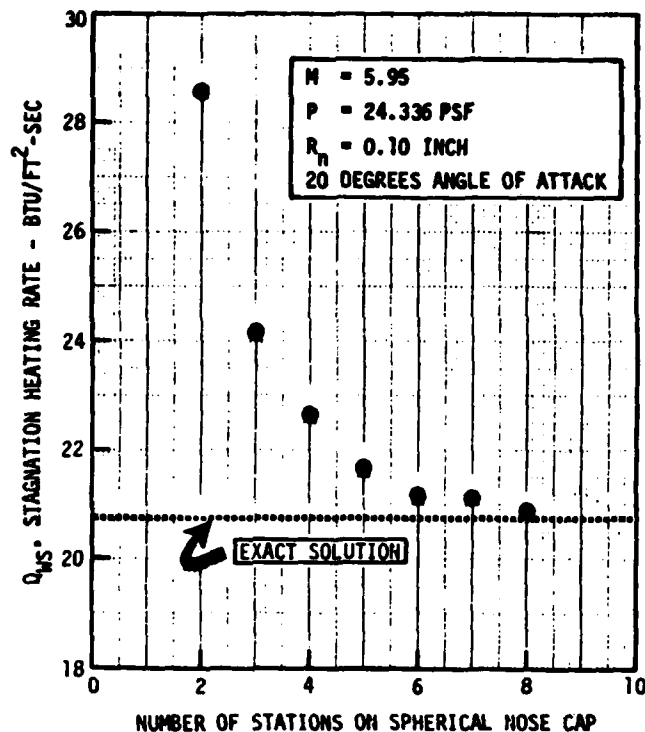


FIGURE 49 - EFFECT OF GEOMETRY FIT ON STAGNATION HEATING

5.2 INPUT CONDITIONS

Freestream input conditions for wind tunnel tests for which data are available are tabulated below.

$$\begin{aligned}
 P_{\infty} &= 24.336 \text{ psf} \\
 T_{\infty} &= 102.75^{\circ}\text{R} \\
 U_{\infty} &= 2956 \text{ fps} \\
 M_{\infty} &= 5.95
 \end{aligned}$$

Assume a wall temperature of 550°R . Transition onset at angle of attack is assumed at an X distance of 1.5 inch; fully developed turbulent flow at 1.8 inch.

5.2.1 Input Pressure Data

One of the present analysis cases was carried out by using the input pressure distribution option. Pressure data at angles of attack of 0° , 4° , 8° , and 12° were received from AFFDL. This data was generated with the NSWC inviscid flow field code (Reference 31) and closely matches test data. Nose cap pressure data at zero angle of attack is presented in Figure 50. Polar plots at two stations (on the nose cap and on the cylindrical section) for 12 degrees angle of attack are presented in Figures 51 and 52. The data at each station are normalized by the value on the windward stagnation line ($\phi = 0^\circ$) at that station.

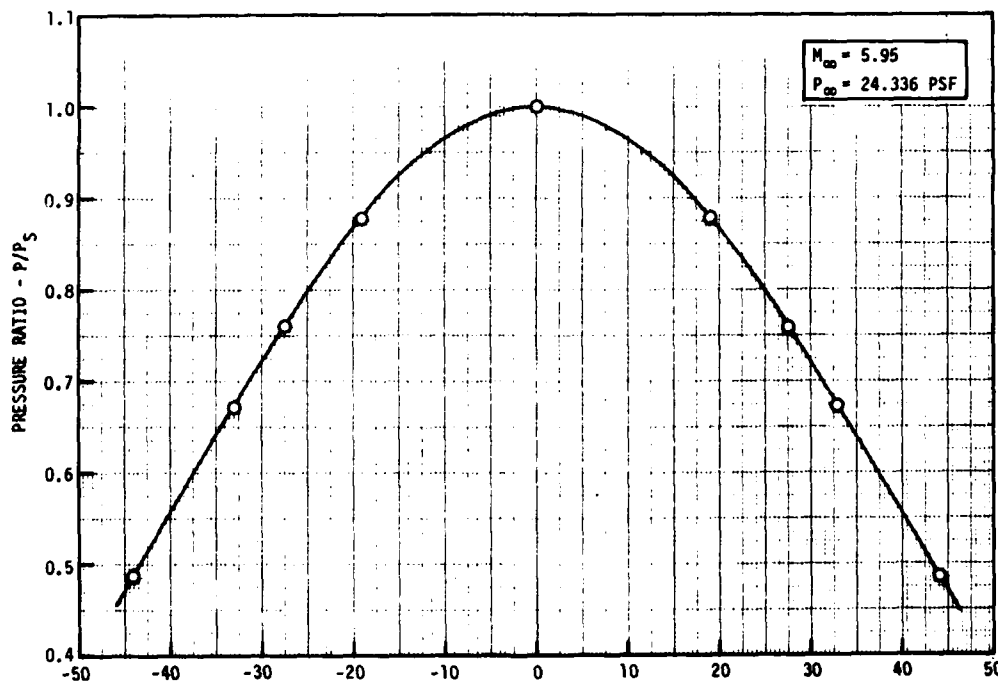


FIGURE 50 - SPHERICAL NOSE CAP PRESSURES

PRESSURE DISTRIBUTION FROM
 FIT OF DATA FROM NSWC
 PROGRAM (REFERENCE 31)
 $M_{\infty} = 5.95$
 $P_{\infty} = 24.336 \text{ PSF}$
 $\alpha = 12^\circ$
 $R_N = 0.10 \text{ IN.}$
 $P_{CL}/P_S = 0.32458$
 $P_S = 1120.2 \text{ PSF}$

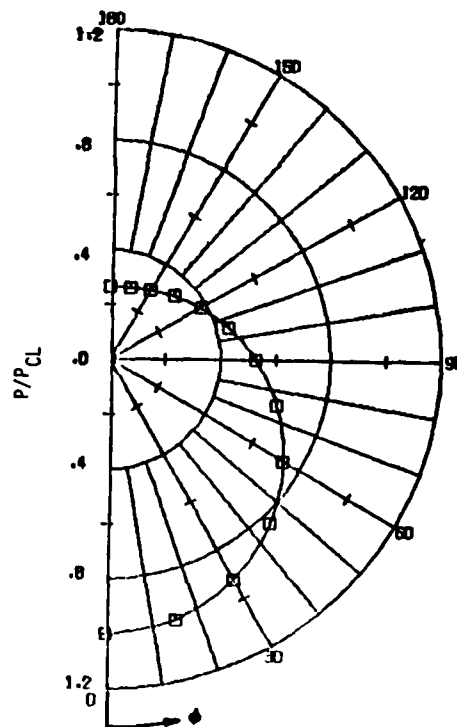


FIGURE 51 - PRESSURES ON OGIVE/CYLINDER ($x=0.0699 \text{ INCH}$)

PRESSURE DISTRIBUTION FROM
 FIT OF DATA FROM NSWC
 PROGRAM (REFERENCE 31)
 $M_{\infty} = 5.95$
 $P_{\infty} = 24.336 \text{ PSF}$
 $\alpha = 12^\circ$
 $R_N = 0.10 \text{ IN.}$
 $P_{CL}/P_S = 0.06461$
 $P_S = 1120.2 \text{ PSF}$

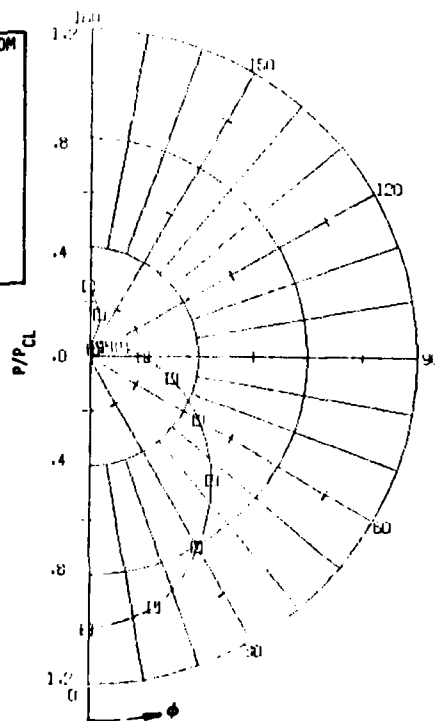


FIGURE 52 - PRESSURES ON OGIVE/CYLINDER ($x=39.6634 \text{ INCH}$)

5.2.2 Options and Other Input Data

The options chosen for this demonstration case are listed in Appendix E of Volume II on sample output, which reproduces the first pages of the computer output. Also shown are the derived initialized stagnation conditions, normal shock properties, and shock stand-off parameters.

5.3 STREAMLINE GENERATION

Streamlines were generated at two angles of attack, 8 degrees and 12 degrees, and for two different pressure options for 12 degrees angle of attack, input pressures and modified Newtonian. The 8 degrees angle-of-attack case used the modified Newtonian pressure option. The streamlines have been superimposed on a representation of the model and are shown in Figures 53 through 58, in both a side view and a front view. The front views are looking at the vehicle at zero angle of attack. Using the input pressures for 12 degrees angle of attack, it is seen that $\beta \geq 2^\circ$ streamlines wrap completely around the vehicle. The $\beta = 2^\circ$ streamline using the modified Newtonian pressure wraps around to $\phi = 90^\circ$ at the aft end. Using the modified Newtonian pressure at 8 degrees angle of attack, the $\beta = 6^\circ$ streamline wraps around to $\phi = 90^\circ$ at the aft end.

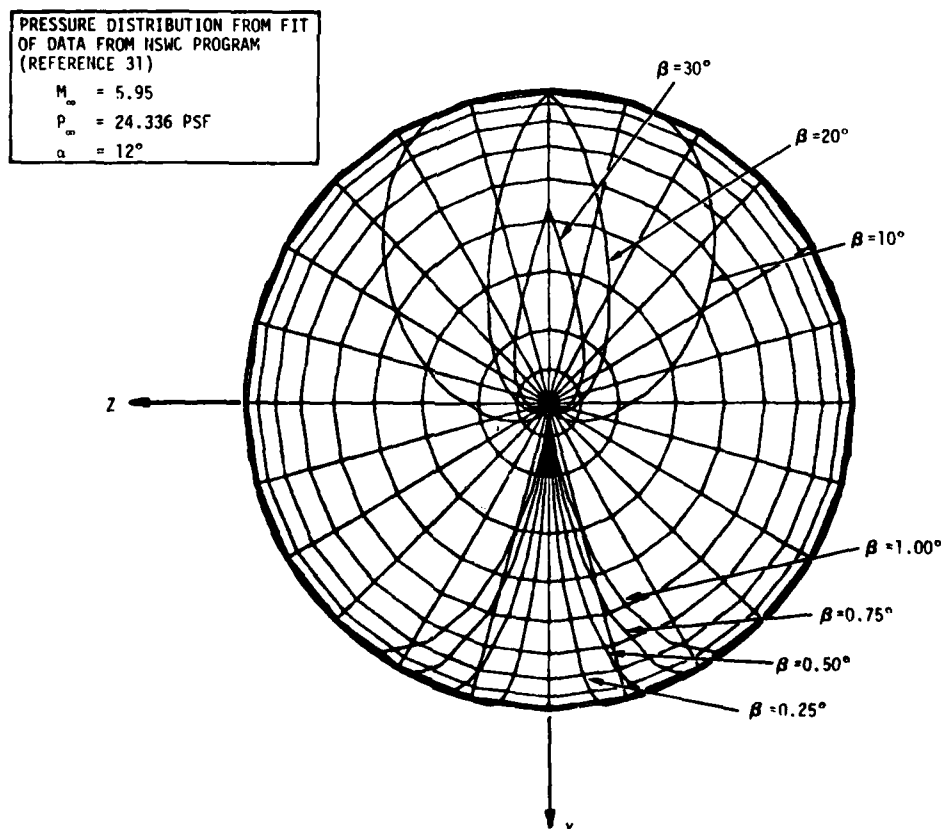


FIGURE 53 - STREAMLINES ON OGIVE/CYLINDER, 12° ANGLE OF ATTACK, INPUT PRESSURES - (FRONT VIEW)

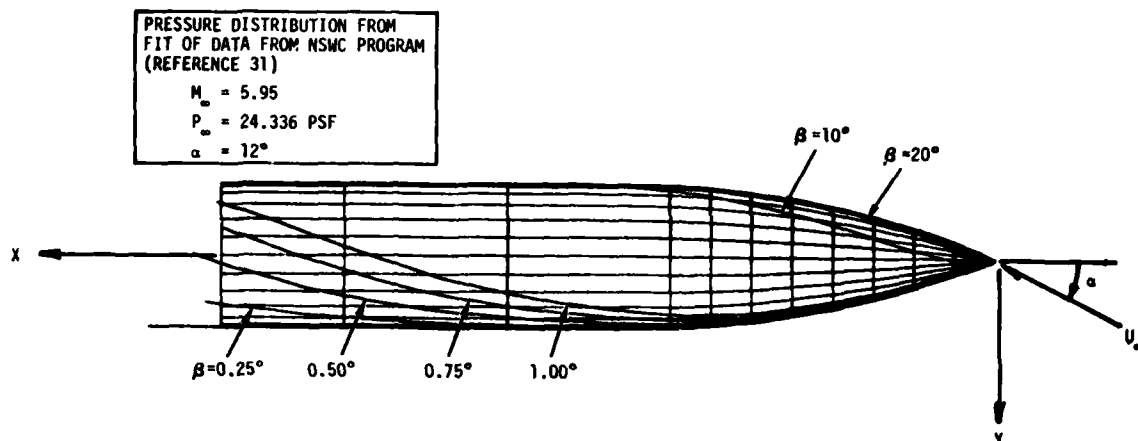


FIGURE 54 - STREAMLINES ON OGIVE/CYLINDER, 12° ANGLE OF ATTACK, INPUT PRESSURES - (SIDE VIEW)

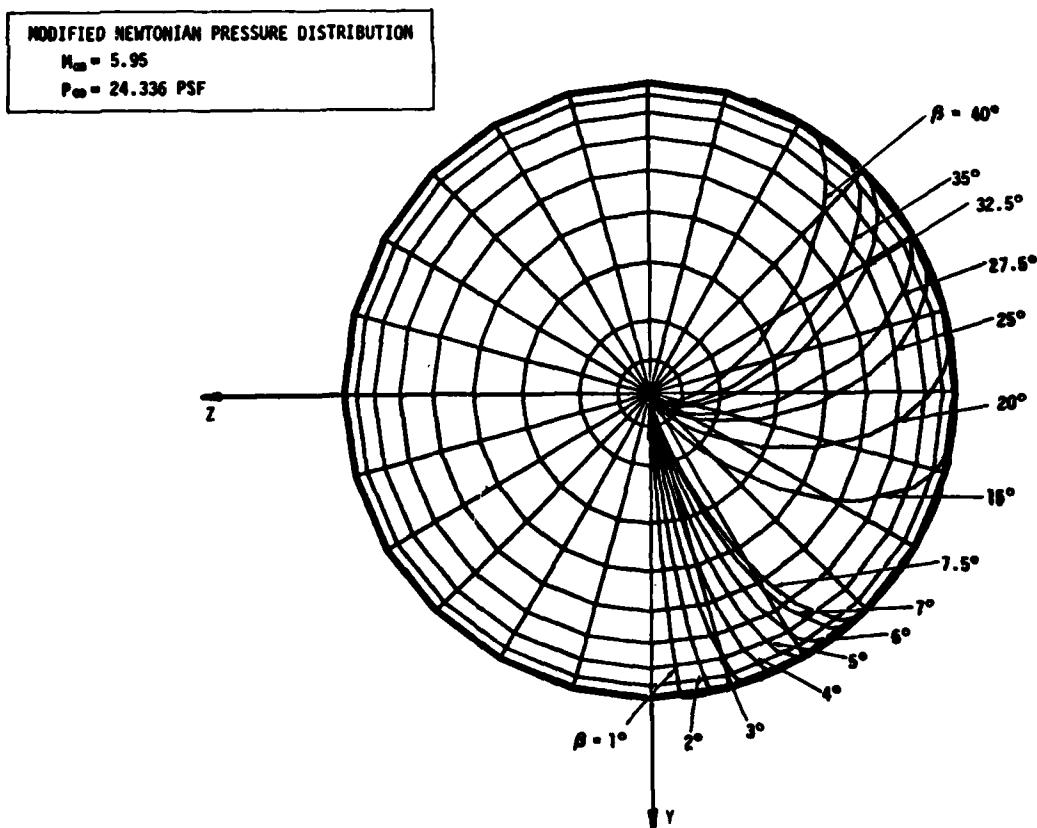


FIGURE 55 - STREAMLINES ON OGIVE/CYLINDER, 8° ANGLE OF ATTACK, NEWTONIAN PRESSURE - (FRONT VIEW)

MODIFIED NEWTONIAN PRESSURE DISTRIBUTION

$M_{\infty} = 5.95$
 $P_{\infty} = 24.336 \text{ PSF}$

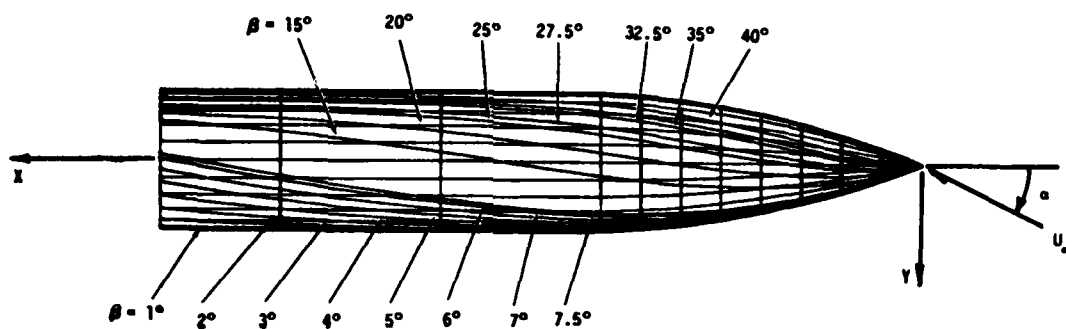


FIGURE 56 - STREAMLINES ON OGIVE/CYLINDER, 8° ANGLE OF ATTACK, NEWTONIAN PRESSURE - (SIDE VIEW)

MODIFIED NEWTONIAN PRESSURE DISTRIBUTION

$M_{\infty} = 5.95$
 $P_{\infty} = 24.336 \text{ PSF}$

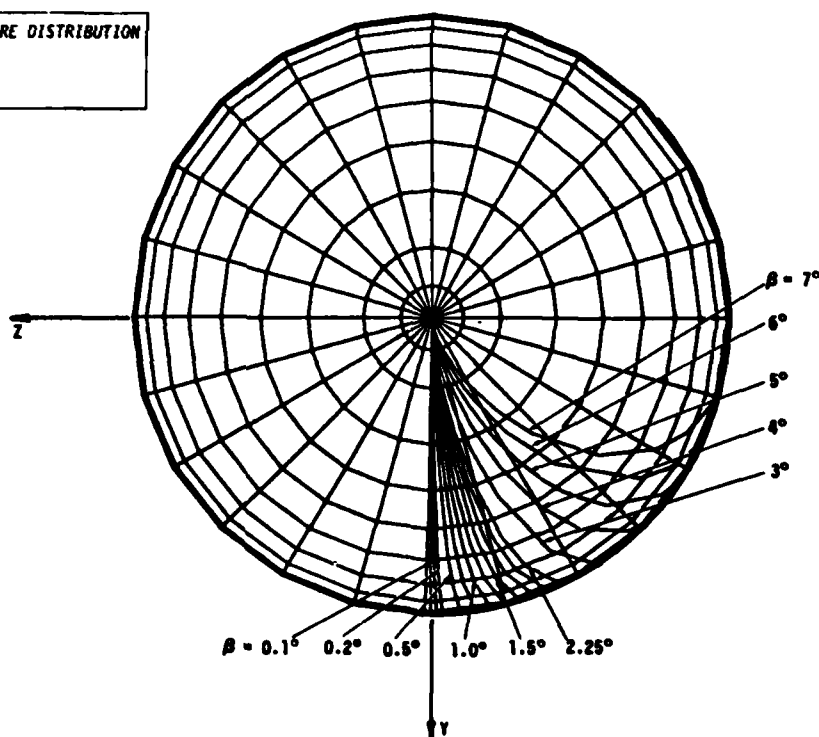


FIGURE 57 - STREAMLINES ON OGIVE/CYLINDER, 12° ANGLE OF ATTACK, NEWTONIAN PRESSURE - (FRONT VIEW)

MODIFIED NEWTONIAN PRESSURE DISTRIBUTION
 $M_\infty = 5.95$
 $P_\infty = 24.336 \text{ PSF}$

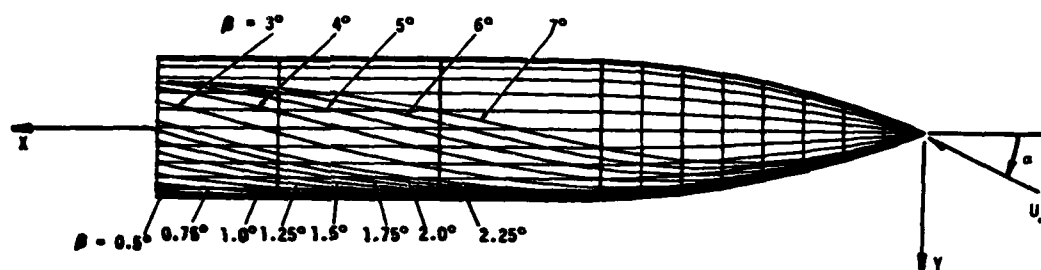


FIGURE 58 - STREAMLINES ON OGIVE/CYLINDER, 12° ANGLE OF ATTACK, NEWTONIAN PRESSURE - (SIDE VIEW)

5.4 HEATING RATE DISTRIBUTION

The axial heating rate along the windward centerline is presented in Figure 59, comparing the two angles of attack using modified Newtonian pressures. As was expected, the heating rate is higher at the greater angle of attack. Spanwise heating rate distributions are presented in Figures 60 through 65. Distribution at 3 body stations for the input pressure case are presented in Figure 60. The angle PHI is measured from the windward stagnation line. The remaining figures present a comparison of the spanwise heating distribution at two angles of attack for 5 body stations, all based on the modified Newtonian pressure distribution.

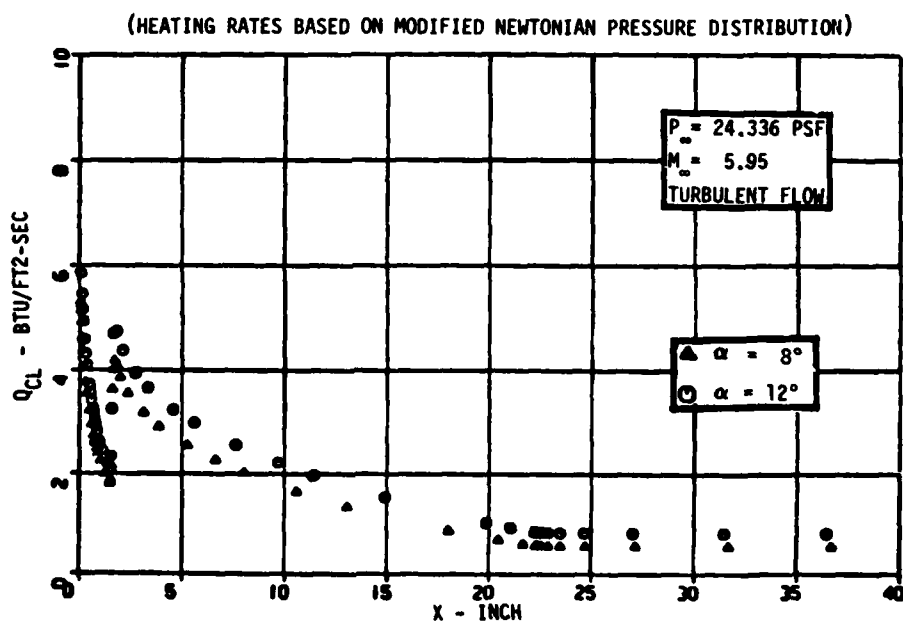


FIGURE 59 - OGIVE/CYLINDER CENTERLINE HEATING RATE

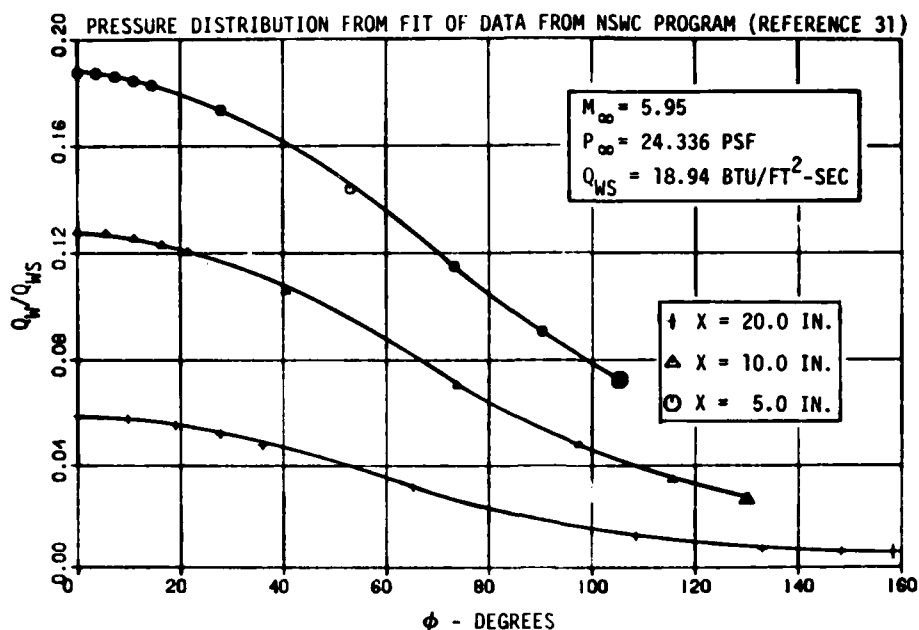


FIGURE 60 - SPANWISE HEATING RATE ON OGIVE/CYLINDER,
12° ANGLE OF ATTACK, INPUT PRESSURE

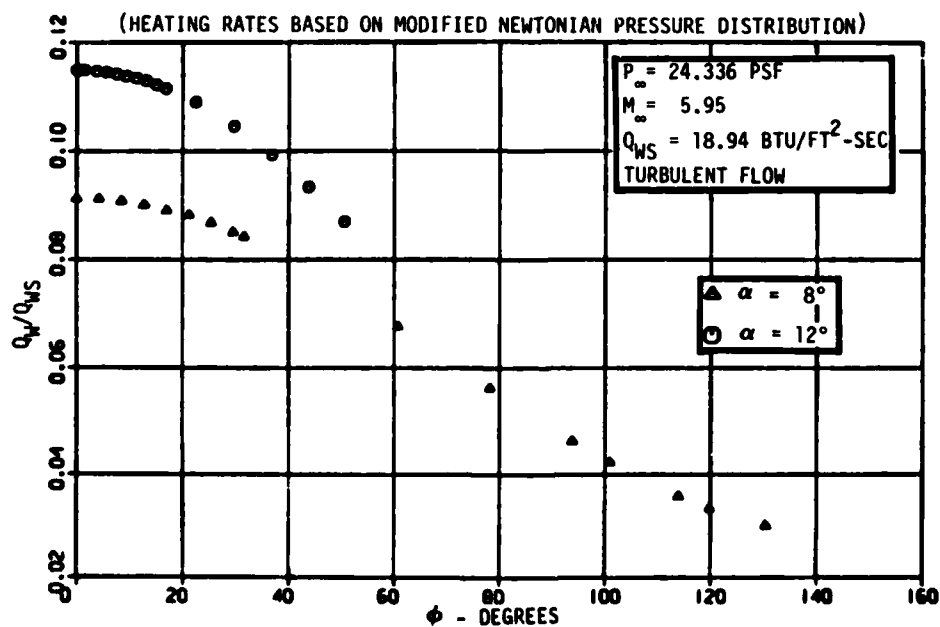


FIGURE 61 - SPANWISE HEATING RATE ON OGIVE/CYLINDER, $x = 10$ INCH

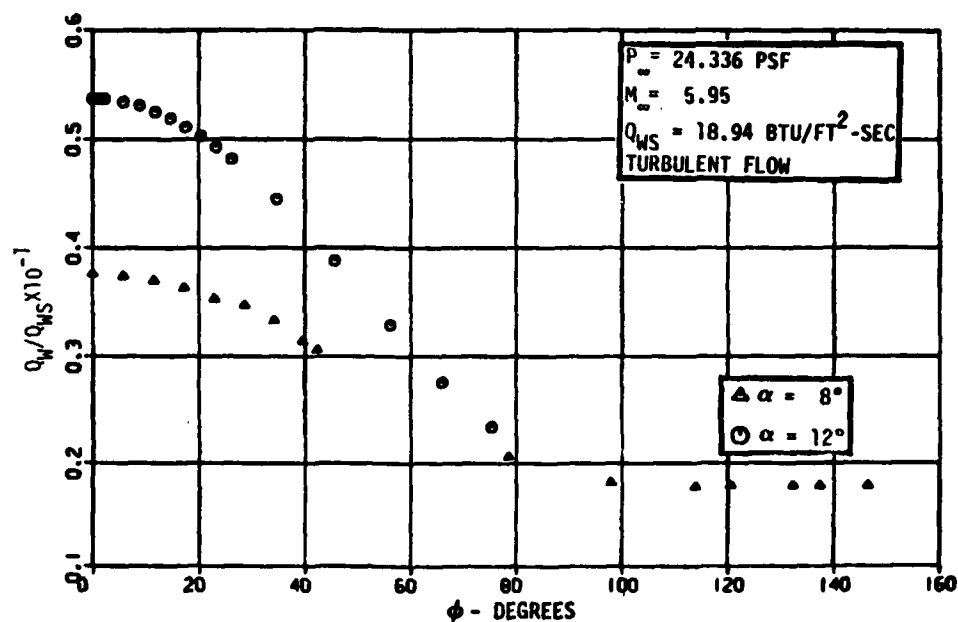


FIGURE 62 - SPANWISE HEATING RATE ON OGIVE/CYLINDER, X = 20 INCH

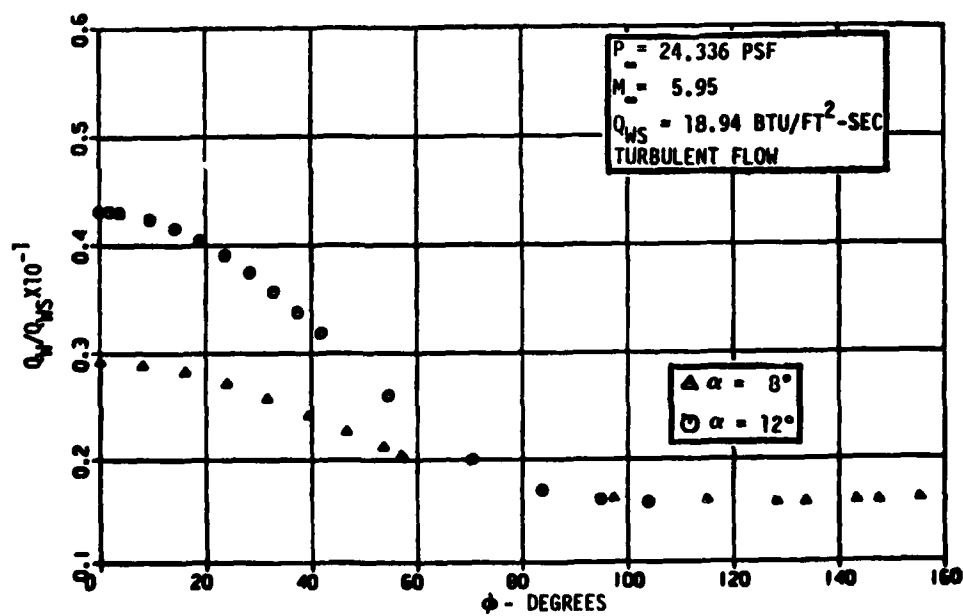


FIGURE 63 - SPANWISE HEATING RATE ON OGIVE/CYLINDER, X = 30 INCH

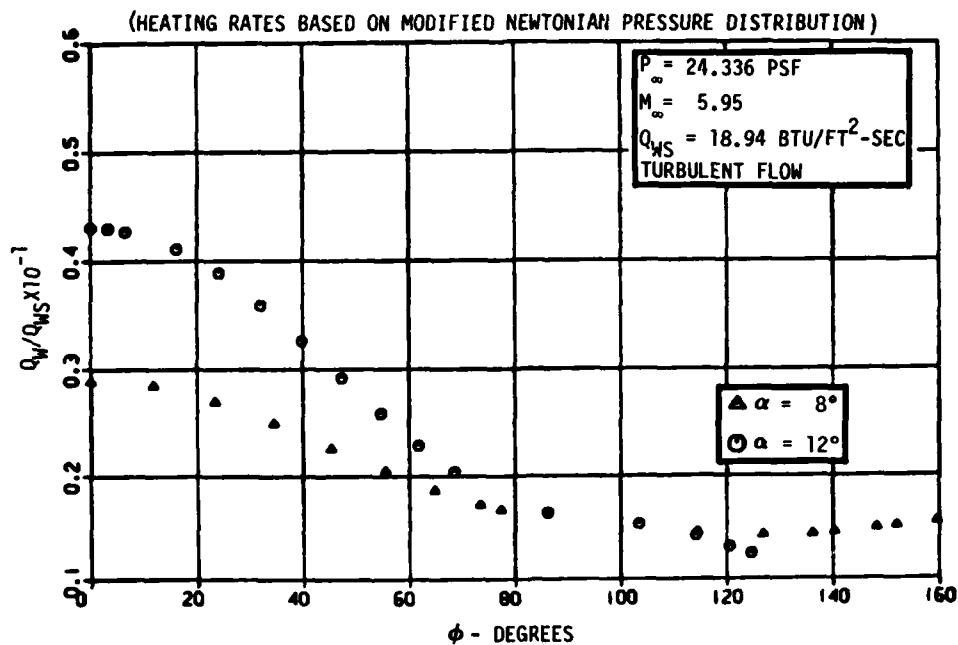


FIGURE 64 - SPANWISE HEATING RATE OF OGIVE/CYLINDER, $X = 40$ INCH

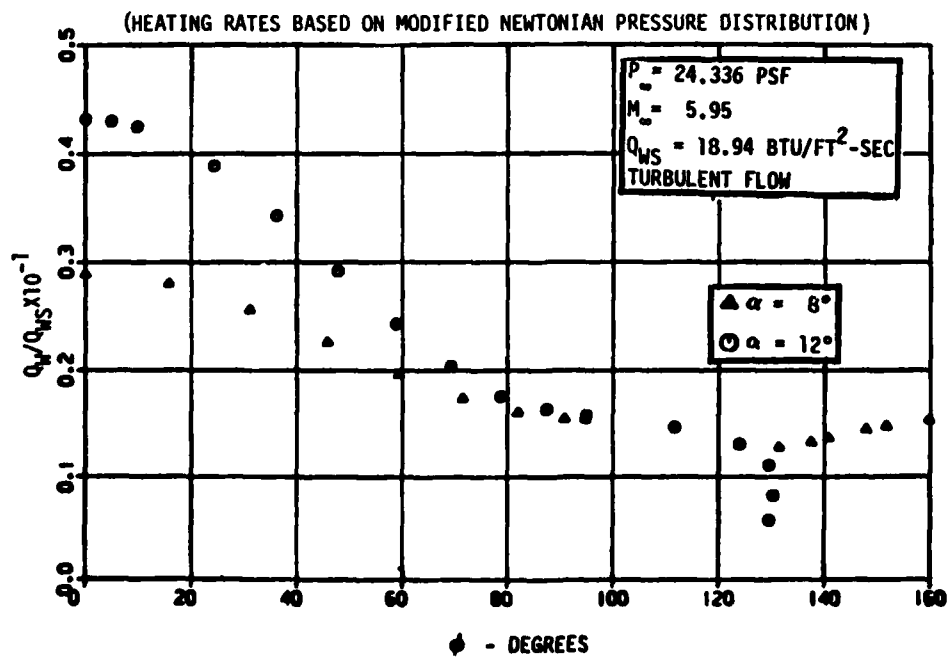


FIGURE 65 - SPANWISE HEATING RATE ON OGIVE/CYLINDER, $X = 47.5$ INCH

5.5 FIN/PLATE INTERACTION

Calculations were performed to obtain the heating rate distribution resulting from fin/plate interaction. A fin was placed at the aft end of the vehicle with the leading edge on the 90° meridian, measured from the windward stagnation line. The fin was arbitrarily made 10 inches long with the side of the fin oriented 10° from the longitudinal axis. As was mentioned above, the $\beta = 6^\circ$ streamline at 8 degrees angle of attack approaches the 90° meridian at the end of the vehicle, while the $\beta = 2^\circ$ streamline intersects the 90° meridian for 12 degrees angle of attack. Information on these two streamlines at the end of the vehicle provide the free stream conditions input to the fin calculations. The following table summarizes the input parameters.

α	β	$\phi_{x=47.5}(\text{IN})$	θ_{FIN}	M_e	Q_w/Q_{ws}	FIN SHOCK WAVE ANGLE
8°	6°	91.4°	20.3°	5.19	0.0155	29.8°
12°	2°	90.4°	25.4°	4.98	0.0161	36.3°

Fin/plate interaction results are presented in Figures 66 through 70. The ratio of local surface heating rate to the undisturbed value at the fin leading edge is shown for both angles of attack at each of several locations along the fin. The peak appears to be more sharply defined for the 8 degree angle of attack case, but the peak value for the 12 degree angle of attack case is 20 to 25 percent greater than for 8 degrees angle of attack.

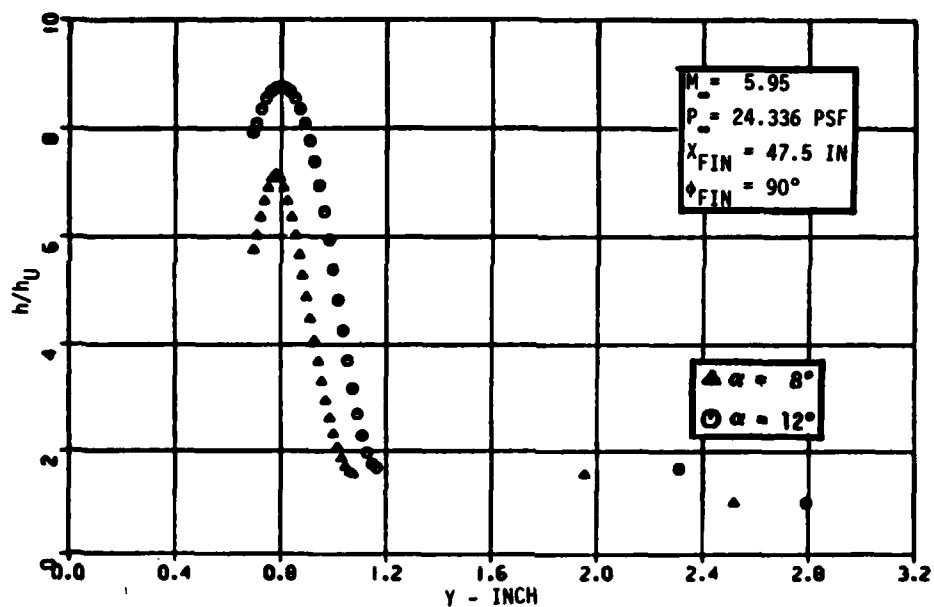


FIGURE 66 - FIN/PLATE INTERACTION HEATING, $X/X_{\text{Fin}} = 0.2$

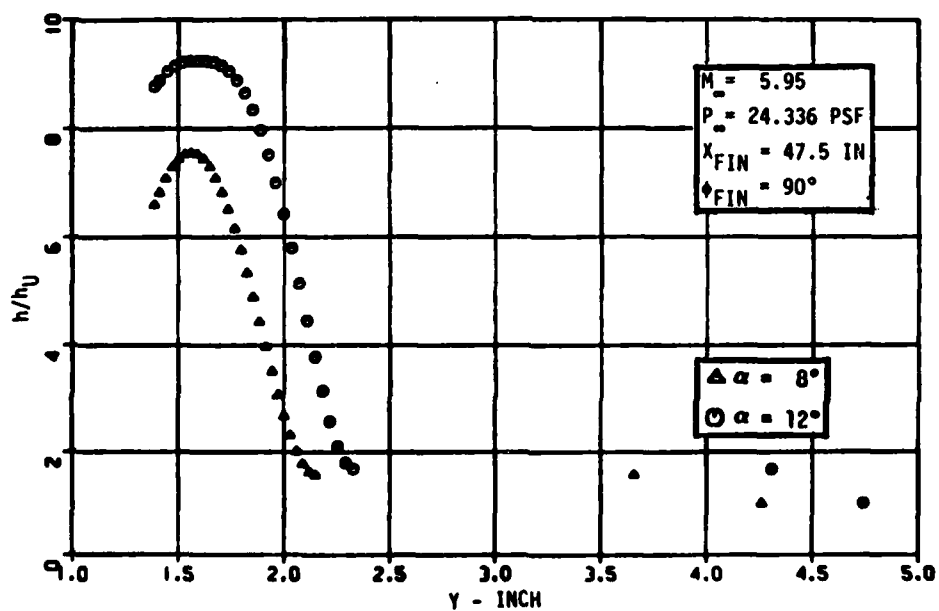


FIGURE 67 - FIN/PLATE INTERACTION HEATING, $X/X_{\text{Fin}} = 0.4$

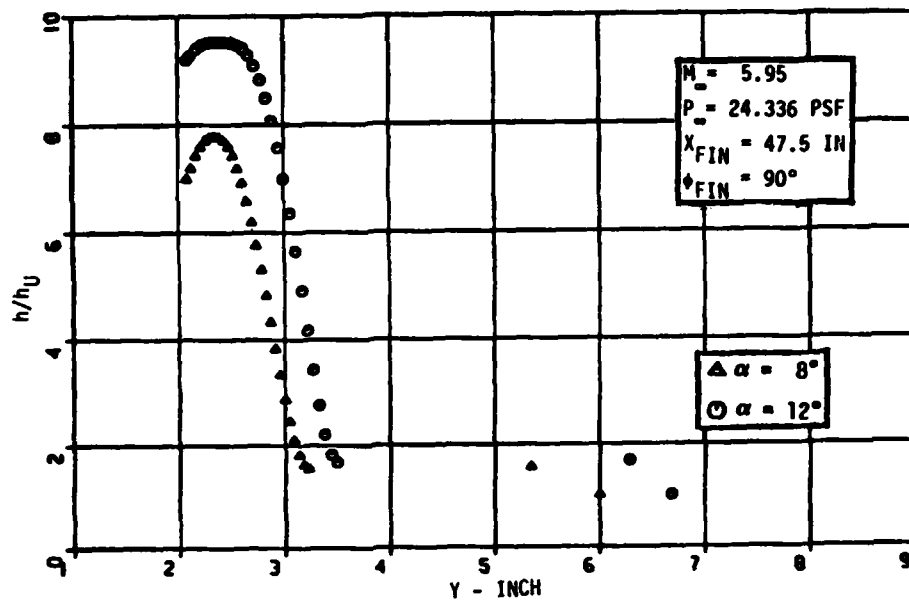


FIGURE 68 - FIN/PLATE INTERACTION HEATING, $X/X_{\text{fin}} = 0.6$

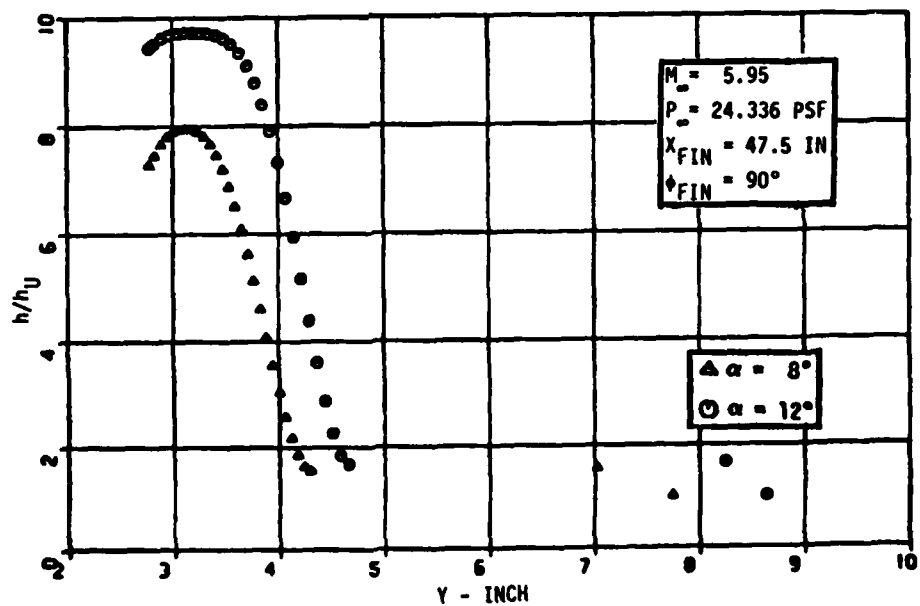


FIGURE 69 - FIN/PLATE INTERACTION HEATING, $X/X_{\text{fin}} = 0.8$

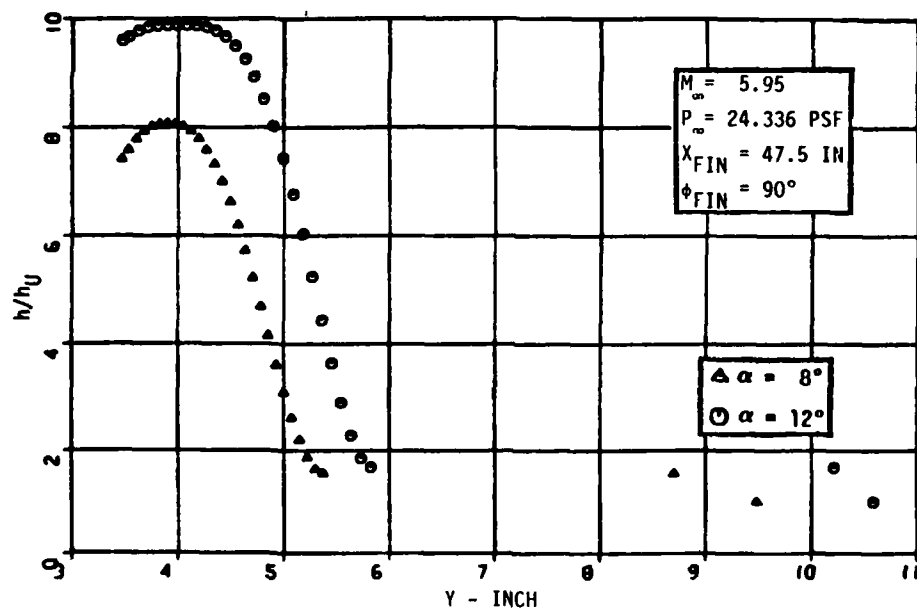


FIGURE 70 - FIN/PLATE INTERACTION HEATING, $X/X_{\text{Fin}} = 1.0$

SECTION VI

FLAT BOTTOM DELTA WING CHECK CASE

The second demonstration check case is the flat bottom, delta wing X-24C configuration. Of specific interest are the leading edge and the flat bottom portion of the vehicle. A sketch of the model was presented in Section 4.0 and is repeated here as Figure 71. The nose cap diameter and the leading edge diameter are both 8.0 inches. The sweep angle is 77.55 degrees and the leading edge starts at station 2.73. The flat bottom is inclined 3.27 degrees to the free stream at zero angle of attack. The vehicle length of interest is 418.6 inches. Geometry input by cross section coordinates, input conditions, streamline generation at angle of attack, and heat transfer results will be discussed in the following sections.

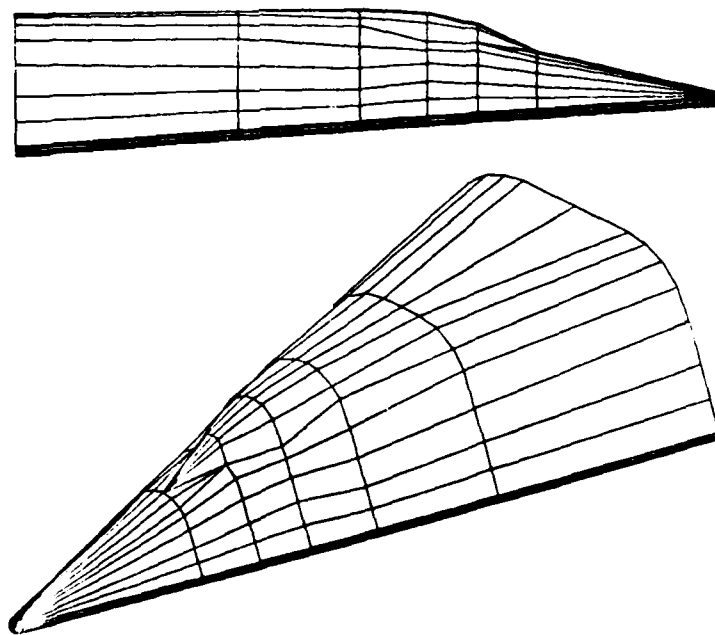


FIGURE 71 - X-24C MODEL FOR DELTA WING CHECK CASE

6.1 ARBITRARY GEOMETRY

Results of specifying the geometry from cross section coordinate data, originally in HARP format, are shown in Figure 72. The model was generated from the geometric coefficients determined in the auxiliary geometry codes.

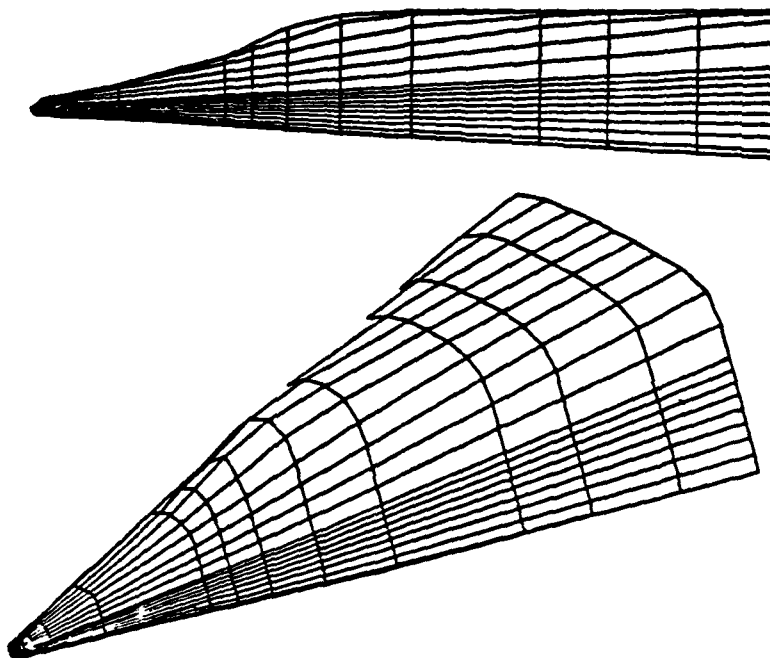


FIGURE 72 - X-24C MODEL FROM GEOMETRY COEFFICIENTS

6.2 INPUT CONDITIONS

Freestream input conditions for wind tunnel tests for which data are available are listed below.

$$P_{\infty} = 22.71 \text{ psf}$$

$$T_{\infty} = 104.0^{\circ}\text{R}$$

$$U_{\infty} = 2993 \text{ fps}$$

$$M_{\infty} = 5.99$$

The wall temperature is assumed to be 535°R . At angle of attack, transition onset is assumed to be at 1.0 inch; fully developed turbulent flow at 1.2 inch. The boundary layer edge conditions were generated assuming a variable entropy inviscid flow field for a perfect gas, although some cases were generated using a normal shock entropy.

AD-A081 471

MCDONNELL DOUGLAS ASTRONAUTICS CO ST LOUIS MO

F/6 20/4

NUMERICAL FLOW FIELD PROGRAM FOR AERODYNAMIC HEATING ANALYSIS. --ETC(U)

DEC 79 H J FIVEL

F33615-77-C-3003

UNCLASSIFIED

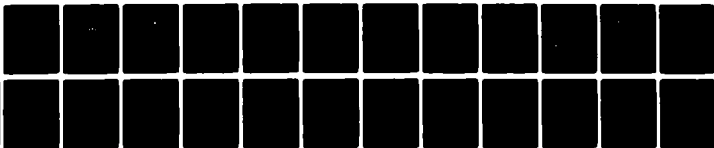
AFFDL-TR-79-3128-VOL-1

NL

2 + 2

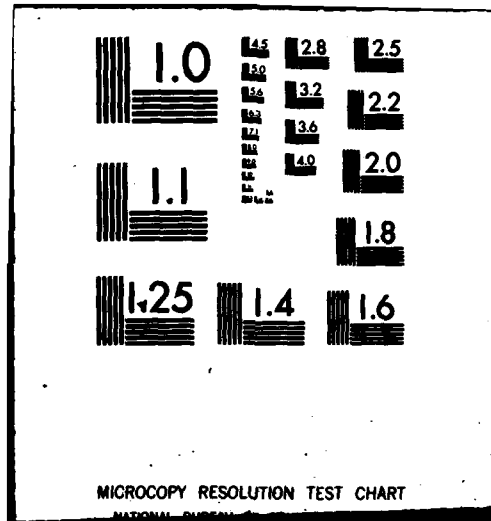
2 + 2

■



END

DATE
FILMED:
4-80



6.3 STREAMLINE GENERATION

Streamlines were generated for two angles of attack; 4 degrees and 12 degrees. The input parameters describing the flat bottom pressure distribution are listed in the table below.

α	Q_M	X_C	$(P_{CL} - P_F)/(P_{CL} - P_{SHOULDER})$
4°	0.876	5.0	0.01
12°	1.000	0.0	0.01

Typical streamlines are shown for both cases in Figures 73 through 76, superimposed on a representation of the model. Figures 73 and 75 show the streamlines as viewed from the bottom and Figures 74 and 76 are front views, looking at the vehicle at zero angle of attack. At an angle of attack of 4 degrees, the $\beta = 32.8^\circ$ streamline wraps around the leading edge. The $\beta = 10^\circ$ streamline at an angle of attack of 12 degrees wraps around the leading edge.

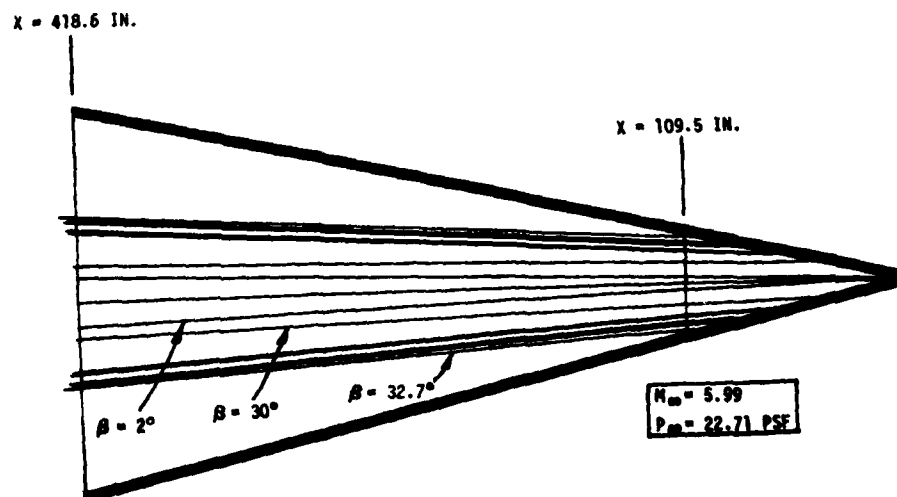


FIGURE 73 - STREAMLINES ON X-24C, 4° ANGLE OF ATTACK - (BOTTOM VIEW)

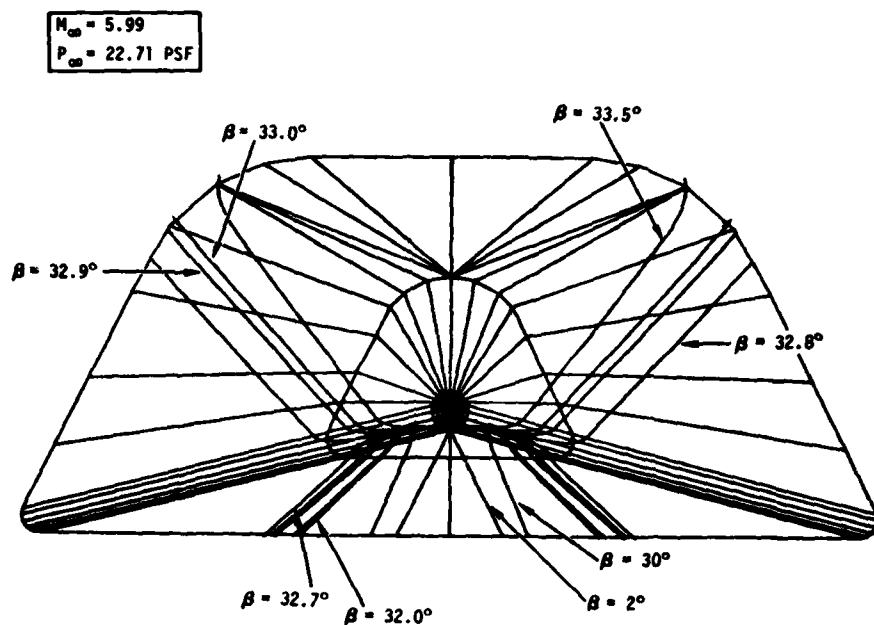


FIGURE 74 - STREAMLINES ON X-24C, 4° ANGLE OF ATTACK - (FRONT VIEW)

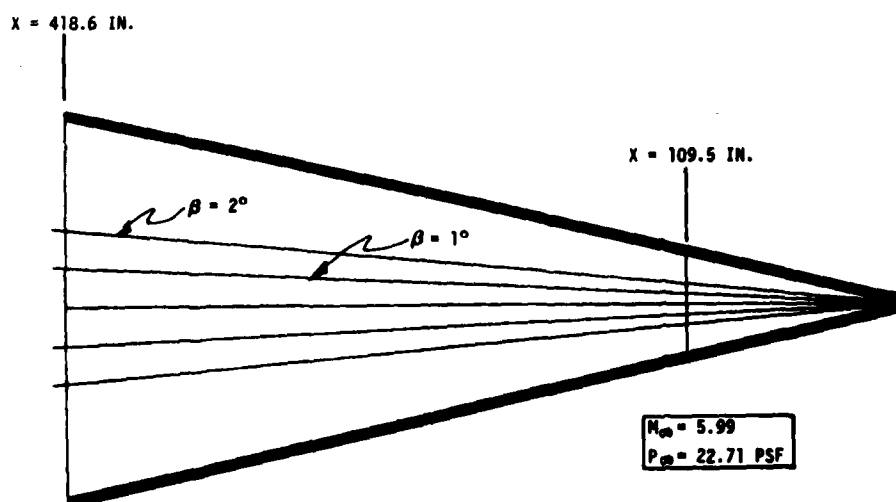


FIGURE 75 - STREAMLINES ON X-24C, 12° ANGLE OF ATTACK - (BOTTOM VIEW)

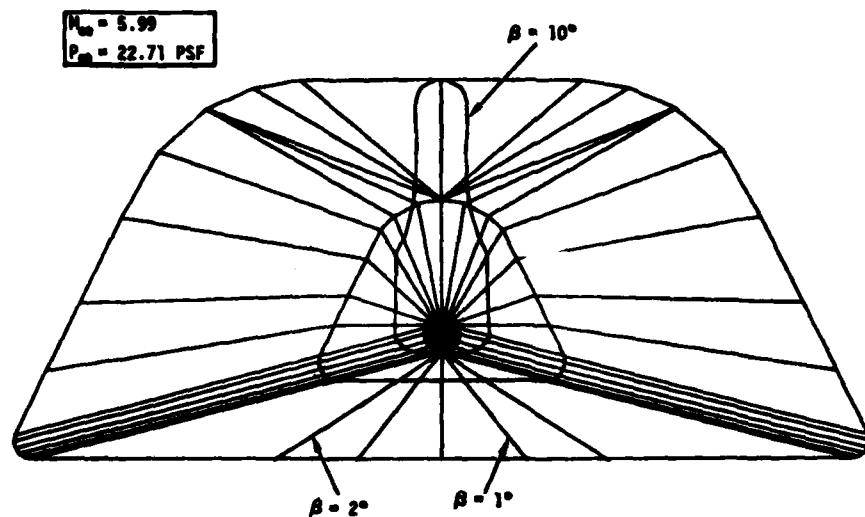


FIGURE 76 - STREAMLINES ON X-24C, 12° ANGLE OF ATTACK - (FRONT VIEW)

6.4 HEATING RATE DISTRIBUTION

The use of variable entropy in determining boundary layer edge conditions is compared to the use of normal shock entropy in Figures 77 and 78. The axial heating rate along the windward centerline at an angle of attack of 4 degrees is presented in Figure 77. The heating rate along the $\beta = 2^\circ$ streamline for the same angle of attack is presented in Figure 78. It may be seen from both figures that variable entropy predicts a higher heating rate than does normal shock entropy. The axial heating rate for the two angles of attack are compared in Figures 79 and 80. Figure 79 compares the heating rates along the windward centerline and Figure 80 compares the heating rates along the $\beta = 2^\circ$ streamline. The results shown in Figures 79 and 80 are for variable entropy. Spanwise heating rate distributions on the flat bottom at three body stations for the two angles of attack are shown in Figures 81 and 82. Body stations chosen are $X=200$ inches, $X=300$ inches, and $X=419$ inches. The same information is also presented in Figures 83 through 85. Here, the two angles of attack are compared at each of the body stations.

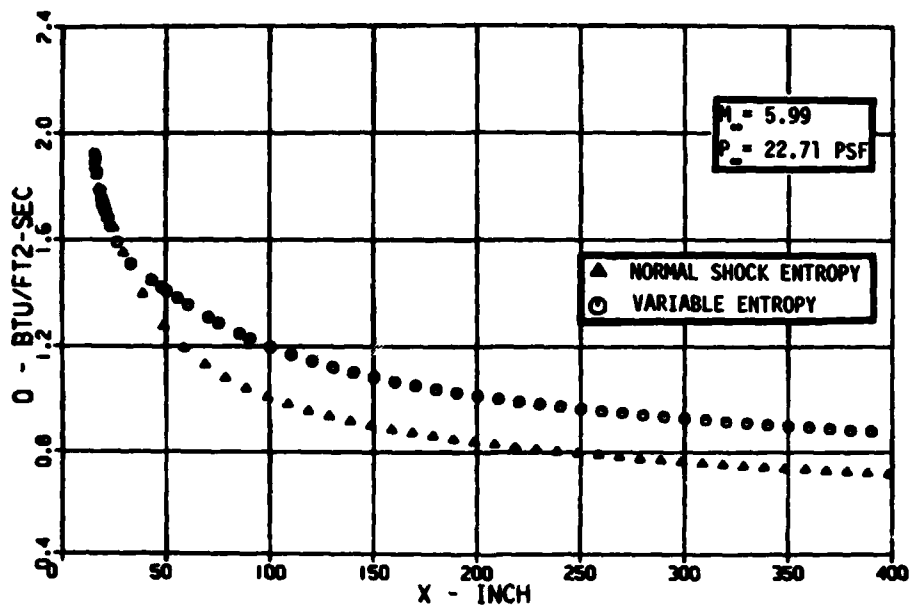


FIGURE 77 - X-24C AXIAL HEATING RATE DISTRIBUTION, 4°
ANGLE OF ATTACK, $\beta = 0^\circ$

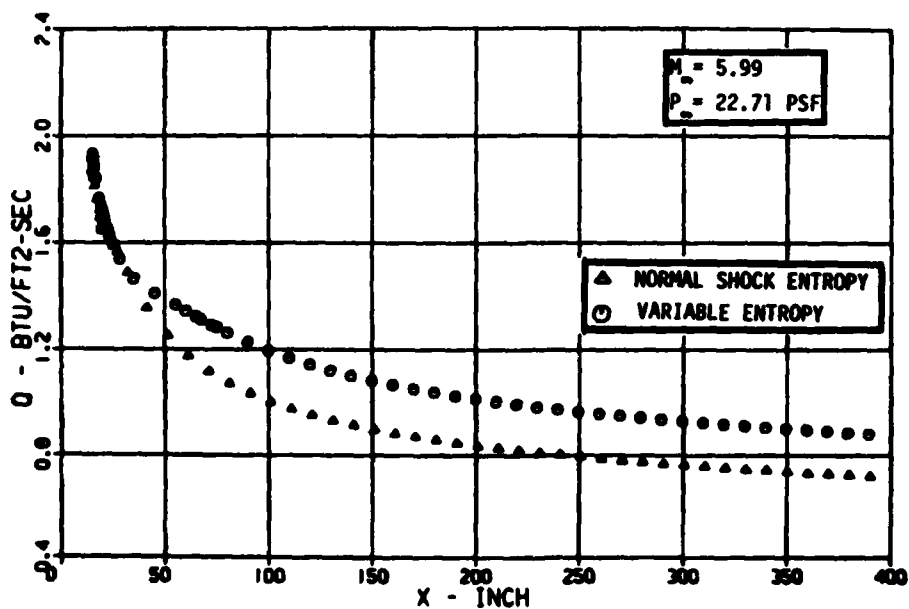


FIGURE 78 - X-24C AXIAL HEATING RATE DISTRIBUTION, 4°
ANGLE OF ATTACK, $\beta = 2^\circ$

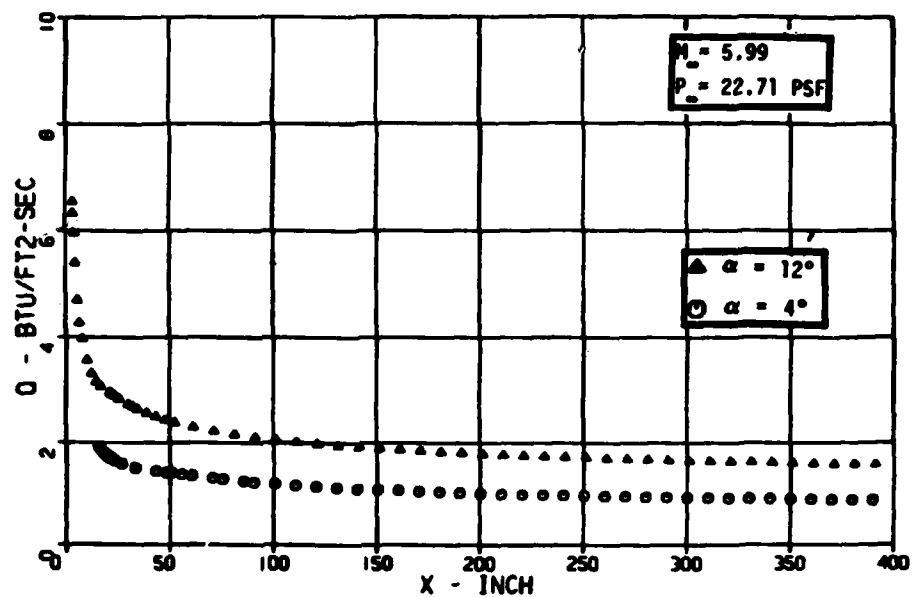


FIGURE 79 - X-24C AXIAL HEATING RATE DISTRIBUTION,
VARIABLE ENTROPY, $\beta = 0^\circ$

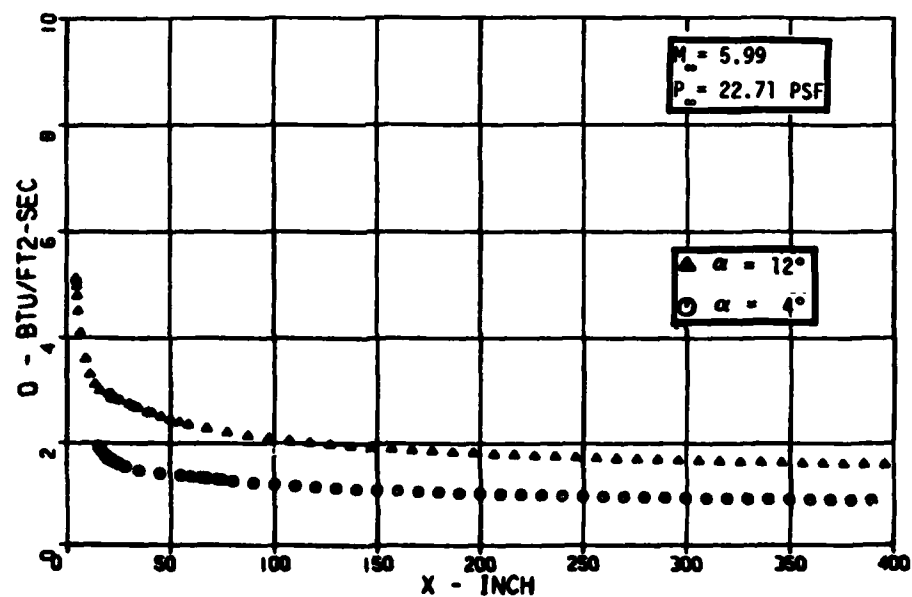


FIGURE 80 - X-24C AXIAL HEATING RATE DISTRIBUTION,
VARIABLE ENTROPY, $\beta = 2^\circ$

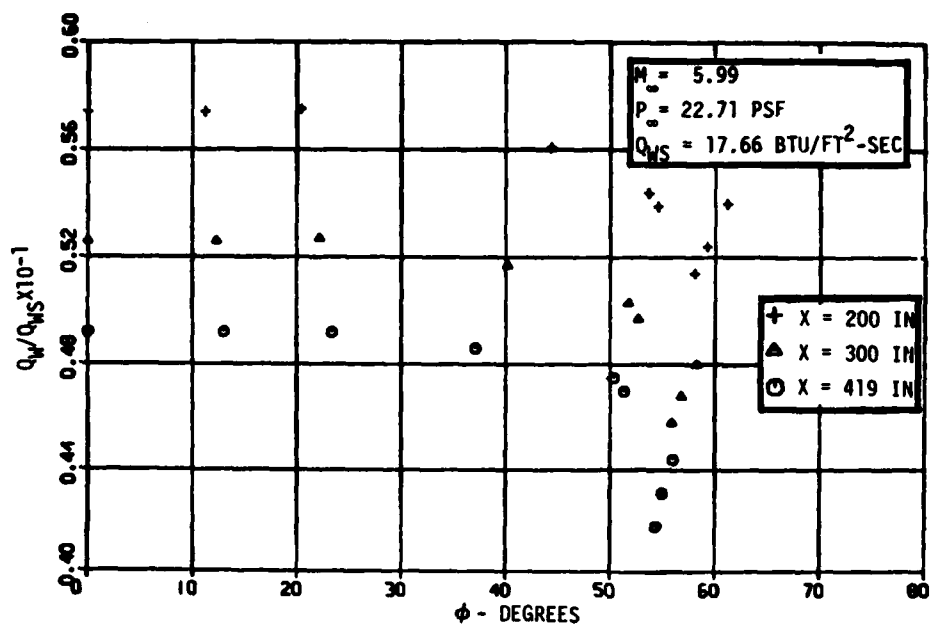


FIGURE 81 - X-24C SPANWISE HEATING RATE, 4° ANGLE OF ATTACK

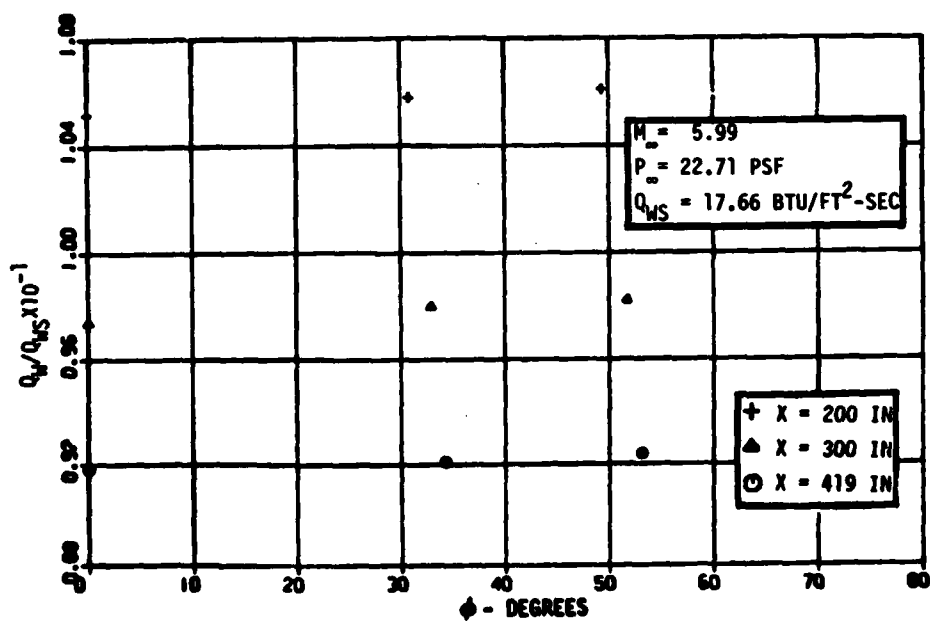


FIGURE 82 - X-24C SPANWISE HEATING RATE, 12° ANGLE OF ATTACK

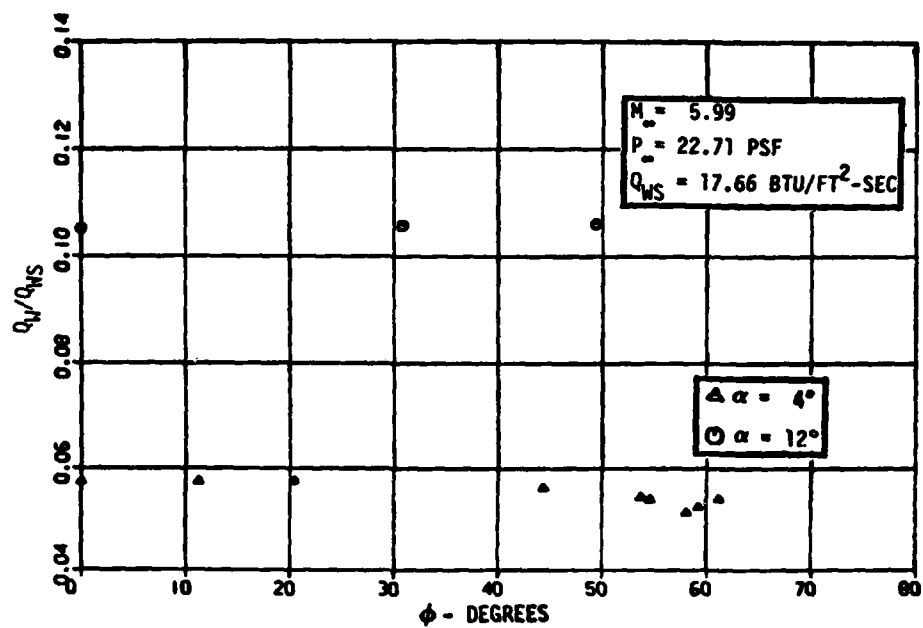


FIGURE 83 - X-24C SPANWISE HEATING RATE, $X = 200$ INCH

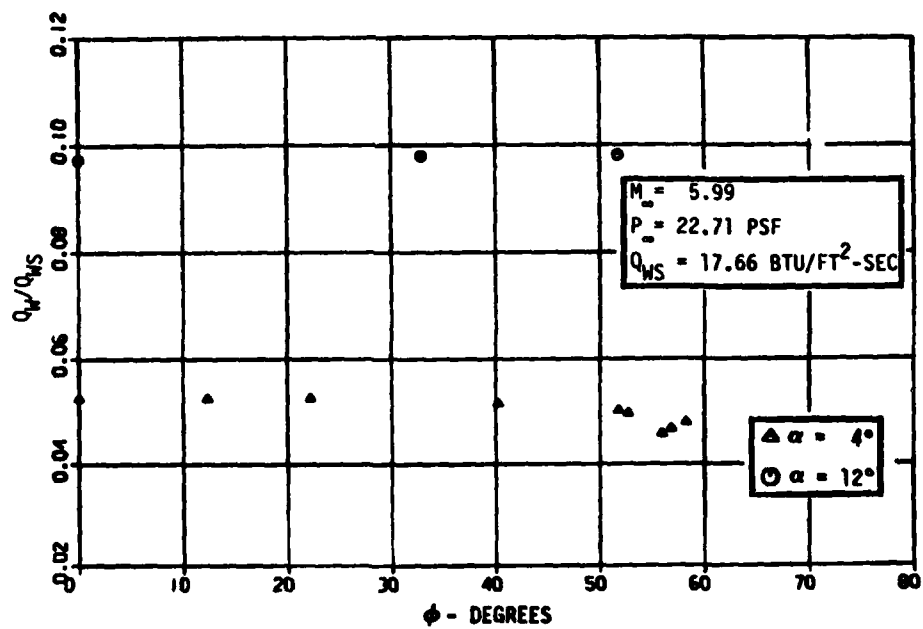


FIGURE 84 - X-24C SPANWISE HEATING RATE, $X = 300$ INCH

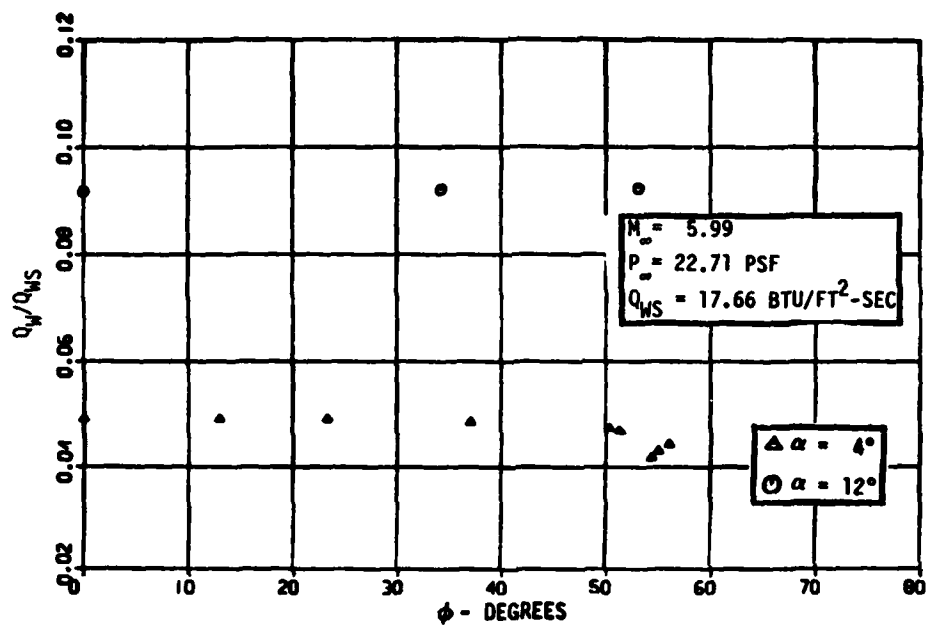


FIGURE 85 - X-24C SPANWISE HEATING RATE, $X = 419$ INCH

SECTION VII

SLAB DELTA CHECK CASE

The third demonstration check case is the slab delta model used by Bertram and Everhart in Reference 18. The slab thickness is 0.75 inches and the leading edge sweep is 70 degrees. The vehicle length of interest is 4.53 inches. The geometry in the calculations was generated with the exact analytical slab delta routine. Input conditions, stream line generation at angle of attack, and heat transfer results will be discussed in the following section. Heat transfer results include heating to a flap located at the end of the vehicle.

7.1 INPUT CONDITIONS

Freestream input parameters for two conditions are listed below

M_∞	6.8	9.6
P_∞ - psf	18.42	2.94
T_∞ - °R	108.31	85.43
U_∞ - fps	3468	4348
Re_∞	2.4×10^5	7.9×10^4

The wall temperature is assumed to be 570°R. At angle of attack, transition onset is assumed to be 0.01 inch; fully developed turbulent flow at 0.012 inch. The boundary layer edge conditions were generated with a variable entropy inviscid flow field for a perfect gas.

7.2 STREAMLINE GENERATION

Streamlines for $M_\infty = 6.8$ were generated for two angles of attack; 5.5 degrees and 10 degrees, and streamlines for $M_\infty = 9.6$ were generated at 5.2 degrees angle of attack. The input parameters describing the flat bottom pressure distribution are listed in the table below.

M_∞	α	Q_M	X_C	$(P_{CL} - P_F)/(P_{CL} - P_{SHOULDER})$
6.8	5.5°	0.798	5.35	0.01
	10.0°	1.000	0.0	0.01
9.6	5.2	0.892	4.2	0.01

Typical streamlines on the bottom delta surface are shown in Figures 86, 87, and 88. At $M_\infty = 6.8$ and an angle of attack of 5.5 degrees, the $\beta \geq 70^\circ$ streamlines wrap around the leading edge. At an angle of attack of 10 degrees and $M_\infty = 6.8$, the $\beta = 50^\circ$ streamline is still on the bottom surface. The $\beta = 20^\circ$ streamline is still on the bottom surface for the $M_\infty = 9.6$ and 5.2° angle of attack condition.

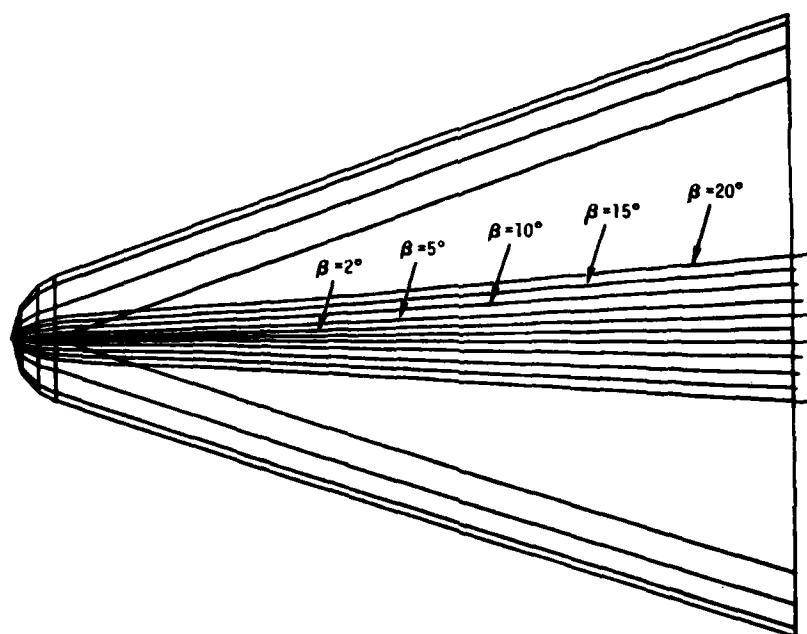


FIGURE 86 - STREAMLINES ON SLAB DELTA, 5.5° ANGLE OF ATTACK, $M = 6.8$

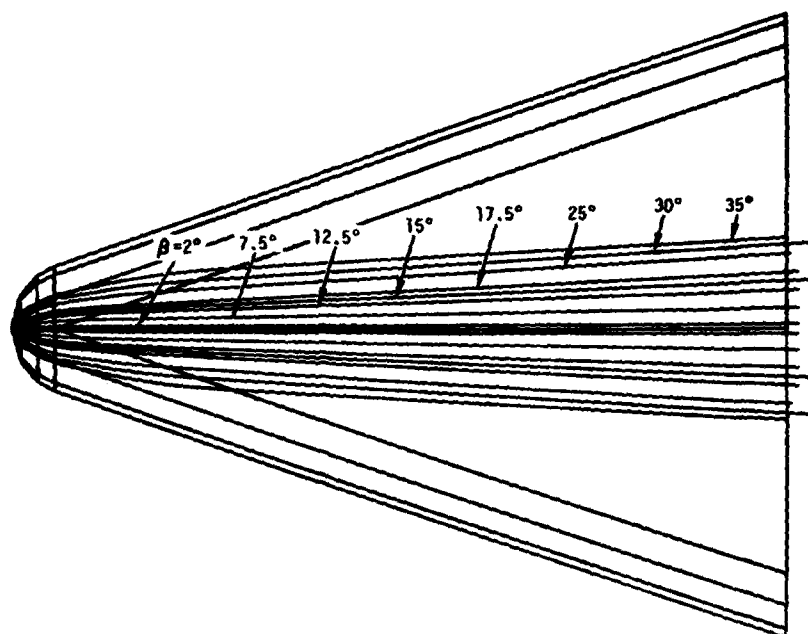


FIGURE 87 - STREAMLINES ON SLAB DELTA, 10° ANGLE OF ATTACK, $M = 6.8$

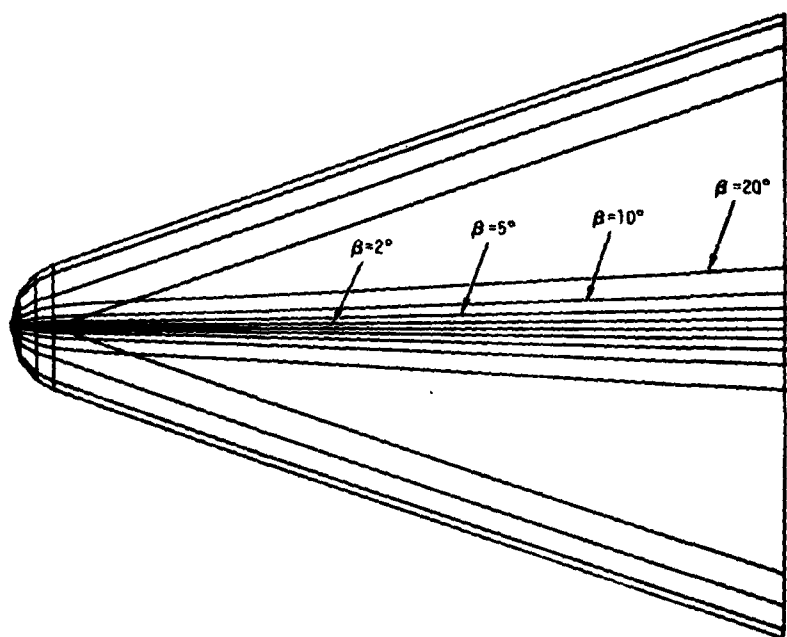


FIGURE 88 - STREAMLINES ON SLAB DELTA, 5.2° ANGLE OF ATTACK, $M = 9.6$

7.3 HEATING RATE DISTRIBUTION

Axial heating rates along the windward centerline are presented in Figures 89, 90, and 91. Laminar and turbulent heating rates for 5.5 degrees angle of attack are compared in Figure 89. A comparison of the laminar heating rates for the two angles of attack at $M_\infty = 6.8$ is made in Figure 90. The results for $M_\infty = 9.6$ are added, and are presented in Figure 91. Spanwise laminar and turbulent heating rates for 5.5 degrees angle of attack at several body stations are compared in Figures 92 through 96.

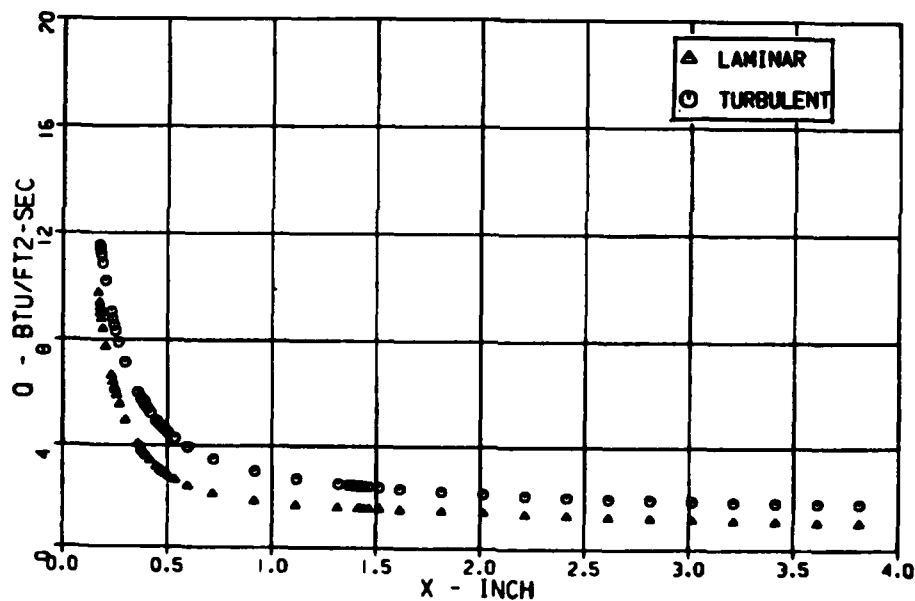


FIGURE 89 - SLAB DELTA WINDWARD CENTERLINE HEATING,
5.5° ANGLE OF ATTACK, $M = 6.8$

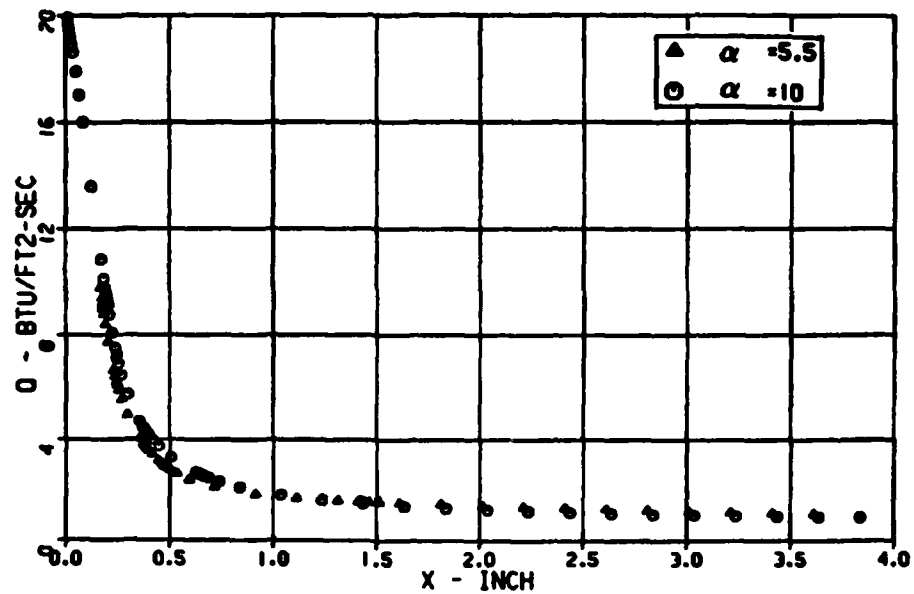


FIGURE 90 - SLAB DELTA WINDWARD CENTERLINE HEATING,
 $M = 6.8$, LAMINAR FLOW

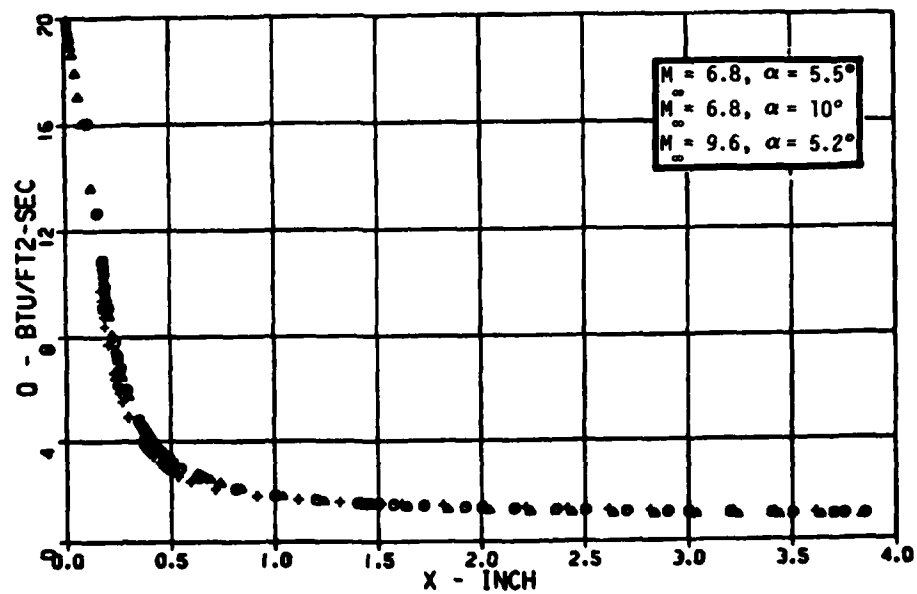


FIGURE 91 - SLAB DELTA WINDWARD CENTERLINE HEATING, LAMINAR FLOW

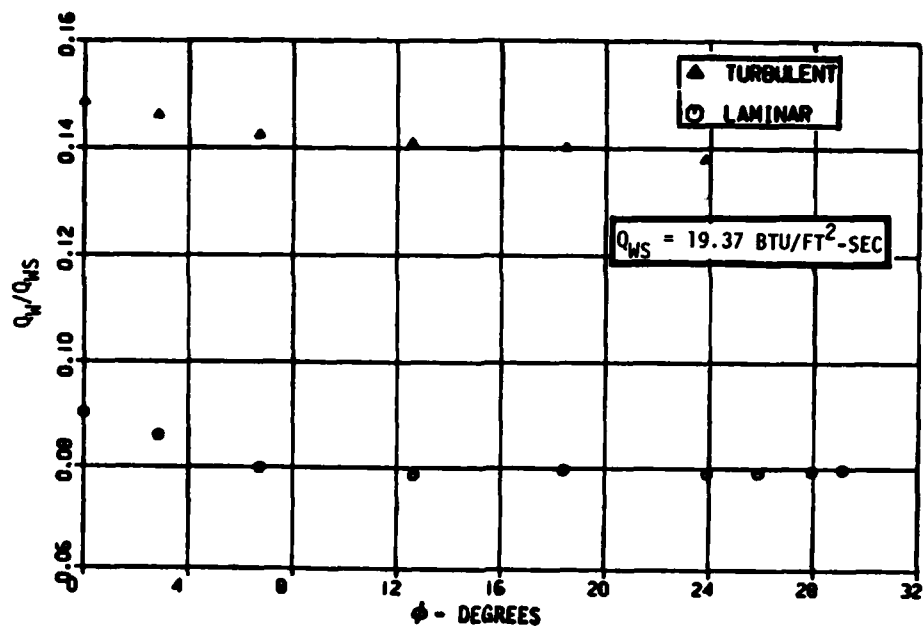


FIGURE 92 - SLAB DELTA SPANWISE HEATING, 5.5° ANGLE OF ATTACK,
 $M = 6.8$, $X = 1.0$ INCH

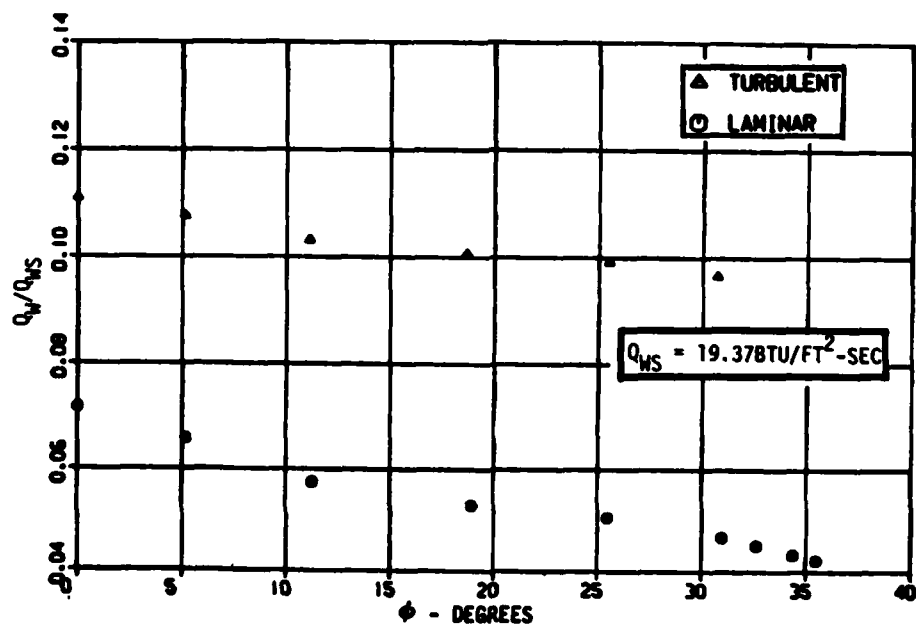


FIGURE 93 - SLAB DELTA SPANWISE HEATING, 5.5° ANGLE OF ATTACK,
 $M = 6.8$, $X = 2.0$ INCH

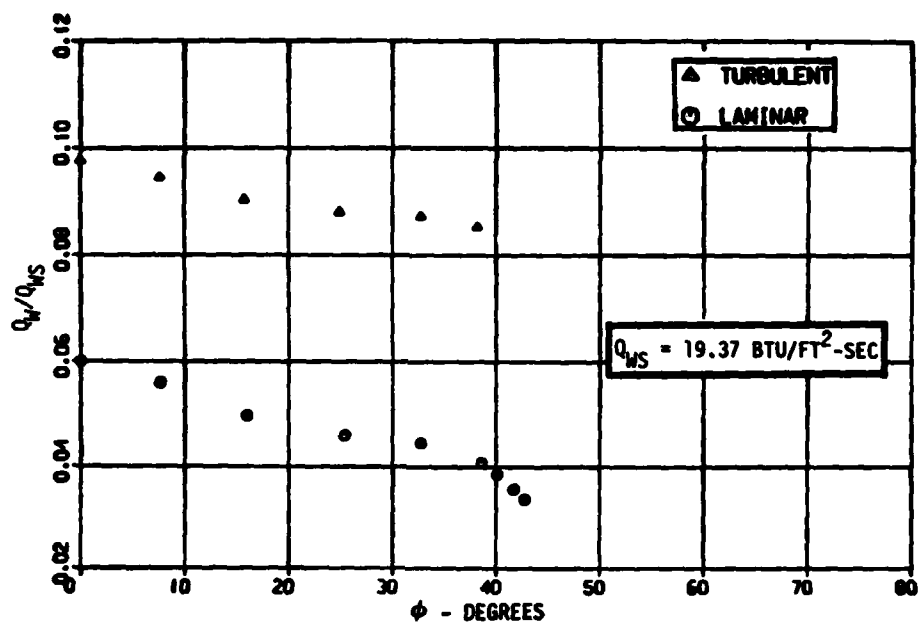


FIGURE 94 - SLAB DELTA SPANWISE HEATING, 5.5° ANGLE OF ATTACK,
 $M = 6.8$, $X = 3.0$ INCH

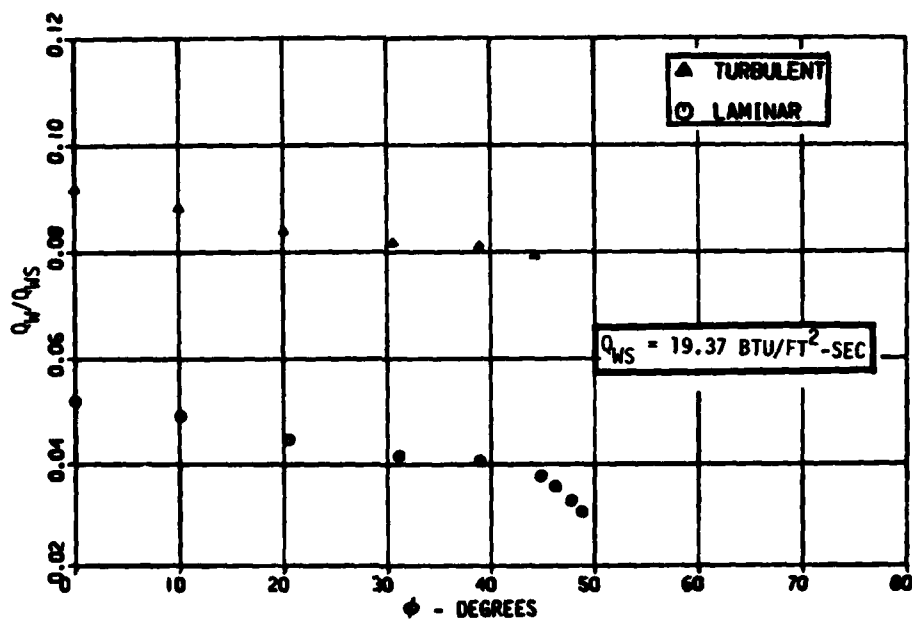


FIGURE 95 - SLAB DELTA SPANWISE HEATING, 5.5° ANGLE OF ATTACK,
 $M = 6.8$, $X = 4.0$ INCH

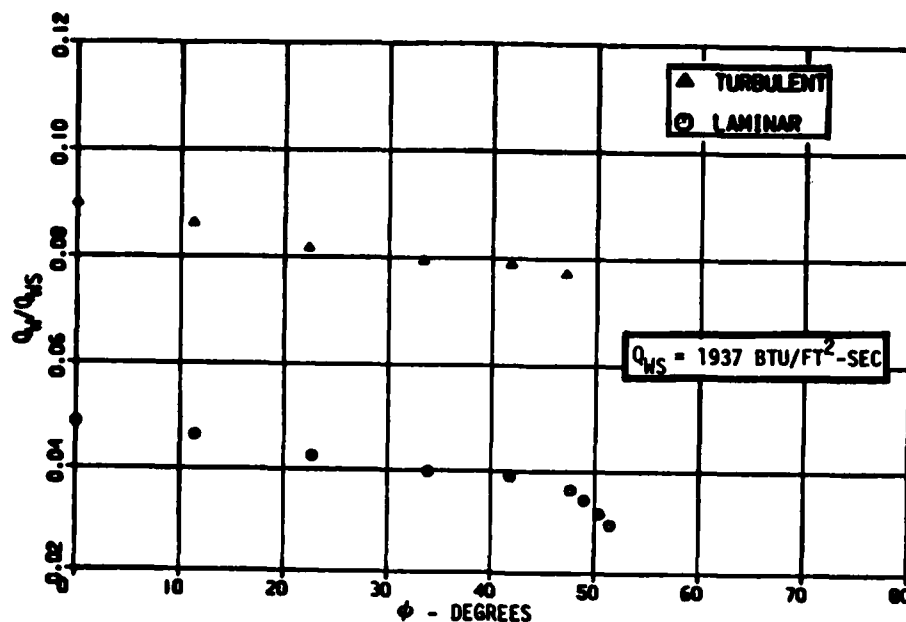


FIGURE 96 - SLAB DELTA SPANWISE HEATING, 5.5° ANGLE OF ATTACK,
M = 6.8, X = 4.53 INCH

7.4 FLAP HEATING

The spanwise distribution of peak heating rate at reattachment to a flap located at the aft end of the lower surface of the basic slab delta model was calculated for two conditions; 10 degrees angle of attack at $M_\infty = 6.8$ and 5.2 degrees angle of attack at $M_\infty = 9.6$. The variation of the enthalpy heat transfer coefficient, h/C_p , with flap angle at several spanwise locations is shown in Figures 97 and 98. (The enthalpy heat transfer coefficient is used with enthalpy difference rather than with the temperature difference, and is presented here as the temperature heat transfer coefficient divided by specific heat.) Incipient separation for the $M_\infty = 6.8$ case occurs at a flap angle of approximately 2.5°, and the flap angle can be increased to about 32° before the

local Mach number goes subsonic, which is the limit of the current calculation procedure. For the $M_\infty = 9.6$ case, incipient separation occurs at a flap angle of approximately 5° , and the flap angle can be increased to about 40° . The heat transfer coefficient spanwise distribution at three flap angles is compared for the two Mach numbers in Figures 99, 100 and 101. Flap heating for $M_\infty = 6.8$, which represents a higher Reynolds number, is greater than for $M_\infty = 9.6$, and shows a spanwise peak. An additional comparison at several flap angles for each Mach number is made in Figures 102 and 103.

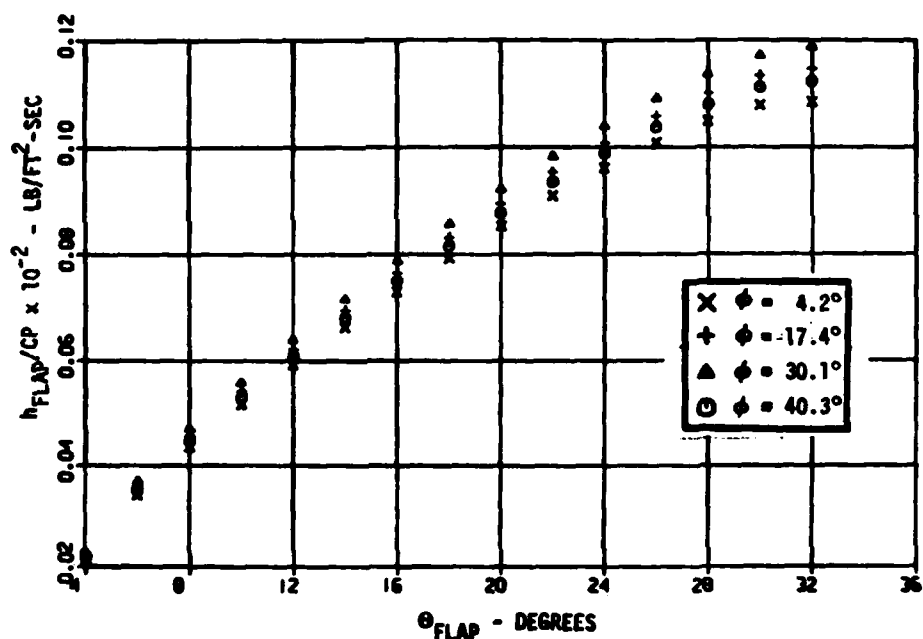


FIGURE 97 - PEAK HEATING ON A FLAP, 10° ANGLE OF ATTACK, $M = 6.8$

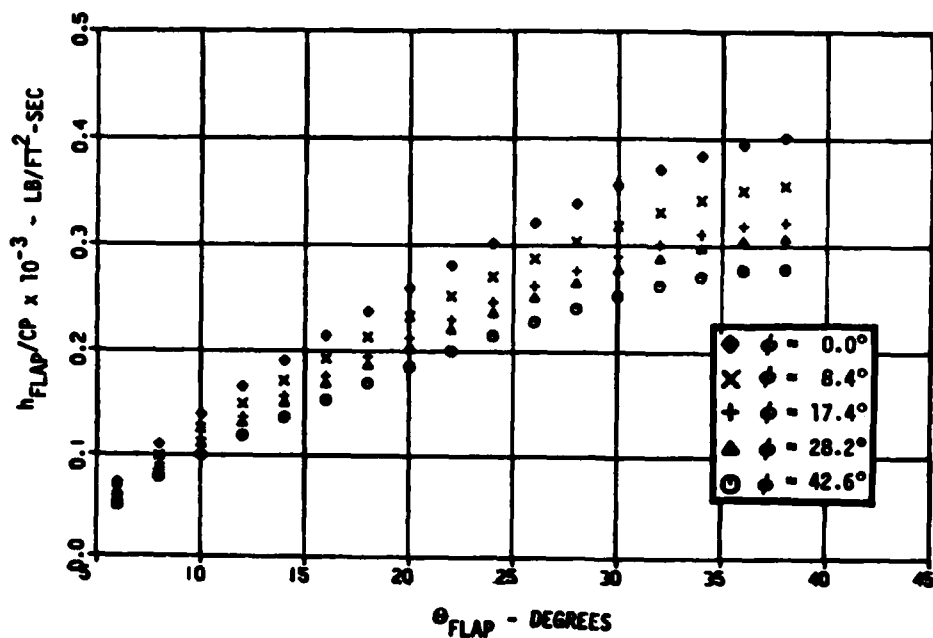


FIGURE 98 - PEAK HEATING ON A FLAP, 5.2° ANGLE OF ATTACK, M = 9.6

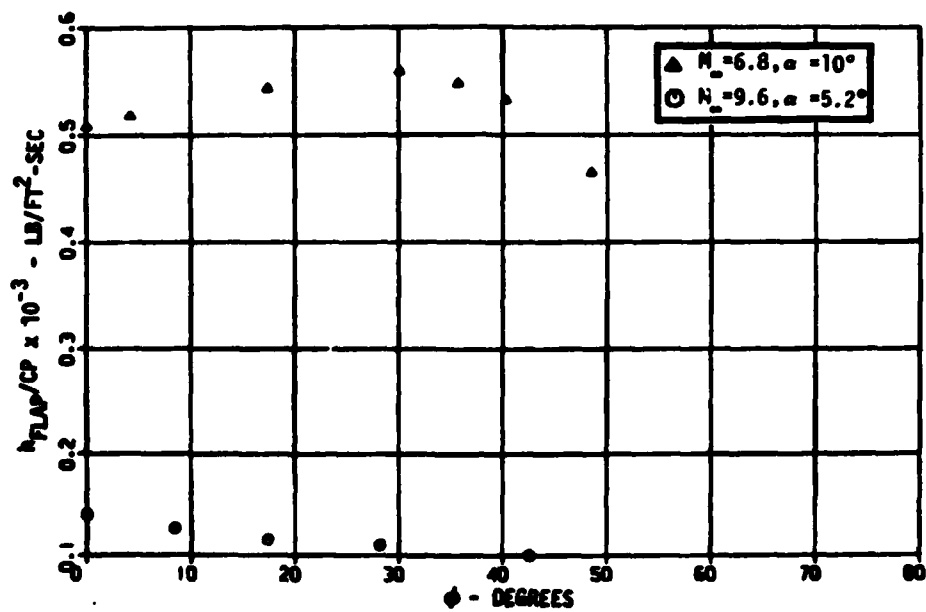


FIGURE 99 - SPANWISE PEAK HEATING ON A FLAP, FLAP ANGLE = 10°

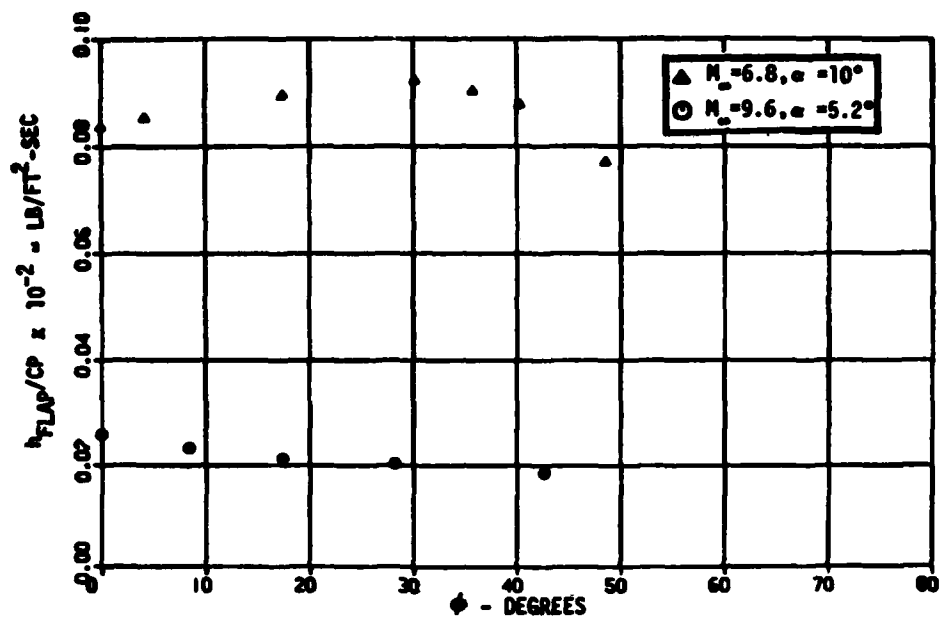


FIGURE 100 - SPANWISE PEAK HEATING ON A FLAP, FLAP ANGLE = 20°

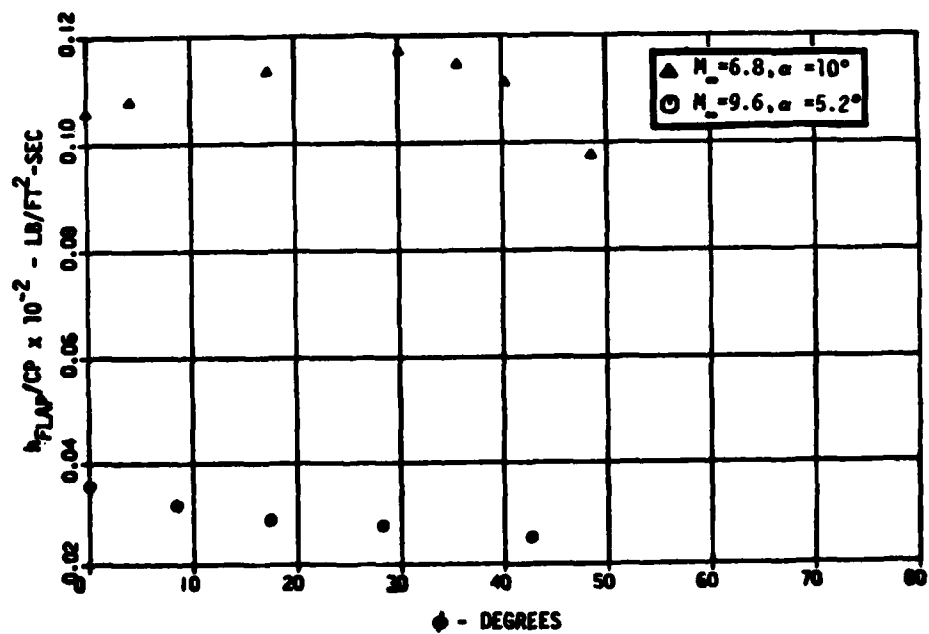


FIGURE 101 - SPANWISE PEAK HEATING ON A FLAP, FLAP ANGLE = 30°

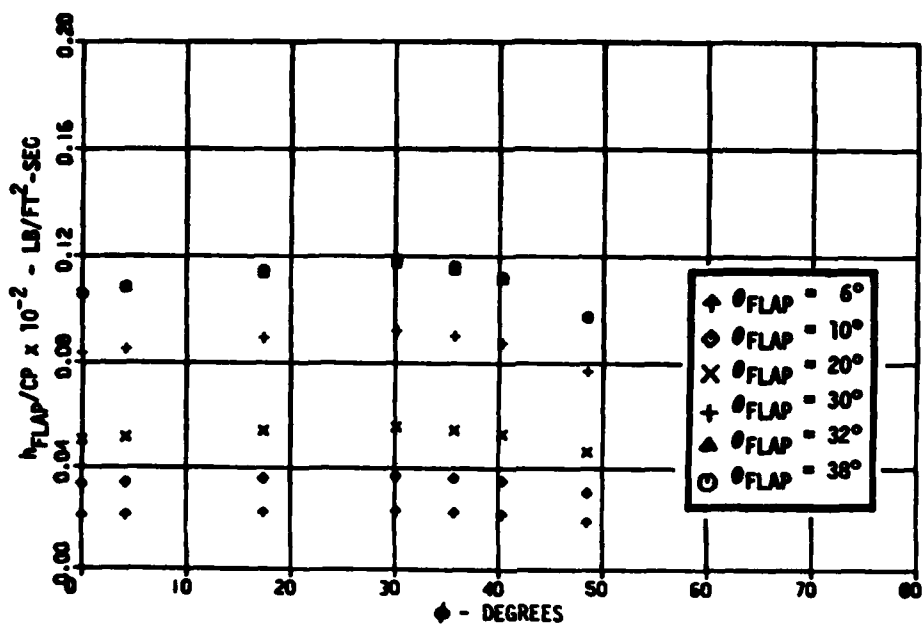


FIGURE 102 - SPANWISE PEAK HEATING ON A FLAP,
10° ANGLE OF ATTACK, M = 6.8

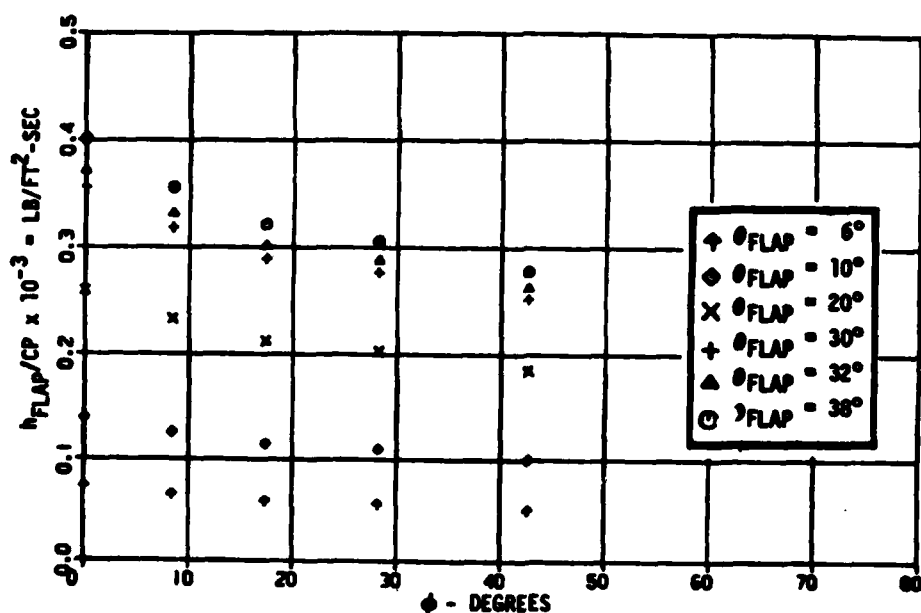


FIGURE 103 - SPANWISE PEAK HEATING ON A FLAP,
5.2° ANGLE OF ATTACK, M = 9.6

A similar treatment of the nondimensional local Stanton number at the reattachment point is presented in Figures 104 through 110. The trends in Stanton number are somewhat different from those for the heat transfer coefficient, however. The Stanton number shows a peak with flap angle. At the same flap angle, the lower Reynolds number ($M_\infty = 9.6$) results in higher Stanton numbers, although a spanwise peak still occurs with the higher Reynolds number ($M_\infty = 6.8$).

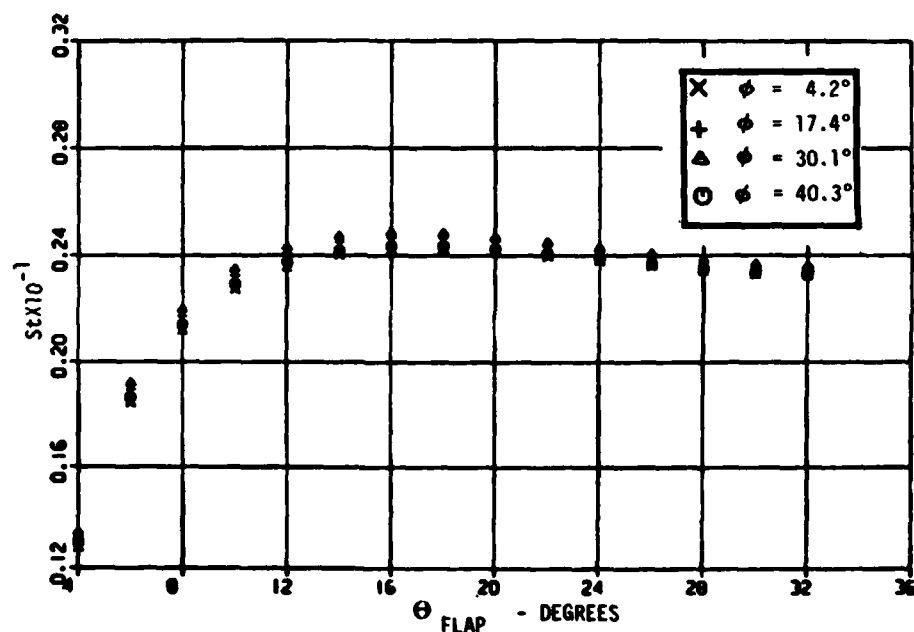


FIGURE 104 - PEAK STANTON NUMBER ON A FLAP, 10° ANGLE OF ATTACK,
 $M = 6.8$

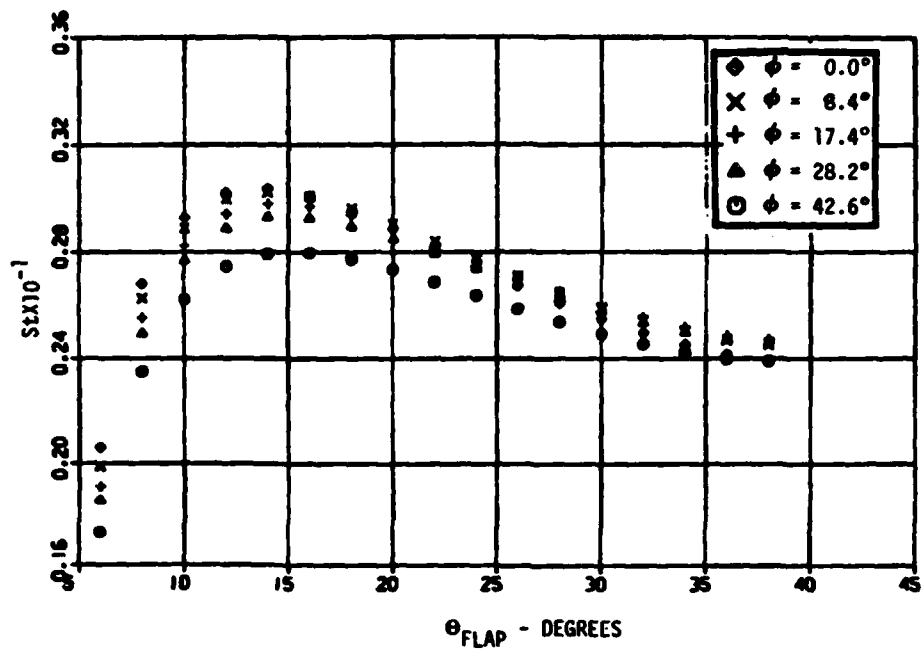


FIGURE 105 - PEAK STANTON NUMBER ON A FLAP, 5.2°
ANGLE OF ATTACK, $M = 9.6$

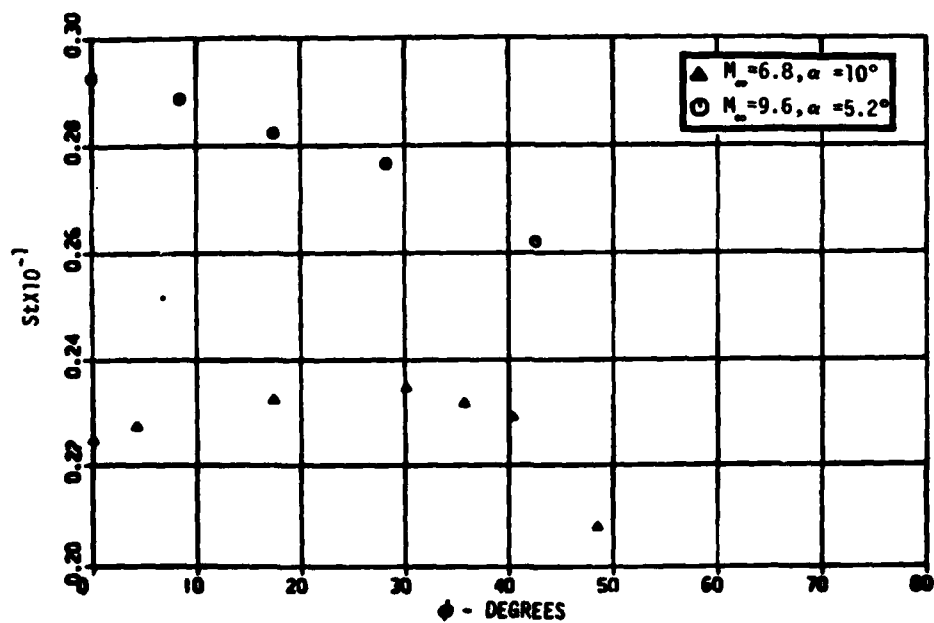


FIGURE 106 - SPANWISE PEAK STANTON NUMBER ON A FLAP,
FLAP ANGLE = 10°

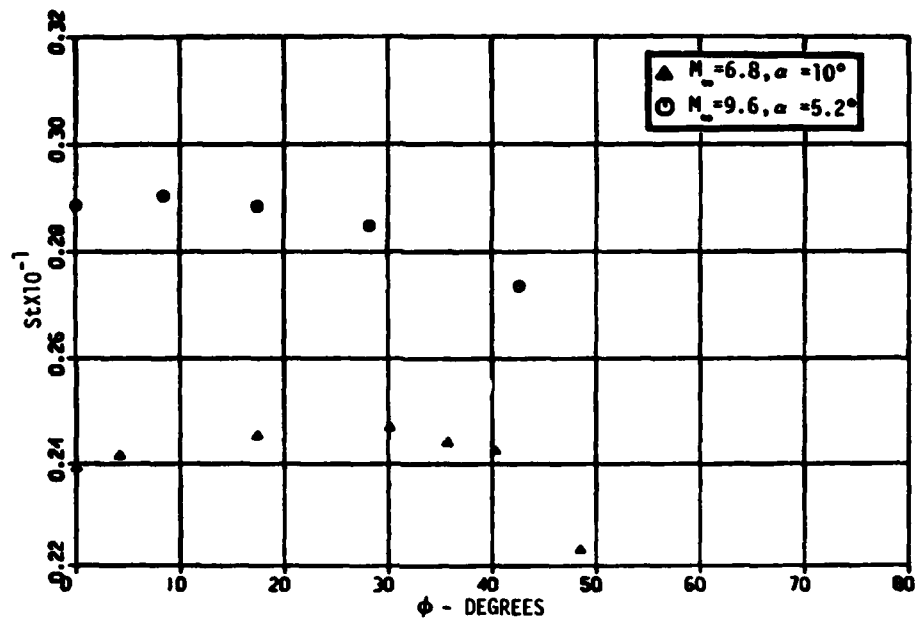


FIGURE 107 - SPANWISE PEAK STANTON NUMBER ON A FLAP,
FLAP ANGLE = 20°

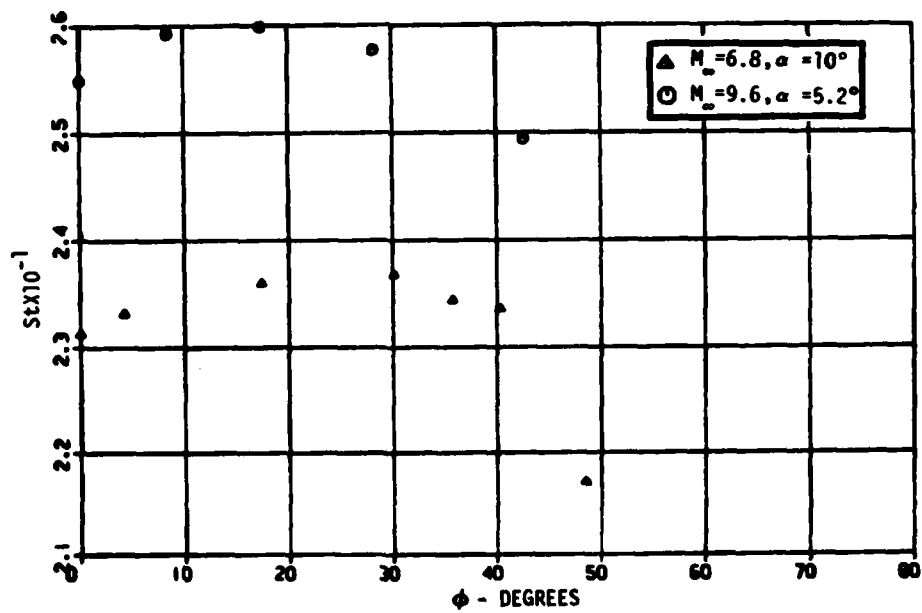


FIGURE 108 - SPANWISE PEAK STANTON NUMBER ON A FLAP,
FLAP ANGLE = 30°

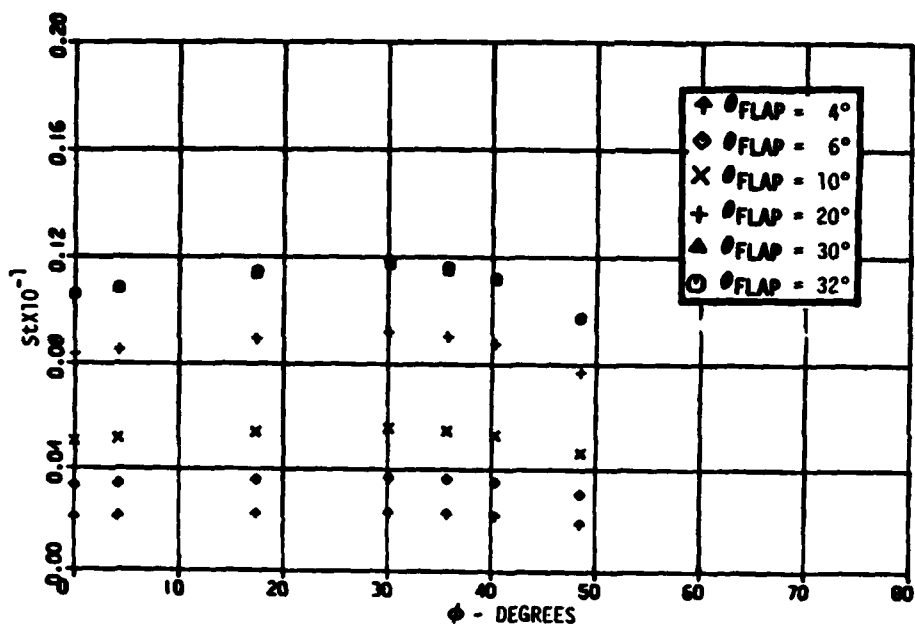


FIGURE 109 - SPANWISE PEAK STANTON NUMBER ON A FLAP, 10°
ANGLE OF ATTACK, M = 6.8

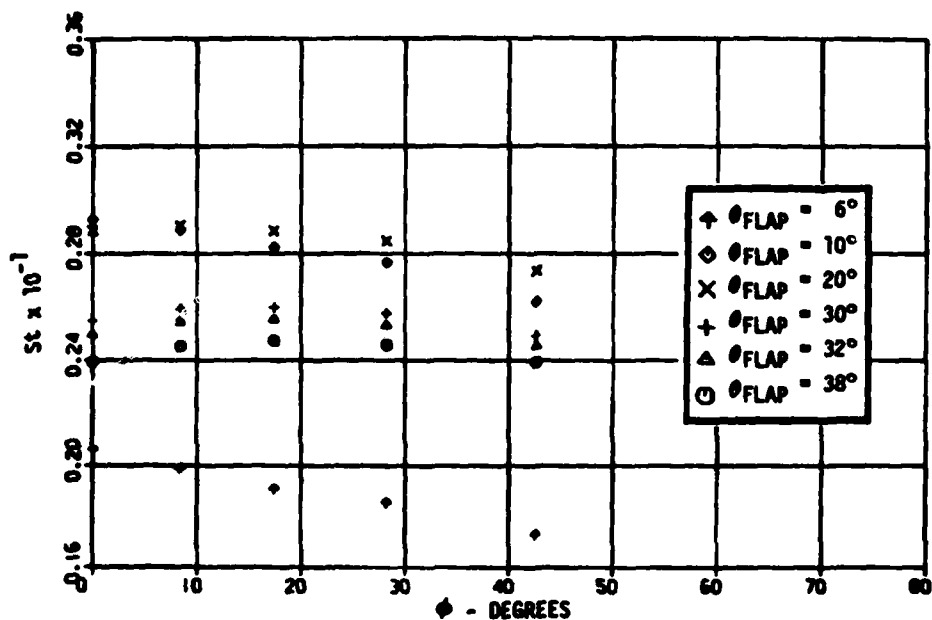


FIGURE 110 - SPANWISE PEAK STANTON NUMBER ON A FLAP, 5.2°
ANGLE OF ATTACK, M = 9.6

APPENDIX A

TWO-STREAMLINE SCALE FACTOR EQUATION

The following two equations relating geometric parameters used in the scale factor analysis are presented on pages 23 and 24 of Reference 5.

$$dx = \hat{e}_s \cdot \hat{e}_x h_s d\xi + \hat{e}_\rho \cdot \hat{e}_x h d\rho \quad (A-1)$$

$$f d\phi = \hat{e}_s \cdot \hat{e}_\phi h_s d\xi + \hat{e}_\rho \cdot \hat{e}_\phi h d\rho \quad (A-2)$$

From Equations (39), (40) and (62) of Reference 5 it can be shown that

$$\left. \begin{aligned} \hat{e}_s \cdot \hat{e}_x &= \cos \theta \cos \Gamma' \\ \hat{e}_s \cdot \hat{e}_\phi &= \sin \theta \cos \delta_\phi - \cos \theta \sin \delta_\phi \sin \Gamma' \\ \hat{e}_\rho \cdot \hat{e}_x &= -\sin \theta \cos \Gamma' \\ \hat{e}_\rho \cdot \hat{e}_\phi &= \cos \theta \cos \delta_\phi + \sin \theta \sin \delta_\phi \sin \Gamma' \\ \sin \theta \cos \delta_\phi - \cos \theta \sin \delta_\phi \sin \Gamma' &= f \frac{d\phi}{d\xi} \end{aligned} \right] \quad (A-3)$$

Equation (A-2) can be solved for $h_s d\xi$.

$$h_s d\xi = (f d\phi - \hat{e}_\rho \cdot \hat{e}_\phi h d\rho) / (\hat{e}_s \cdot \hat{e}_\phi) \quad (A-4)$$

This result may be substituted into Equation (A-1) to give

$$dx = \frac{\hat{e}_s \cdot \hat{e}_x}{\hat{e}_s \cdot \hat{e}_\phi} \left(f d\phi - \hat{e}_\beta \cdot \hat{e}_\phi h d\beta \right) + \hat{e}_\beta \cdot \hat{e}_x h d\beta \quad (\text{A-5})$$

If this expression is divided by $d\beta$ and solved for h , we find that

$$h = \frac{\left[\frac{dx}{d\beta} - \left(\frac{\hat{e}_s \cdot \hat{e}_x}{\hat{e}_s \cdot \hat{e}_\phi} \right) f \frac{d\phi}{d\beta} \right]}{\left[\hat{e}_\beta \cdot \hat{e}_x - \left(\frac{\hat{e}_s \cdot \hat{e}_x}{\hat{e}_s \cdot \hat{e}_\phi} \right) \hat{e}_\beta \cdot \hat{e}_\phi \right]} \quad (\text{A-6})$$

By incorporating the results of Equation (A-3) it can be shown that

$$h = \left[\cos \theta \frac{d\phi}{d\beta} - \left(\frac{dx}{d\beta} \right) \left(\frac{d\phi}{ds} \right) / \cos \Gamma \right] \frac{f}{\cos \delta_\phi} \quad (\text{A-7})$$

It is this expression that is used to calculate the scale factor in the computer program.

REFERENCES

1. DeJarnette, F. R., and Jones, M. H., "Calculation of Inviscid Surface Streamlines and Heat Transfer on Shuttle Type Configurations, Part II - Description of Computer Program," NASA CR-111922, August 1971.
2. Gentry, A. E., Smyth, D. N., and Oliver, W. R., "The Mark IV Supersonic-Hypersonic Arbitrary-Body Program. Volume I - User's Manual," AFFDL-TR-73-159, Volume I, November 1973.
3. Gentry, A. E., Smyth, D. N., and Oliver, W. R., "The Mark IV Supersonic-Hypersonic Arbitrary-Body Program. Volume II - Program Formulation," AFFDL-TR-73-159, Volume II, November 1973.
4. Fivel, H. J. "Numerical Flow Field Program for Aerodynamic Heating Analysis. Interim Report," AFFDL-TR-79-3025, April 1979.
5. DeJarnette, F. R., "Calculation of Inviscid Surface Streamlines and Heat Transfer on Shuttle-Type Configurations, Part I - Description of Basic Method," NASA CR-111921, August 1971.
6. Beckwith, I. E., and Cohen, N. B., "Application of Similar Solutions to Calculation of Laminar Heat Transfer on Bodies with Yaw and Large Adverse Pressure Gradient in High-Speed Flow," NASA TN D-625, 1961.
7. Reshotko, E., and Tucker, M., "Approximate Calculation of the Compressible Turbulent Boundary Layer with Heat Transfer and Arbitrary Pressure Gradient," NACA TN 4154, 1957.
8. Spalding, D. B., and Chi, S. W., "The Drag of a Compressible Turbulent Boundary Layer on a Smooth Flat Plate With and Without Heat Transfer," J. Fluid Mech., Vol. 18, pt. 1, January 1964, pp. 117-143.
9. Bertram, M. H., and Neal, L., "Recent Experiments in Hypersonic Turbulent Boundary Layers," Paper presented at the AGARD Specialists Meeting on Recent Developments in Boundary-Layer Research, Sponsored by the Fluid Dynamics Panel of AGARD, Naples, Italy, 1965.
10. Dhawan, S., and Narasimha, R., "Some Properties of Boundary Layer Flow During the Transition from Laminar to Turbulent Motion," J. Fluid Mech., Vol. 3, No. 4, April 1958, pp. 418-436.
11. DeJarnette, F. R., "Calculation of Heat Transfer of Shuttle-Type Configurations Including the Effects of Variable Entropy at Boundary Layer Edge," NASA CR-112180, October 1972.
12. Dahlem, V., and Buck, M. L., "Experimental and Analytical Investigations of Vehicle Designs for High Lift-Drag Ratios in Hypersonic Flight," AFFDL-TR-67-138, June 1967.
13. Kaufman, L. G., II, "Pressure Estimation Techniques for Hypersonic Flows Over Blunt Bodies," The Journal of the Astronautical Sciences, Vol. X, No. 2, Summer 1963.

14. Van Dyke, M. D., "A Study of Hypersonic Small-Disturbance Theory," NACA Report 1194, 1954.
15. Ames Research Staff, "Equations, Tables, and Charts for Compressible Flow," NACA Report 1135, 1953.
16. Korn, G. A., and Korn, T. M., "Mathematical Handbook for Scientists and Engineers," McGraw-Hill, April 1961.
17. Hammitt, A. G., and Murthy, K. R. A., "Approximate Solutions for Supersonic Flow Over Wedges and Cones," Journal of the Aero/Space Sciences, Volume 27, No. 1, January 1960.
18. Bertram, M. H., and Everhart, P., "An Experimental Study of the Pressure and Heat-Transfer Distribution on a 70° Sweep Slab Delta Wing in Hypersonic Flow," NASA TR R-153, December 1963.
19. McElderry, E. D., Jr., "A Pressure Distribution Study of Highly Swept Deltas at Hypersonic Speeds from -15 Degrees to +15 Degrees Angle of Attack," AFFDL-TR-70-82, October 1970.
20. Hankey, W. L., Neumann, R. D., and Flinn, E. H., "Design Procedures for Computing Aerodynamic Heating at Hypersonic Speeds," WADC Technical Report 59-610, June 1960.
21. Eckert, E. R. G., "Survey of Boundary Layer Heat Transfer at High Velocities and High Temperatures," WADC TR-59-624, April 1960.
22. Van Driest, E. R., "Problem of Aerodynamic Heating," Aeronautical Engineering Review, Vol. 15, No. 10, October 1956, pp. 26-41.
23. Hopkins, E. J., and Inouye, M., "An Evaluation of Theories for Predicting Turbulent Skin Friction and Heat Transfer on Flat Plates at Supersonic and Hypersonic Mach Numbers," AIAA Journal, Vol. 9, No. 6, June 1971, pp. 993-1003.
24. Kessler, W. C., Reilly, J. F., and Mockapetris, L. J., "Supersonic Turbulent Boundary Layer Interaction With An Expansion Ramp and Compression Corner," McDonnell Douglas Astronautics Company - St. Louis Report MDC E0264, 17 December 1970.
25. Wuerer, J. E. and Clayton, F. I., "Flow Separation in High Speed Flight. A Review of the State-of-the-Art," Douglas Report SM-46429, April 1965.
26. Bushnell, D. M. and Weinstein, L. M., "Correlation of Peak Heating for Reattachment of Separated Flows," J. of Spacecraft and Rockets, Vol. 5, No. 9, September 1968, pp. 1111-1112.
27. Hayes, R., "Prediction Techniques for the Characteristics of Fin Generated Three Dimensional Shock Wave Turbulent Boundary Layer Interactions," AFFDL-TR-77-10, May 1977.

28. Scuderi, L. F., "Expressions for Predicting 3-D Shock Wave-Turbulent Boundary Layer Interaction Pressures and Heating Rates," Presented to AIAA 16th Aerospace Sciences Conference, 16 Jan 1978.
29. Token, K. H., "Heat Transfer Due to Shock Wave Turbulent Boundary Layer Interactions on High Speed Weapon Systems," AFFDL-TR-74-77, April 1974.
30. DeJarnette, F. R., and Ford, C. P., "Surface Fitting Three-Dimensional Bodies," NASA SP-390, pp. 447-474, October 1975, also in Final Report on NASA Grant NGR 34-002-193, July 1974.
31. Solomon, J. M., et al, "A Program for Computing Steady Inviscid Three-Dimensional Supersonic Flow on Reentry Vehicles, Vol. I: Analysis and Programming," NSWC/WOL/TR 77-28, 11 February 1977.